Interband Cascade Lasers, from FabryPérot Waveguides to Subwavelength Cavities

by

Jeyran Amirloo Abolfathi

A thesis
presented to the University of Waterloo
in fulfillment of the
thesis requirement for the degree of
Doctor of Philosophy
in
Electrical and Computer Engineering

Waterloo, Ontario, Canada, 2015

© Jeyran Amirloo Abolfathi 2015

I hereby declare that I am the sole author of this thesis. This is a true copy of the thesis, including any required final revisions, as accepted by my examiners. I understand that my thesis may be made electronically available to the public.

Abstract

This research in centered around engineering approaches to improve the electro-optical performance of interband cascade lasers. The enhancement strategies are ranging from empirical design optimizations and fabrication and packaging techniques to design and application of optical coating. These improvements resulted in room temperature (RT) CW optical powers of 40 mW, as well as, internal loss and threshold current densities as low as 4.9 cm^{-1} and 365 A/cm^2 respectively. Moreover, additional improvements resulted in devices with threshold current density as low as 320 A/cm^2 and wall plug efficiency reaching up to 5.9% for a 1 mm device producing 20.3 mW CW RT output power. Application of Antireflection (AR) coatings to interband cascade lasers not only led to identification of several promising material combinations for AR coatings in Mid-Infrared (Mid-IR) region of the spectrum, but was also used to study the fundamental laser parameters such as internal efficiency and leakage current. AR coatings ranging from 0.15 to 7E-4 were designed and fabricated on ICL waveguide facets. By monitoring the laser performance before and after coating a direct relation between carrier concentration and leakage currents was observed and an optimal reflectivity value of 9.6E-3 was experimentally extracted in order to achieve the maximum slope efficiency for a 1 mm device. As the next step toward utilization of the Mid-IR ICLs a systematic approach to design of sub-wavelength cavities was developed with universal applications in active plasmonic cavities. Key parameters such as quality factor, confinement factor, and threshold gain have been calculated and their dependence of cavity parameters are demonstrated which enables a flexible design for various applications. In particular a coaxial cavity with energy confinement factor of 84% and mode volume of 0.14 $(\lambda/2n)^3$ and quality factor of Q=515 was designed at 3.55μm. The dependence of the emission wavelength to the surrounding refractive index was also demonstrated with potential sensing applications.

Acknowledgements

It is with great pleasure that I thank my supervisors, Professor Simarjeet Singh Saini and Professor Mario Dagenais for their continuous support, and encouragement. They have guided me throughout my PhD studies with endless enthusiasm and patience and I am very grateful.

I would like to thank my external examiner, Professor Dan Botez for taking the time to review my thesis and for valuable discussions and instructive suggestions. Many thanks to my committee members, Professor Zbig Wasilewski, Professor Dayan Ban, and Professor Donna Strickland.

My gratitude goes to Dr. J. Bruno and F. Towner for supplying the laser material used in this work.

Special thanks to my colleague and friend, Dr. Geunmin Ryu, for his support throughout my PhD studies.

I would like to acknowledge the Laboratory for Green Nanophotonics, Optoelectronics and Nanosensing in the University of Maryland led by Professor Mario Dagenais, where I have conducted all the laser measurement, packaging, and anti-reflection coating fabrications, the Nanophotonics and Integrated Optoelectronics laboratory, lead by Prof. Simarjeet S. Saini at the University of Waterloo, and University of Maryland Fablab where I fabricated my devices. Many thanks to the University of Maryland Fablab team, John Abrahams, Tom Loughran, Jonathan A. Hummel, and Jim O'Connor. They have always been there for me and made the impossible possible and I am deeply grateful to all of them.

I acknowledge the financial support from the University of Waterloo and the Ontario Graduate Scholarship (OGS), and the Queen Elizabeth II Graduate Scholarships in Science and Technology (QEII-GSST).

And last but not least, I would like to thank my beloved husband, Behnood. His unconditional love and support empower me everyday to peruse my dreams and have made this work possible.

Jeyran Amirloo

Fall 2015

Dedicated to the love of my life, the light of my day, Behnood.

Contents

List of Figures **xviii**

1 Introduction **1**

2 Interband Cascade Laser - Design and Simulation **10**

2.1 Cascade or Non-Cascade 10

2.2 ICL and QCL, a Comparison 12

2.3 ICL Operation Principles 14

2.3.1 Active Region 15

2.3.2 Electron/Hole Injector and Semi-Metallic Interface 16

2.4 δ-Strained Quantum well 21

2.5 Optical Mode and Waveguide Design 22

3 Device Fabrication and Packaging **26**

3.1 Introduction 26

3.2 Step by Step Fabrication Process 27

3.3 Mask design 36

3.4 Self-aligned fabrication 40

3.5 Sample Packaging 42

4 Towards Room Temperature Operation of ICLs **45**
4.1 Introduction 45
4.2 Characterization Methodology 46
4.3 Laser Test Setup 49
4.4 Interband Cascade Laser Characterization 52
4.5 Results and Discussions 53
4.6 Series Resistance 66
4.6.1 Contact Resistance 66
4.6.2 Contact Metallization 70
4.7 Packaging Considerations 70
4.7.1 Annealing 70
4.7.2 Metal Diffusion and Contact Metal 72
4.8 Temperature Dependent Measurements of ICLs 74
4.9 Conclusion 77

5 Mid-Infrared Anti-Reflection Coatings **79**
5.1 Introduction 79
5.2 Theory of Transmission and Reflection of Light 81
5.2.1 Fresnel Reflection 81
5.2.2 Transverse Electric Plane Wave 82
5.2.3 Transverse Magnetic Plane Wave 84
5.2.4 Reflectance and Transmittance 86
5.2.5 Matrix Formulation for Multi-layer Systems 87
5.2.6 Mode Decomposition and ARC Design 88
5.2.7 Merit Function 90
5.3 Anti-Reflection Coating Facility with *in-situ* Reflectometry 90

5.3.1 Single Layer Coating . . . 94
5.3.2 Multi-Layer Coating . . . 95
5.4 Materials for Infrared Coatings . . . 97
5.5 Experimental Results . . . 101
5.5.1 Single Layer AR Coating . . . 102
5.5.2 Double Layer AR Coating in ICL . . . 104
5.6 Anti-Reflection Coating and Measurement of Reflectivity . . . 109
5.7 Carrier Leakage in ICLs . . . 112
5.7.1 Extraction of Leakage Current . . . 113
5.7.2 Discussion . . . 117
5.8 Conclusions . . . 121

6 Mid-IR Subwavelength Lasers 123
6.1 Introduction . . . 123
6.2 Surface Plasmon Polaritons (SPP) . . . 127
6.3 Metallic Optical Resonators . . . 134
6.4 Principles of Lasing in Metallic Cavities . . . 139
6.5 Mid-IR Microcavities Design and Simulations . . . 143
6.5.1 Full-Wave 3D Analysis . . . 156
6.5.2 Optical Pumping and Scattering from Cavity . . . 162
6.5.3 Electrical Pumping . . . 162
6.6 Discussions and Conclusions . . . 165

7 Conclusions and Future Works 169

Bibliography 173

Appendices **188**

A Material Dispersion and Refractive Indices in Mid-IR **189**

B Double Layer AR Coating Designs **196**

List of Figures

1.1 Infrared atmospheric “transmission window”, adopted from [1]. 4

2.1 Interband cascade laser band structure and relevant electron/hole wavefuctions, Reprinted by permission from Macmillan Publishers Ltd: nature communications [2], copyright © 2011. 15
2.2 Interband cascade laser W-shaped active region. 16
2.3 InAs/GaSb Type-II broken gap band alignment, Reprinted by permission from Macmillan Publishers Ltd: nature communications [2], copyright © 2011. 18
2.4 δ-Strained quantum well band structure (a) initial and (b) final design . . 22
2.5 ICL layer composition and the corresponding refractive indices 23
2.6 Rsoft simulation results: (a) 2D refractive index map of an ICL waveguide with 10 μm width and 3 μm height (b) fundamental mode profile (c) 1D refractive index map (d) 1D cut of the fundamental mode. 25

3.1 Double trench laser waveguides 29
3.2 Wet etching configuration 30
3.3 Dielectric Opening on top of the laser waveguide 32

3.4 (a) Image reversal photo-lithography creating an undercut needed for lift-off (b) regular photo-lithography and SEM picture of a properly created undercut. 33
3.5 an ICL sample after top contact deposition. 35
3.6 (a) an ICL sample after electrodeposition of gold (b) Electroplating Setup . 35
3.7 SEM picture of (a) An individual laser Die (b) an ICL cleaved facet 37
3.8 Interband Cascade Laser Process Flow 39
3.9 Planarization results for double trench waveguides. (a) an optical microscope picture of a planarized and etched sample. (b-d) SEM pictures of the cross section of the diced sample from different angles. 41
3.10 (a) Laser die bonder (b) Die attach process 43
3.11 A packaged 5 mm interband cascade laser diode. 44

4.1 Laser bar probe station 49
4.2 Biasing circuit. 50
4.3 The Copper Holder of the ICL characterization setup. 51
4.4 ICL wavelength measurement setup. 51
4.5 0.5 mm Interband cascade laser bar 53
4.6 (a) IVL curve for 12-cascade ICL for cavity length 0.6 mm (solid line) 1 mm (dashed line) 2 mm (dotted line) (b) Threshold current density versus 1/cavity length 55
4.7 (a) IVL curve for 6 cascade ICL for cavity length 1 mm (solid line) 2 mm (dashed line) 3 mm (dotted line) (b) Threshold current density versus 1/cavity length [3] 56
4.8 (a) IVL curve for 5-cascade ICL for cavity length 1 mm (solid line) 2 mm (dashed line) 3 mm (dotted line) and 5 mm (dotted-dashed line) (b) Threshold current density versus 1/cavity length [3] 58
4.9 Normalized intensity vs. emission wavelength for the 5-cascade ICL at 3.8 μm. 59

4.10 (a) IVL curve for 5-cascade ICL for cavity length 1 mm (solid line) 2 mm (dashed line) 3 mm (dotted line)) (b) Threshold current density versus 1/cavity length 60
4.11 (a) IVL curve for δ-strained 5-cascade ICL for cavity length 1 mm (solid line) 2 mm (dashed line) 3 mm (dotted line) and 5 mm (dotted-dashed line) (b) Threshold current density versus 1/cavity length 61
4.12 Intensity vs. emission wavelength for the δ-strained ICL 62
4.13 CW IVL for a 3 mm long 5-cascade ICL at 3.8 μm 63
4.14 (a) CW IVL for a 5 mm long 5-cascade ICL at 3.8 μm 63
4.15 (a) CW IVL for a 1 mm long 5-cascade ICL at 3.5 μm(b) WPE for a 1 mm long 5-cascade ICL at 3.5 μm 65
4.16 CTLM Pattern for r = 200 μm and d=8, 14, 20, 30, 50 μm(left). Measured contact resistance (right). 67
4.17 (a) SEM picture of the dielectric opening. The two narrow lines on either side of the waveguide are all that is left from the isolating SiN layer (b) The effect of narrow (solid) and wide (dashed) dielectric opening on the series resistance of a 1 mm δ-strained laser die. 69
4.18 LI characteristics for a 10μm ridge 12-cascade ICL subjected to the annealing study. The devices were annealed in ambient and were tested again at room temperature for comparison. 71
4.19 IV characteristics for a 10μm ridge 12-cascade ICL subjected to the annealing study. 72
4.20 IV and LI for a 1 mm 5-cascade laser measured at different temperatures. 75
4.21 Temperature dependence of (a) slope efficiency [4] and (b) threshold current for a range of temperatures between 250K and 320K 76

5.1 Transmission and reflection of a plane wave at the boundary of two dielectrics. 82

5.2 Transmission and reflection of a TE polarized plane wave at the boundary of two dielectrics. 83

5.3 Transmission and reflection of a TM polarized plane wave at the boundary of two dielectrics. 85

5.4 Multi-layer dielectric interface 87

5.5 Waveguide mode and multi-layer coating 89

5.6 E-beam evaporation Facility equipped with an *in-situ* reflectometer. 91

5.7 schematic of the e-beam evaporation facility equipped with an *in-situ* reflectometer [5]. 93

5.8 reflectometry map for a double layer ZnS-YF_3 AR coating at $\lambda = 3.4\mu m$ 94

5.9 Al_2O_3 single layer coating layer reflectivity designed for a 5-cascade ICL at 3.5μm. . . . 95

5.10 ZnS-YF_3 double layer merit function contour. 97

5.11 ZnS-YF_3 double layer reflectivity spectrum 97

5.12 ZnS-SiO_2 double layer AR coating in the absence of the Ta_2O_5 adhesion layer. 100

5.13 ZrO_2 single layer AR coating for 5-cascade laser $\lambda = 3.5\ \mu m$ with cavity length of 2 mm. 102

5.14 Ta_2O_5 single layer AR coating for 5-cascade laser $\lambda = 3.8\ \mu m$ with cavity length of 1 mm. 103

5.15 SEM picture of the 5-cascade laser coated with 495 nm of Ta_2O_5 103

5.16 Al_2O_3 single layer AR coating for 5-cascade laser at $\lambda = 3.5\ \mu m$ with cavity length of 1 mm. 104

5.17 YF_3-ZnS double layer AR coating for δ-strained ICL with cavity length of 1 mm. . . . 105

5.18 ZnS-YF_3 double layer AR coating for δ-strained ICL with cavity length of 1 mm. . . . 106

5.19 ZnS-YF_3 double layer AR coating applied to a δ-strained ICL with cavity length of 2 mm and a Ta_2O_5 adhesion layer of 20nm. 107

5.20 TiO_2-SiO_2 double layer AR coating for 5-cascade ICL at $\lambda = 3.5\ \mu m$ with cavity length of 1mm 107

5.21 ZnS-SiO_2 double layer AR coating for 5 cascade ICL at $\lambda = 3.8\mu m$ with cavity length of 1mm and a Ta_2O_5adhesion layer of 20nm. 108

5.22 ZnS-SiO_2 double layer AR coating for 5 cascade ICL at $\lambda = 3.5\mu m$ with cavity length of 1mm and a Ta_2O_5adhesion layer of 20nm. 109
5.23 The ratio of internal differential efficiency after and before the coatings ($\eta_{i,A}/\eta_{i,B}$) as the facet reflectivity is changed. 119
5.24 Ratio of differential quantum efficiencies vs. Reflectivity considering the decrease in the internal differential efficiency (Solid line). Slope efficiency vs. reflectivity is also plotted for constant internal differential efficiency (dashed-line) for comparison. 120

6.1 Transverse field profile of a surface plasmon polariton along a meta-dielectric interface. . 129
6.2 Real and imaginary part of silver refractive index, Babar and Weaver 2015 (triagles) [6], Johnson and Christy 1972 (starts) [7], and fitted curve using the extended Drude model dielectric function with $\omega_p = 1.4 \times 10^{16}[rad/s^{-1}]$, $\gamma = 2.6^{13}[rad/s^{-1}]$, and $\epsilon_\infty = 5$ 132
6.3 Dispersion curve for surface plasmon for an ideal metal. The real (solid line) and imaginary (dashed line) part of the propagation constant β are shown as well as the light line. Frequency and propagation constant are both normalized to the plasma frequency. . . 133
6.4 Output power in vs derive current for a conventional semiconductor (solid line) and in the limit when spontaneous emission is only coupled to a single lasing mode (dashed line). 142
6.5 The Coaxial cavity 144
6.6 Magnitude of the electric field for a silver nanowire of 100 nm radius in a semiconductor medium 145
6.7 (a) Real and (b) Imaginary part of the effective index of a nanowire silver waveguide in the semiconductor medium versus the nanowire radius 146
6.8 Magnitude of the electric field for a semiconductor Pillar of 500 nm radius embedded in silver 147

6.9 (a) Real and (b) Imaginary part of the effective index of a circular semiconductor waveguide surrounded by silver 148
6.10 Magnitude of the electric field for the plasmonic mode of a coaxial waveguide with silver as inner and outer metal. The inner and outer radii are 100 nm and 400 nm respectively 148
6.11 Real part of the effective index for the fundamental mode of a coaxial waveguide with inner radius of 100 nm, outer radius of 400 nm 149
6.12 (a) Real and (b) Imaginary part of the effective index of a coaxial waveguide versus inner metal radii. The outer radius is kept constant at 400 nm 150
6.13 (a) Refractive index profile and (b) electric field of a 1D resonator comprised of a semiconductor medium with effective refractive index of 3.7 terminated on one side with an air interface and on the other side with a SiO_2/silver boundary 152
6.14 Dependance of the resonant wavelength on (a,b) the height of the semiconductor and (c) height of the SiO_2s layer 152
6.15 (a) Quality factor as a function of outer radius of the coaxial cavity at 4K. Overall quality factor (stars) as well as Q_{rad} (circles) and $Q_{mat}/5$ (triangles)(b)External cavity efficiency as a function of cavity outer radius, both at 4K. Simulation was perform using eigenfrequency solver of COMSOL multiphysics in 2D axisymmetric mode. 154
6.16 (a) Index profile and (b) magnitude of electric field for a vertical cross section of a coaxial cavity with $r_i = 130\ nm$, $r_o = 400\ nm$, height of the semiconductor region of 660 nm and dielectric buffer of 30 nm at 4K. 155
6.17 Quality factor as a function of outer radius of the coaxial cavity at RT. Overall quality factor (stars) as well as $Q_{rad}/2$ (circles) and Q_{mat} (triangles)(b)External cavity efficiency as a function of cavity outer radius. 156
6.18 External cavity efficiency as a function of cavity outer radius at RT 157

6.19 The electric field of the fundamental resonant mode of the optimized cavity at RT. (a) Magnitude of the electric field in XY plane at Z=450 nm (b) in XZ plane at Y=0 (c) z component of the electric field in YZ plane and (d) x and (e) y components of the electric field at XY plane at Z=450 nm 159

6.20 Modal content of the optimized mid-IR cavity. (a-c) The degenerate cavity mode at $\lambda = 4.85\mu m$ with Q=75 (d-e)The fundamental mode at $\lambda = 4.85\mu m$ with Q=118 (f-g) Higher order mode at $\lambda = 2.83\mu m$ with Q=210 and second order degeneracy 161

6.21 The background electric field, a plane wave in **x** direction, shown by white arrows and the normalized magnitude of the scattered field [color plot] from the structure. 163

6.22 The normalized time averaged power flow of the scattered field shown by yellow arrows and the normalized magnitude of the scattered field from the structure [color plot]. . . 164

6.23 Flow chart of the systematic design method of a coaxial cavity 167

6.24 (a) The coaxial cavity resonant wavelength versus ambient refractive index (b) Proposed active region for the coaxial cavity at Mid-IR 168

A.1 ZrO_2 dispersion curve from SOPRA N&K Database [8], its Cauchy fit and experimental ellipsometry data 190

A.2 Ta_2O_5 dispersion curve from SOPRA N&K Database [8], its Cauchy fit and experimental ellipsometry data 191

A.3 Al_2O_3 Sellmeier dispersion curve [9], experimental ellipsometry data and its Sellmeier fit 192

A.4 ZnS Sellmeier dispersion curve [10, 11], experimental ellipsometry data and its Sellmeier fit 193

A.5 YF_3 Sellmeier dispersion curve [12] and its Sellmeier fit, experimental ellipsometry data and its Sellmeier fit. 194

A.6 SiO_2 Sellmeier dispersion curve [9, 13], experimental ellipsometry data and its Sellmeier fit 195

B.1 Contours of constant reflectivity versus film thickness for a double layer YF_3-ZnS ARC for an ICL-3 at λ=3.4μm 197
B.2 Reflectivity curve versus wavelength for a double layer YF_3-ZnS ARC with thickness of 177 nm and 164 nm, respectively. 197
B.3 Contours of constant reflectivity versus film thickness for a double layer ZnS-YF_3 ARC for an ICL-3 at λ=3.4μm 198
B.4 Reflectivity curve versus wavelength for a double layer ZnS-YF_3 ARC with thickness of 244 nm and 344 nm, respectively. 198
B.5 Contours of constant reflectivity versus film thickness for a double layer TiO_2-SiO_2 ARC for an ICL-1 at λ=3.5μm 199
B.6 Reflectivity curve versus wavelength for a double layer TiO_2-SiO_2 ARC with thickness of 330 nm and 200 nm, respectively. 199
B.7 Contours of constant reflectivity versus film thickness for a double layer ZnS-SiO_2 ARC for an ICL-2 at λ=3.8μm 200
B.8 Reflectivity curve versus wavelength for a double layer ZnS-SiO_2 ARC with thickness of 292 nm and 408 nm, respectively. 200
B.9 Contours of constant reflectivity versus film thickness for a double layer ZnS-SiO_2 ARC for an ICL-2 at λ=3.2μm 201
B.10 Reflectivity curve versus wavelength for a double layer ZnS-SiO_2 ARC with thickness of 287 nm and 447 nm, respectively. 201

Chapter 1

Introduction

LASER stands for **L**ight **A**mplification by **S**timulated **E**mission of **R**adiation. Einstein's theory of stimulated emission, i.e. transition of an electronic system to a lower energy through interaction with photons and subsequent generation of new photons that are identical to those of the incident radiation, laid the foundation for the invention of laser [14]. When the first laser was demonstrated in 1960 [15] it was described as "a solution looking for a problem". Now half a century later, lasers have greatly influenced science and technology as well as everyday lives.

Semiconductor lasers are one of the most important category of lasers that provide inexpensive and compact light sources. Although compound semiconductors with direct bandgap provide the basic form of a gain medium, they can only cover certain wavelengths corresponding to the material's energy gap. Quantum well lasers, on the other hand, utilize quantum confinement to tailor the emission wavelength by adjusting the thickness of the quantum wells (QWs). QWs facilitate electron-hole confinement and their quasi-two-dimensional (quasi-2D) density of states near the band edge increases the differential

gain [16]. These properties are the main reason behind the importance of QW lasers and their widespread use in industry.

However, when it comes to long wavelengths in the infrared region, lower density of states and scaling of the optical mode result in less overlap with the active quantum well and lower material gain [16]. Lasing occurs when the overall gain exceeds the total loss. As such, the reduced gain in QWs combined with increased loss factors including free carrier absorption [17] and Auger recombination [18] render QWs inadequate for lasing in the long wavelength region.

Sufficient gain may be achieved by exploiting multiple quantum wells (MQWs) in the active region. Depending on whether the QWs are connected in parallel or in series, this strategy can also improve the threshold voltage or current. Furthermore, the distance between the QWs should be much less than the wavelength, yet they must be sufficiently separated in order to decouple and maintain their 2D density of states [16]. Therefore, inserting thin potential barriers between adjacent QWs provides a straightforward configuration. Consequently for the parallel connection configuration the injected current divides among the wells. The threshold voltages, hence, is minimized and the carrier density scales directly with the number of QWs, designated by M.

Alternatively, injectors can replace the thin barriers to achieve a series configuration. Connecting the QWs in series, where the same current passes through all QWs, increases the differential efficiency, since each QW recycles the charge carriers of the preceding one. The QWs in series, also known as the *cascade*, require a lower current and a higher voltage, wherein the later scales directly with the multiplicity M. Given that Ohmic dissipation

varies quadratically with current, the parallel configuration parasitic loss varies as M^2 whereas that of the cascade configuration is independent of the QW numbers [18]. Therefore cascaded QWs minimize the threshold power density (P_{th}). Moreover, as a consequence of carrier recycling, the differential quantum efficiency (η_d) as well as the internal efficiency (η_i) scale directly with M [2].

The Mid-Infrared (Mid-IR) region of spectrum from 3 to 5 μm, corresponds to an atmospheric transmission window and has diverse environmental, technological and medical applications such as chemical spectroscopy and sensing [19], free-space communications, military countermeasures, bio-molecular sensing [20], and medical diagnosis [21]. All of these applications require a compact and highly efficient semiconductor laser source. In addition, optical detection methods, which enable non-intrusive and real time monitoring, also benefit from a laser source in this range. Sensitivities in the order of part per billion (ppb) will be achievable for gas LIDAR (Light Detection and Ranging) and laser spectroscopy techniques such as Cavity Ring-Down Spectroscopy (CRDS), Intra-Cavity Laser Absorption Spectroscopy (ICLAS), and photo-acoustic spectroscopy detection [19].

The Mid-IR part of the spectrum is particularly important because the fundamental vibration modes of N-H, C-H, and O-H bonds lie in this region. These vibrational transitions are present in all organic molecules and greenhouse gases like methane (CH_4) and butane (C_4H_{10}) [19]. Their strong absorption bands facilitate measurement of low concentrations mixtures. Therefore, coherent light sources will significantly improve trace gas analysis, single molecule detection, biochemical sensing, and other spectroscopic applications.

Mid-IR laser sources also have numerous application in bio-photonics. Due to water

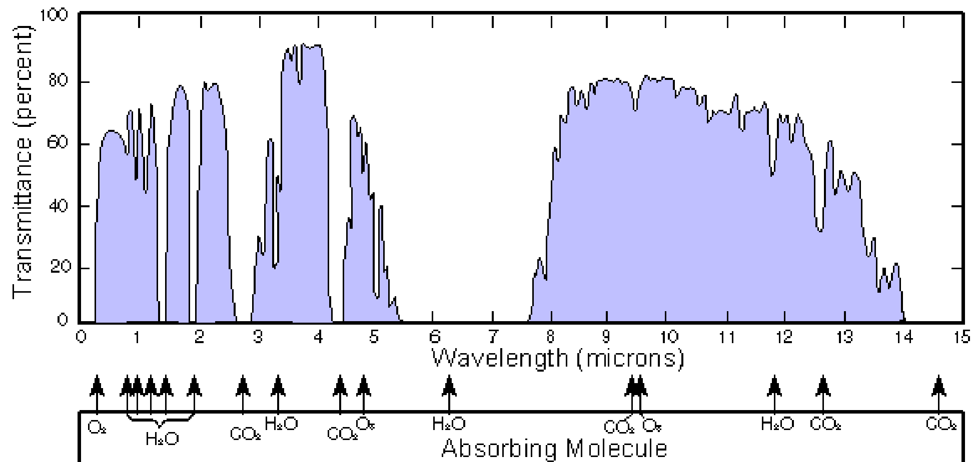

Figure 1.1: Infrared atmospheric "transmission window", adopted from [1].

absorption in this region, which peaks at 3 μm, Mid-IR spectroscopic techniques can be employed in diagnostics and treatment procedures [19]. Water, the principal component of biological substances, is highly absorptive in Mid-IR region due to the presence of O-H bonds. Consequently, the penetration depth of radiation in these frequencies is minimal, which, in turn, allows for tissue ablation and surgeries to be performed with high precision and minimum damage [19]. Mid-IR bio-sensing and imaging devices can be employed in biomedical applications for disease detection and diagnostics by means of safe *in-vivo* techniques [19]. Moreover, high density 2D planar arrays of nano-lasers with digitally tunable emission spectrum can be used for high resolution biomedical imaging of living organisms.

The following lists different types of lasers that have been developed for continuous wave (CW), room temperature (RT) emission in Mid-IR:

- conventional QW lasers,

- quantum cascade lasers,
- type-II interband cascade lasers.

Conventional QW laser diodes suffer from poor hole confinement and high loss at long wavelengths. Nevertheless, high gain associated with intra-well transitions in QWs can offset the temperature-sensitive loss in narrow bandgap materials and result in low threshold current densities. However, rapid thermal rollover still limits the output power [22]. Conventional QW lasers have become the primary infrared source in 2-3 μm wavelength region [16]. For example, CW RT output powers as high as 1.4 W at 2.2 μm has been demonstrated [23]. Recently, there has been much effort to extend the emission wavelength beyond 3 μm. Threshold current densities of 0.6kA/cm^2 were reported for GaSb-based diode lasers at 3.4 μm [24]. Record output powers of 190 mW at 3.1 μm [25] and 15 mW at 3.4 μm [23] show a trend that output power falls as the wavelength increases.

The well-known quantum cascade laser (QCL) performs best in the wavelengths above 4 μm. Infrared QCLs are usually comprised of 30-40 stages [17], providing high output powers at the expense of high threshold power densities. QCLs utilize the intersubband transition within the conduction band (CB) states. Therefore, electrons are the only carrier used in the light generation process and consequently they are considered as unipolar lasers. The independence of the emission wavelength from material bandgap has enabled the development of long-wavelength lasers based on wide-bandgap materials like GaAs and InP, which not only enjoy a mature technology but also possess advantageous thermal properties [26]. One of the fundamental characteristics of QCLs is the short carrier lifetime at the upper lasing level which is limited by optical phonons and surface roughness scattering [17]. The small coupling efficiency between the lasing mode and spontaneous emission is a direct consequence of this picosecond (ps) lifetime, which, in turn, results in

a very narrow line-width for QCLs [27].

Although QCLs were first demonstrated at $\lambda = 4.2\ \mu m$ in 1994 [26], much of the progress has been made at the long-wavelength region of infrared. Within 3-4 μm range, QCLs suffer from inadequate conduction band offset, which causes poor electron confinement and carrier leakage, and results in excessive currents and thermal management problems [21]. QCLs have achieved 5 W of CW RT output power with wall plug efficiency (WPE) of 21% at 4.9 μm. The reported threshold current density (J_{th}) at this wavelength is 1.25 kA/cm^2. At 3.7 μm the CW output power at RT decreases to 1.1W with 6% WPE and J_{th}=1.67 kA/cm^2. This trend continues for $\lambda = 3.4\ \mu$m, 3.2 μm and 3 μm with CW output powers of 403 mW, 20 mW and 2.8 mW, respectively. The threshold current density for devices emitting at 3 μm reaches 2.4 kA/cm^2 in spite of high reflectivity (HR) coated back facet and partially high reflectivity coated (PHR) front facet [21].

Mid-IR type-II Interband Cascade Lasers (ICLs) combine the interband transition of QW lasers and cascading of QCLs in a type-II broken gap alignment. The invention of ICL by Yang dates back to 1995 [28]. He proposed an active region based on type-II broken gap alignment which naturally occurs in InAs/GaSb material system and was termed "leaky quantum well approach". Lining up the GaSb valence band minimum slightly higher than the InAs conduction band maximum provides a"leaky window region" which enables the spatial overlap between conduction and valence bands [28]. The laser core was comprised of many active region connected by injection regions to enable electrical pumping [28]. Soon after this proposal, it was shown that adding a second GaSb well to the active regions improves the design [29]. The additional GaSb well was designed sufficiently wide to impede the carrier leakage via inter-valence transitions. This adjustment did not affect the

optical transition rate, whereas altering the first well would have reduced the electron-hole wave-function overlap [29].

The ICL active region has evolved from the original idea. A type-II W-design [29] featuring a GaInSb hole well surrounded by two InAs electron wells with enhanced optical gain constitutes today's ICL active regions [2]. ICLs, unlike any other semiconductor lasers, generate carriers internally at the electron-hole injection region interface. The conduction-valence band overlap, a character of type-II alignment in the GaSb/InAs material system, creates a semi-metallic interface in the presence of an electric field. Carrier generation at this semi-metallic interface is controlled by quantum confinement as well as the applied bias and serves to maintain the population inversion [16]. ICL is the only currently used laser with this feature [2].

The number of cascaded active regions has decreased from 18 in early ICLs [30] to 5-7 in the recent devices [17]. This reduction has provided a balanced design capable of RT operation and is in direct contrast to QCLs with several tens of stages in the laser core. Another fundamental distinction between ICLs and QCLs is their upper lasing level carrier lifetime. Nano-second (ns) carrier lifetime in ICLs is determined by Auger recombination process, which greatly differs from that of QCLs. Therefore, an ICL requires lower threshold current density [2].

Dedicated research efforts from several groups around the world, such as Naval Research Laboratory (NRL), Maxion/University of Maryland(UMD)/University of Waterloo (UW), Jet Propulsion Laboratory (JPL)/NASA, and University of Würzburg, resulted in the ICL progress over the past decade [2, 3, 16, 17, 30–52]. ICLs have reached RT CW

operation over the entire 3-5 μm spectrum with max output power of nearly 0.5 W at 3.7 μm [17]. Maximum WPE of 15% at room temperature [49] and maximum CW temperature of T_{max}^{CW}=118°C [50] has been reported. ICLs can operate with threshold powers as low as 29 mW [2] and threshold current densities as low as 100 A/cm^2 [52] at RT.

Low threshold voltage and current densities are a fundamental feature of ICLs and are not reliant on cavity design [16]. For chemical sensing application, power levels as low as ~1 mW are sufficient, which means laser is operated close to threshold. Thus, for battery operated applications that require minimal power consumption levels, ICLs are preferred to QCLs [17] due to ICL's low threshold power densities, 0.35kW/cm^2 [2] versus that of QCL's, 10kW/cm^2 [21].

Continuous-wave room-temperature operation of ICLs is not trivial and was not realized at the start of this project. Much effort have been made throughout the course of the project to improve the device performance. These efforts include various design optimization. The doping level adjustments have been made in several epitaxial layers such as electron injector and separate confinement regions. Novel active regions, such as a δ-strained ICL, were designed and tested. Similarly, the associated fabrication techniques were developed and perfected. Optical coatings, including high-reflectivity and anti-reflectivity coating, were also investigated. Special efforts were dedicated to anti-reflection coating to improve the output power of the ICLs. The experimental results associated with these optimizations will be discussed in the following chapters.

Chapter 2 outlines various design aspects of ICLs and compares it to those of QCLs in detail. The discussion on the fundamental underlying physics of the ICLs is essential

for understanding the different design optimization schemes that are discussed later on. Chapter 3 describes the fabrication techniques and their effect on the device performance. Novel fabrication methods are described and their effects on the device performance is discussed. Chapter 4 summarizes experimental design and characterization results. In this chapter, several successful design changes together with the associated experimental analysis are reviewed. Design, fabrication and characterization of anti-Reflection (AR) coatings for high power operation are the subject of Chapter 5. Several dielectric materials have been considered for anti-reflection coating and been characterized experimentally. Most promising materials have been selected for investigation of laser performance before and after the application of ARCs. This study has also been used to investigate the internal laser parameters and provided insight to the fundamental underling mechanisms in laser performance. Chapter 6 describes the design and simulation of novel sub-wavelength mid-IR lasers. These devices have been introduced for the first time in the Mid-IR region in this work. A systematic design approach for sub-wavelength cavities is developed that is applicable to any wavelength in general. Important cavity merit such as quality factor and confinement factor are discussed and related to laser parameter. Optimum cavity at $\lambda = 3.6\mu$m is then designed and studied and the chapter concludes with the application of such devices.

Chapter 2

Interbound Cascade Laser - Design and Simulation

2.1 Cascade or Non-Cascade

Multiple quantum wells (MQWs) are needed to provide sufficient gain to overcome the cavity and material losses in Mid-IR wavelengths. These QWs can be connected either in parallel or series, more commonly known as cascade. When QWs are connected in parallel, as is the case in a conventional MQW diode laser, the electrons are injected into the conduction band from the n-contact and holes to the valence band from the p-contact and they divide between the quantum wells, where they recombine through radiative and/or non radiative processes. In order to reach threshold, every quantum well must provide a certain amount of gain, $g_{th,m}$, and the combined gain should exceed the total loss. If $J_{th,m}$ is the required current in each QW which yields $g_{th,m}$, then the total current at the contacts will become $MJ_{th,m}$, where M is the number of quantum wells.

In cascade configurations, the injected carriers cross all the QWs one by one. Upon reaching each stage, carriers make a transition in the active well in that stage and move onwards. Therefore, the total current is the same as the threshold current in one QW, i.e. $J_{th,m}$ [16],

$$J_{th} = M J_{th,m} \qquad \text{non-cascade,} \tag{2.1}$$

$$J_{th} = J_{th,m} \qquad \text{cascade.} \tag{2.2}$$

On the other hand, to reach the threshold condition the voltage drop in each QW has to be larger than the photon energy, $E_g = \hbar\omega$, by a margin of ΔE, that is determined by the total loss [2], analogous to Bernard-Duraffourg condition in conventional diode lasers. In the parallel configuration, all QWs share common upper and lower lasing level, between which the radiative transition occurs. Yet in the cascade scheme, the upper lasing level of each stage should line up with the lower lasing level of the preceding stage. Therefore, the threshold voltage in the series scheme is M times that of the parallel configuration,

$$V_{th} = \frac{\hbar\omega + \Delta E}{q} \qquad \text{non-cascade,} \tag{2.3}$$

$$V_{th} = M\frac{\hbar\omega + \Delta E}{q} \qquad \text{cascade,} \tag{2.4}$$

where q is the electron charge [16].

Combining the voltage/current requirement in both settings **does not** present an advantage from the threshold power P_{th} point of view. It is only in the presence of a series resistance that the difference becomes apparent. The current passing through the parasitic series resistance in a conventional QW laser is, thus, M times that of the cascade laser

current. The dissipated power will be quadratic in current [16], i.e.,

$$P_{th} = \frac{\hbar\omega + \Delta E}{q} M J_{th,m} + \rho M^2 J_{th,m}^2 \qquad \text{non-cascade,} \tag{2.5}$$

$$P_{th} = \frac{\hbar\omega + \Delta E}{q} M J_{th,m} + \rho J_{th,m}^2 \qquad \text{cascade.} \tag{2.6}$$

As Eq. 2.5 implies, the contribution of the first term in the right hand side decreases relative to the second term for long wavelengths. This effect becomes more pronounced in view of high threshold currents predicted for Mid-IR lasers. Therefore, the cascade-lasers seem preferable as they decrease the contribution of the parasitic loss [16].

2.2 ICL and QCL, a Comparison

Cascade lasers were introduced with QCLs in 1994 [26], which is the most well-known laser of this class. ICLs also belong to the cascade category of semiconductor lasers. ICLs and QCLs fundamentally differ in their underlying mechanism of light emission. In QCLs, intersubband transitions between the conduction sub-bands of QWs are responsible for emission, whereas ICLs emit photons due to the interband transition between the conduction and valence bands. This fundamental difference causes major distinctions between ICLs and QCLs. For ICLs most of the holes reside in the lowest sub-band, therefore, heavy hole characteristics dominate the optical matrix element and result in Transverse Electric (TE) emission [53]. For QCLs the conduction to conduction band transitions dominate; therefore, the only non-vanishing optical matrix element is along the growth direction [53]. This leads to Transverse Magnetic (TM) polarized emission.

Another major consequence of the different transition mechanism in ICLs and QCLs

is the carrier lifetime. The upper level lifetime for intersubband transition is restricted by optical phonon and intersubband scattering, which is empirically found to be in the picosecond (ps) range. In contrast the upper state lifetime in interband transitions is governed by Auger recombination, with lifetime of the order of nanosecond obtained from empirical data [17]. As a result of the disparity between carrier lifetimes in these two types of laser, an ICL exhibit a differential gain per current density two orders of magnitude greater than that of a QCL. Therefore, ICLs can reach the gain required for lasing with far less number of stages than their cascade counterpart and, thus, can operate with a much lower voltage [17]. QCLs typically require at least 30-40 stages to sufficiently reduce the current densities for CW operation [17], while the number of cascaded active region in ICLs is between 5-12 [2]. The relevant voltage values range from 10 V to 15 V for QCLs and from 2 V to 3 V for ICLs [2].

Another consequence of the short carrier lifetime in QCLs is a higher threshold current density [2], which tends to increase at wavelengths below 4 μm due to surface roughness scattering and carrier leakage [17]. QCLs current densities are in the order of 1 kA/cm^2 while current densities as low as 100 A/cm^2 have been observed in ICLs [52]. Combining the current and voltage ratios, the threshold power density in QCLs can be 30 times higher than that of an ICL [17]. QCL threshold current density can be reduced by incorporating more stages, at the expense of increasing threshold voltage and power density [17].

QCLs also require higher voltage margin ΔE in addition to photon energy, Eq. 2.5. An additional voltage drop per stage of many $K_B T$ is required in QCLs in order to prevent thermal population of the lower lasing level [54], whereas ICLs voltage margin only needs to overcome the total loss [2]. QCL voltage margin at each stage, is about 100-150 meV com-

pared to 30 meV for ICLs, which is in the order of thermal energy at room temperature [17].

Nevertheless, QCLs are grown on wider bandgap substrates, such as GaAs and InP, which have a significant advantage from the thermal point of view. For example, they allow for cascading many stages whilst maintaining an efficient heat removal from the laser core. ICLs on the other hand are antimonide-based lasers; thus, the number of stages are limited if RT operation is to be realized. The wide bandgap and less temperature sensitive material system of QCLs also means that even though the carrier lifetime is much shorter in QCLs, it has a much weaker temperature dependence than the carrier lifetime in ICLs. Therefore, QCLs usually have higher slope efficiency and can operate at much higher temperatures [2].

It is worth noting that since QCLs performs best at wavelengths above 4 μm and ICLs in 3-4 μm the compared characteristics in the text refer to devices emitting at 4 μm where comparison is most meaningful. Based on this comparison, it can be concluded that QCLs are best suited for high temperature and high power applications whereas ICLs are ideal for compact systems and battery operated field applications where moderate powers are sufficient [17].

2.3 ICL Operation Principles

Interband cascade laser core consists of 5-12 stages. Each stage includes an active region, a hole injector, and an electron injector, Fig. 2.1. The electrons that are injected from the n-contact are confined in the active region conduction band where they make a radiative or non-radiative transition to the valence band. They will then pass through the hole injection valence band and transfer to the conduction band at the electron/hole injector

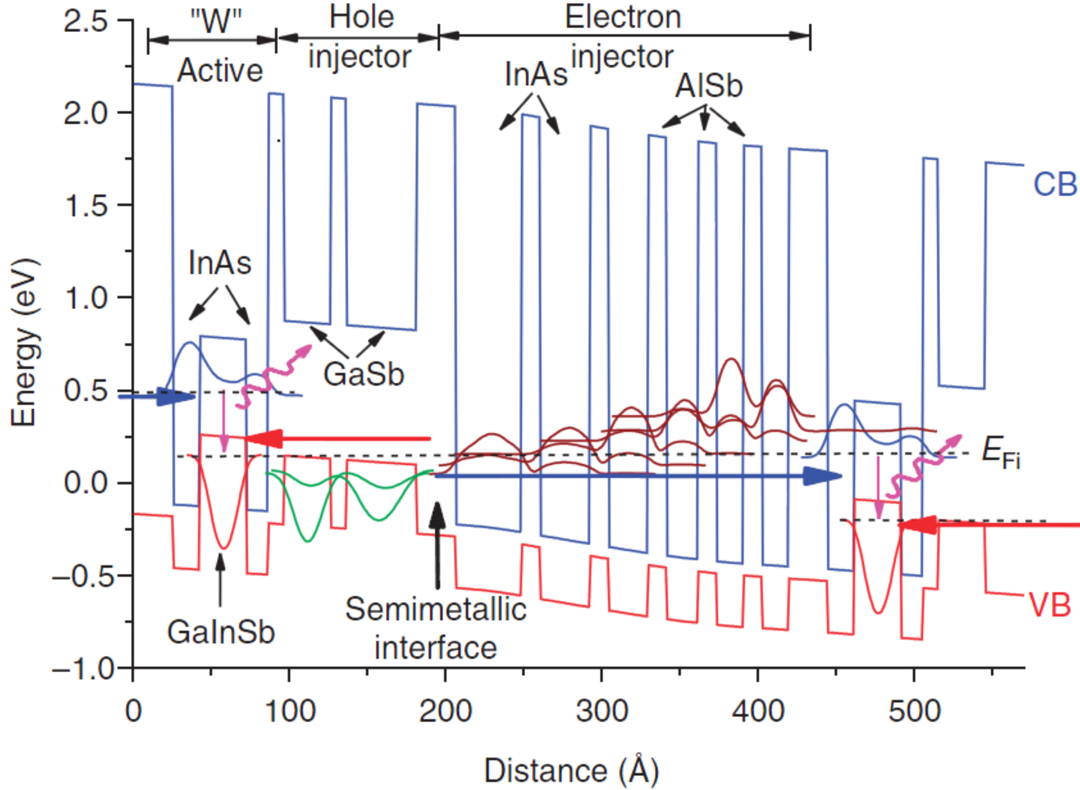

Figure 2.1: Interband cascade laser band structure and relevant electron/hole wavefuctions, Reprinted by permission from Macmillan Publishers Ltd: nature communications [2], copyright © 2011.

interface and will be injected to the next active region subsequently. Having passed all the cascades, they will be collected at the p-contact. In the two following subsections the active and injection region will be discussed in detail.

2.3.1 Active Region

As seen in Fig. 2.2, the active region of an ICL, where the photon emission takes place, has a W-shaped band diagram which is created by a GaInSb hole-well (h-well) surrounded

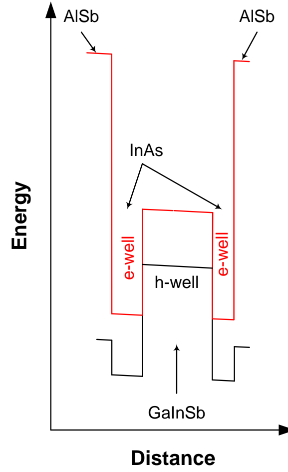

Figure 2.2: Interband cascade laser W-shaped active region.

by two coupled InAs electron-wells (e-wells). The electron/hole wave-function overlap determines the transition rate and is only considerable in the h-well. The two InAs e-wells have slightly different widths to compensate for the wave-function shift in the presence of applied voltage, i.e. quantum-confined Stark effect, and maximize the transition rate. The presence of indium (In) in the composition of h-well imposes a compressive strain on the lattice, which, in turn, results in a higher-energy heavy-hole (HH) sub-band. Therefore, the optical transition with the Mid-IR energy of 0.3 eV-0.4 eV can be attained with thinner e-wells. Reducing the thickness of InAs layers will contribute to a larger optical matrix dipole [16]. The emission wavelength is tuned by adjusting the InAs active e-well thickness.

2.3.2 Electron/Hole Injector and Semi-Metallic Interface

In a cascade scheme, the electron and hole injectors function as a downward staircase that facilitates the alignment of the lower lasing level in each stage with the higher level of the

next. They also contribute to the length of the cascade unit cell and enable the application of minimum required voltage per stage (0.3-0.4 V in Mid-IR) without having to surpass the maximum field/unit length that is allowed by the material system. Since, the electrons have higher mobility than holes, electron injectors usually constitute most of the active region unit cell [16].

In Mid-IR ICLs, the electron injector is composed of InAs e-wells separated by AlSb barriers. The hole injector consists of GaSb h-wells that are also separated by the same barrier type. GaSb, known as intermediate gap semiconductor, has an energy gap of E_g=0.812 eV [55]. The temperature dependence of the bandgap is often characterized experimentally with two fitting parameters α and β, i.e.,

$$E_g(T) = E_g(0) - \frac{\alpha T^2}{T + \beta}, \tag{2.7}$$

where α=0.417 meV/K and β=140 K have been reported for GaSb [55].

InAs is a relatively small bandgap semiconductor, E_g=0.4 eV, with the temperature dependence parameters α=0.276 meV/K and β=93 K. Comparing these values to industry standard materials such as GaAs with E_g=1.5 eV, α=0.5405 meV/K and β=204 K or InP with E_g=1.4236 eV, α=0.363 meV/K and β=162 K, it is evident that the devices incorporating InAs are much more sensitive to temperature variations.

However, the motive behind the use of InAs is its special band alignment with GaSb. The InAs/GaSb material system exhibits a Type-II broken alignment [55], where the conduction band of InAs is ~0.21 eV lower than the valence band of GaSb [2], Fig. 2.3. Even though quantum confinement leads to an indirect positive band gap of E_g in adjacent

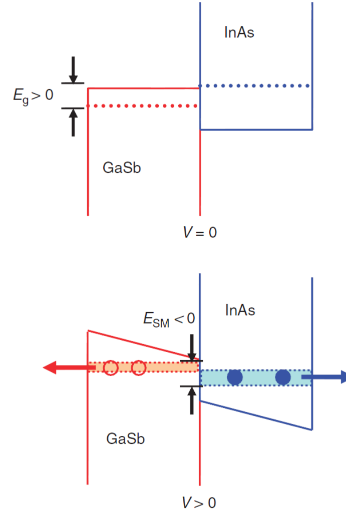

Figure 2.3: InAs/GaSb Type-II broken gap band alignment, Reprinted by permission from Macmillan Publishers Ltd: nature communications [2], copyright © 2011.

GaSb/InAs QWs and induces semiconductor characteristics in the junction, applying electric field can change the band alignment type from semiconducting to semi-metallic [2]. Junction bias will generate a negative band overlap of E_{SM} that allows for population of electron and holes in their respective wells at quasi-equilibrium [2].

As for any other cascade lasers, it is required that the lower lasing energy level of each stage lines up with the upper lasing level at threshold. For an ICL wherein interband transition is essential, the upper (lower) lasing energy level is the quasi-Fermi level of electron (holes) in the active QWs. Therefore, the quasi-Fermi level of the active h-well, the hole injector, and the electron injector of each stage must be equal to that of the active e-well in the next stage, as shown by the dashed line in Fig. 2.1 [2].

In the presence of an applied voltage, V, a band overlap of E_{SM} at the semi-metallic interface is induced. Assuming a common Fermi level for electron and hole injector as

well as across the semi-metallic interface, the Fermi energy for electron and holes has the following value [16],

$$E_f \approx E_{\mathrm{SM}} \frac{m_r^*}{m_e^*} + E_c, \tag{2.8}$$

where m_r^* is the reduced mass, $m_r^* = (m_e^* m_h^*)/(m_e^* + m_h^*)$, and m_e^* and m_h^* are the electron's and hole's effective mass. Taking a 2D density of state for both carriers, g(E)=$4\pi m_{e/h}^*/h^2$, at zero temperature, the field induced carrier density is [16],

$$n = p = \int g(E) dE = \frac{4\pi m_r^*}{h^2} E_{\mathrm{SM}}. \tag{2.9}$$

The Fermi level can alternatively be evaluated from at valence band edge, which results in an equivalent expression for the carrier density. Therefore, the semi-metallic electron-hole injector interface generates equal number of electrons and holes. Holes are then supplied to the valence band to maintain population inversion and electrons are injected to the next stage as if they are recycled from the preceding stage [16]. Interband cascade laser is the only current laser capable of internal generation of carriers [2].

Simulations using an 8-band **k.p** model and self-consistent calculation of conduction and valence band and Poisson's equation in the presence of an applied field [53] yields a threshold carrier density of $n_{th} = 1.5 \times 10^{12}$ cm^{-1} for interband transition in a W-shape ICL active region [16]. The generation of this threshold carrier density requires a threshold overlap energy of $E_{\mathrm{SM,th}} = 130$ meV at 300K [16].

On the other hand, the required voltage per stage should ideally exceed the photon

energy by no more than a few K_BT. Therefore the threshold voltage per stage is [16],

$$V_m = \frac{\hbar\omega + K_B T}{q}, \tag{2.10}$$

where q is the electron charge. In an ideal design, this voltage should be equal to the voltage needed for creating the semimetallic band overlap required for generation of the threshold carrier density [16]. If the required voltage per stage is more than what is needed for generating the threshold carrier density, accumulation of extra carriers will cause additional Auger recombination and free carrier absorption. In contrast, insufficient potential difference will result in inadequate carrier generation and a higher than necessary threshold voltage. As the overlap energy is controlled by quantum confinement and electron-hole center of mass distance, the design and doping of the injectors are parameters for optimizing the performance by the designer [2].

Insofar as the density of states in the electron injector is very high, most of electrons will accumulate in the injector QWs rather than the active QWs, whereas holes are mostly directed to the active region. Under such circumstances, the unbalanced carrier concentration in the active region increases the free carrier absorption loss. Doping the electron injector with silicon can balance the electron-hole concentration and has been shown both theoretically and experimentally to improve the laser performance [2]. A balanced carrier concentration means that more of the available electrons and holes will contribute to the gain, thereby increasing the material gain. Subsequently, a considerably lower threshold current density will be obtained. Slight threshold voltage improvement are also achieved as no extra voltage is required to compensate for unequal number of the carriers. Furthermore, the reduction in carrier recombination reduces the waveguide internal loss [2].

Each cascade stage of an ICL is about 450 Å thick. Moreover, empirical studies show that the tradeoff between the thermal considerations and gain requirements results in the optimum number of stages be equal to five [16]. Therefore the ICL's active core has thickness of about 200 nm.

2.4 δ-Strained Quantum well

In pursuit of an ICL design to provide higher gain, increasing the number of electron and hole wells in the active region was considered. Figure 2.4a shows a cascade unit cell for such a novel ICL design with three e-well and two h-wells. The idea behind this design was to increase the optical matrix element by increasing the optical transition pathways and was inspired by former work done in the group [56]. However, simulations showed that the HH wave-function exhibits anti-symmetric parity, whereas the conduction band wave-function remains symmetric. The overlap of the two in the first well then cancels out that of the second well and, therefore, the extra hole well does not improve the device performance. This design was subsequently modified by replacing the middle electron well with an InAs barrier, as shown in Fig. 2.4b, in order to reduce the energy spacing between the higher symmetric and anti-symmetric wave-functions in the conduction band, thereby enhancing the optical dipole element and increasing the gain. The Current-Voltage-Light (IVL) characteristic for the grown and fabricated devices from this design are reported in chapter4.

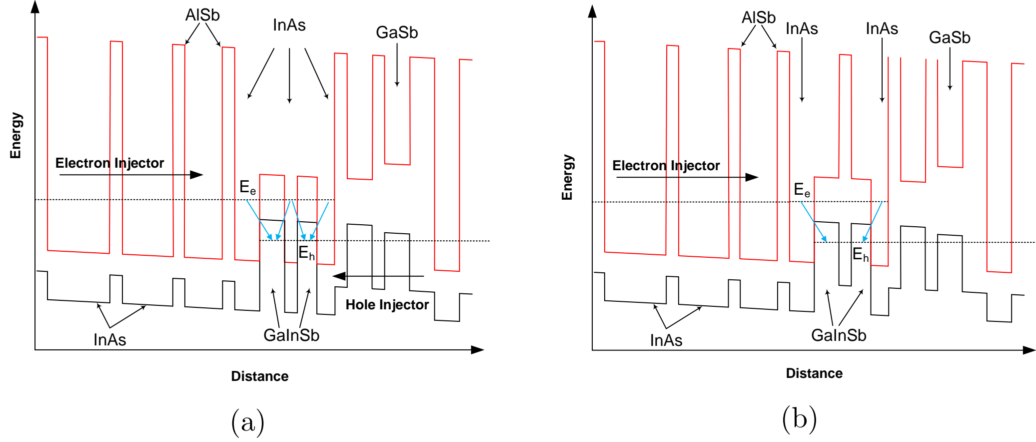

Figure 2.4: δ-Strained quantum well band structure (a) initial and (b) final design

2.5 Optical Mode and Waveguide Design

The ICL waveguide design is another important aspect of the final device as it affects the internal loss and subsequently the required gain to reach threshold. The ICL core consists of the active region and the electron and hole injectors and has an average refractive index of 3.58. However, due to the high refractive index of GaSb substrate, 3.75, many stages will be required to confine the mode to the active region. On the other hand, in order to extract heat efficiently from the active region and prevent the thermal rollover, a minimum number of stages must be used [16]. Therefore in order to confine the optical mode, the active region has to be optically isolated from the substrate using thick lower cladding. The lower cladding needs to have a higher band gap, lower refractive index and be lattice matched to the substrate. However, no such material exists. The problem is solved by using a superlattice consisting of many alternate layers. The active region is also sandwiched between two GaSb separate confinement regions (SCRs) to pull the mode further into the laser core. Moreover, to avoid excessive waveguide loss due to the interaction of the mode with the contact, another low index cladding regions separate the laser core from the metal

contact on the top. Cladding layers consist of InAs/AlSb supper-lattice with an average refractive index of n=3.25 [16]. The layer structure of a typical ICL is schematically shown in Fig. 2.5.

When no gain or loss is present, the transparency condition reads, $\Gamma_a g_{tr} = \alpha_i$, where,

$$\alpha_i = \Gamma_a \alpha_a + \Gamma_s \alpha_s + \Gamma_c \alpha_c, \tag{2.11}$$

is the total waveguide internal loss, in which Γ and α denote the confinement factor and loss, respectively, with the subscript referring to the active region (a), the SCR (s) and the cladding (c). The total loss can be viewed as the weighted average of the material loss in different layers and $\Gamma_a + \Gamma_s + \Gamma_c = 1$ [16].

Minimization of internal loss and the transparency condition requires two different strategies. Since the wide bandgap GaSb SCRs have the lowest loss value, higher confinement factor in this region will reduce the internal loss. Narrow bandgap materials and large hole density are responsible for relatively high losses in the active region, whereas high doping and interface roughness scattering of the supperlattice introduce high losses in cladding [16]. Nevertheless, confining the mode in the SCRs increases the transparency

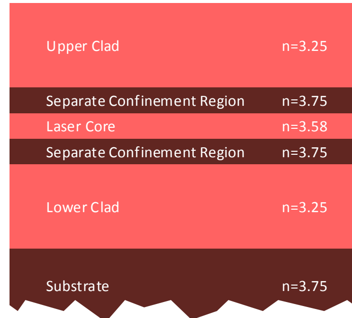

Figure 2.5: ICL layer composition and the corresponding refractive indices

gain and is not desired [16]. To confine the mode in the active region, moderately thick SCRs should be used to balance the transparency gain and the internal loss. The thickness of SCRs in the state of the art ICLs are about 500 nm which coincides with equal losses in all the three regions [5, 16].

The cladding thickness is determined based on the assumption that the losses due to the mode interaction with the substrate on one side and the contact on the other, must not become more than 1 cm^{-1} higher than the loss of infinitely thick cladding [16]. Mode simulations show that in order to meet this condition, the thickness of the top clad should be around 1.6 μm and that of the bottom clad around 2.9 μm. Figure 2.6 depicts the RSoft simulation of the mode profile for a 5-cascade ICL at 3.8 μm with the aforementioned thickness for the SCRs and top/bottom claddings. The simulations are performed with RSoft BeamPROP simulator [57] with grid size 0.05μm. As shown in Fig. 2.6b and Fig. 2.6d the presence of the SCH creates a dip in the mode shape. This behavior further illustrates the sensitivity of the design to the thickness of the SCH layers. It is also apparent for the Fig. 2.6d that this design minimizes the interaction of the mode with the substrate or contact layers. It should be noted that the thickness of these layers have been optimized for 3.8 μm and will scale with λ when the wavelengths is varied.

Inasmuch as the underlying physics of ICLs is very complicated, the summery presented in this chapter may be complimented with the invaluable insights gained from the characterization of operational devices and will illuminate the way for further progress. These experimental methods will be discussed in the following chapters.

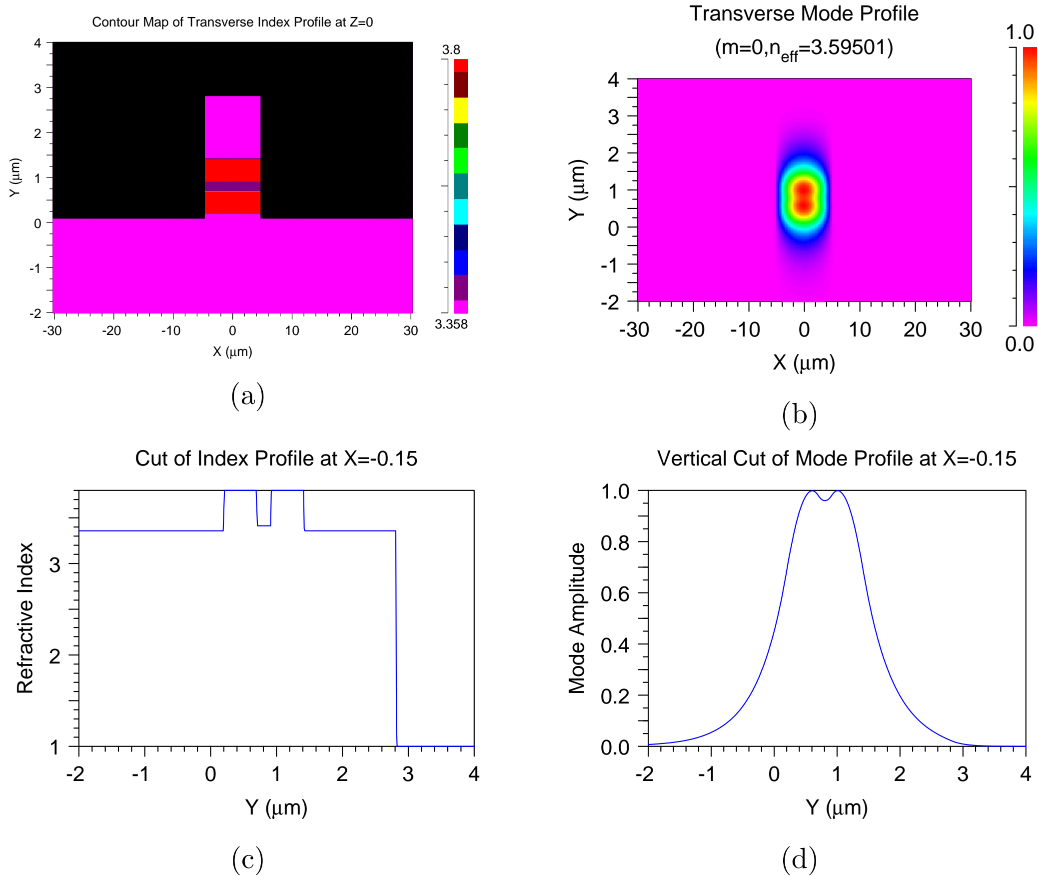

Figure 2.6: Rsoft simulation results: (a) 2D refractive index map of an ICL waveguide with 10 μm width and 3 μm height (b) fundamental mode profile (c) 1D refractive index map (d) 1D cut of the fundamental mode.

Chapter 3

Device Fabrication and Packaging

3.1 Introduction

Fabrication is one of the most important steps in any device study. It can affect or determine the device performance and/or lifetime. Laser fabrication is often more challenging and sensitive to fabrication skills and conditions when compared to other semiconductor devices. The fragility of III-V materials usually used in light emitting devices combined with sample thinning and cleaving steps required for high quality mirror finish of Fabry-Pérot lasers contribute to complexity of the device manufacturing. Moreover, special consideration such as temperatures sensitivity or reaction with chemicals should be taken into account for fabrication of multi-layer structures such as ICLs. This chapter describes the processes involved in the fabrication of ICLs.

3.2 Step by Step Fabrication Process

The device fabrication started with dicing the wafer into 1 cm × 1 cm samples using a diamond scriber. The sample were then subjected to general solvent cleaning that included rinsing with acetone and then with methanol and isopropanol for 30 seconds each. After blow-drying with nitrogen, the samples were transferred to a 150 °C oven, where they were baked for 10 minutes. This step removes any residual moisture on the individual segments and prepares the surface for the photolithography step. In order to ensure that no organic material remained on the surface, the samples were exposed to an oxygen plasma with RF power of around 100 W that was low enough not to damage the top surface. Cleaned samples were then directly transferred to the Plasma Enhanced Chemical Vapor Deposition (PECVD) chamber where 0.8 μm of SiN was deposited on the sample with a deposition rate of ≈ 170 Å/min. This SiN layer served as the etching mask for the subsequent etching steps. The deposition recipe is as follows:

Plasma: LF power 23 W, 7 seconds Pulse time; RF power 20 W, 13 seconds Pulse time

Gas combination: 5%SiH_4 (Silane) and 95%N_2: 400sccm; NH_3: 20sccm.

where LF power and RF power stand for low frequency and radio frequency power, respectively. At this point the samples were patterned with the waveguide mask. In this and all the following photo-lithography steps AZ®5214E, a high resolution image reversal photo-resist from AZ® electronic material, was used.

Next, patterned samples were etched using an Oxford fluorine-based inductive couple plasma (ICP) etcher and the photo-lithographic pattern was transferred to the underlying dielectric. The SiN etching recipe with 4000 Å/min etch rate had the following gas and

power combinations:

Plasma: RF power:50 W; ICP power: 300 W,

Gas combination: SF_6: 40 sccm; O_2: 5 sccm.

where ICP power stands for inductively coupled plasma power. The photo-resist was then removed using a 3 step solvent cleaning process, identical to the one used for initial cleaning, and followed by an exposure to oxygen plasma. The oxygen plasma cleaning was necessary since part of the photo-resist had been polymerized during dry etching and might not be removed using a simple solvent rinse.

An SEM image of the etched SiNwaveguide mask is shown in Fig. 3.1. This particular design, usually referred to as the double trench structure, provides mechanical stability for epitaxial-side (epi-side) down mounting of individual devices. Detailed design criteria for waveguide mask are explained in section 3.3.

The SiN mask was then used to etch the waveguides. Wet or dry etching techniques can be used to define the device features, each subjected to its own limitations. Dry etching combines the chemical and physical etching by utilizing bombardment of ions of the reactive gases. These ion bombardment provides relatively perpendicular waveguide sidewalls but leaves behind a rough footage that contributes to the waveguide scattering loss. Conversely, wet etching typically results in a smooth surface, but the sidewalls are more slanted. The most important disadvantage of wet etching for any multi-layer substrate such as ICLs is the peripheral etching that comes with etch techniques where chemical reactions are dominant. When substrates that are comprised of different materials are exposed to a

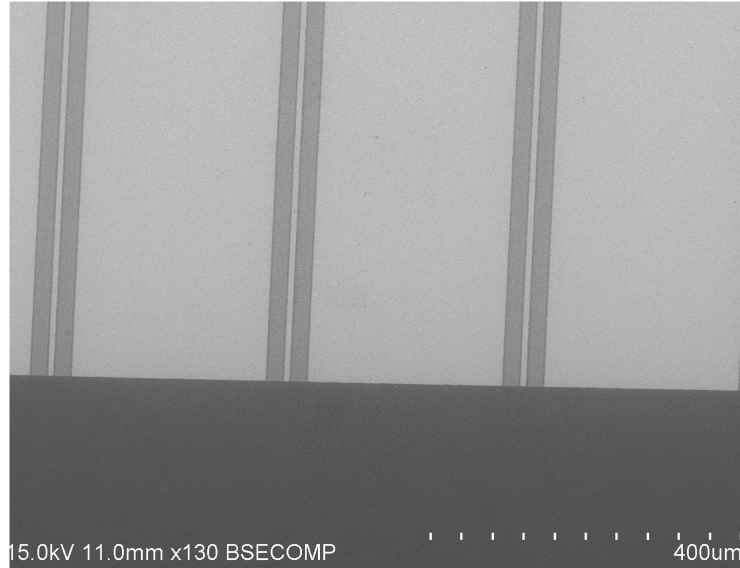

Figure 3.1: Double trench laser waveguides

chemical, each of the layers are etched with different speed, some more than others. Such features not only contribute significantly to the waveguide loss but also create air gaps and prohibit the heat extraction from the active region. Therefore, dry etching seems to be a more appropriate technique for device definition. Nevertheless, a brief wet etching could be used to ameliorate the side wall roughness, and experimental results show that it does lower the waveguide loss.

Therefore, in fabrication of our ICLs, dry etching was followed by 20 second wet etching and 30 second DI water rinse. For dry etching, an OXFORD Chlorine based ICP etcher was used with the following combination of gases and RF powers with the etch rate of about 5500 Å/min:

Plasma: RF power:100 W; ICP power: 400 W,

Gas combination: Ar: 2.5 sccm; BCL_3: 12.5sccm.

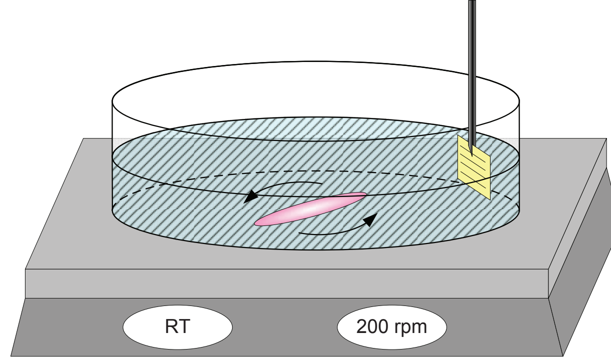

Figure 3.2: Wet etching configuration

For the wet etching, 5 grams of tartaric acid ($C_4H_6O_6$) dissolved in a mixture of phosphoric acid (H_3PO_4): hydrogen peroxide (H_2O_2): deionized water (DI), 30 ml : 30 ml: 90 ml by volume was used. This solution was prepared in advance and stirred at 200 rpm for at least 30 minutes prior to use. During the etch, the waveguides were oriented parallel to the flow of the etchant, thereby creating a flow that smooth outs the sidewalls as illustrated in Fig. 3.2.

Once the waveguides were etched, the SiN mask had to be removed. Part of SiN would be etched during the dry etching of the waveguides. However, the recipes were further refined to achieve a good selectivity between the dielectric and III-V material. Therefore, SiN etch was considerably slowed down relative to that of the substrate, to approximately 900 Å/min. After the completion of the waveguide etch, the remaining SiN on the substrate was removed by dry etching using the same SF_4-based recipe used to etch the mask in the first place.

Clean substrates were investigated using an optical microscope to make sure that all the previously deposited SiN was removed. They were then immediately transferred to the

PECVD chamber for another SiN deposition at 200 °C with the same recipe mentioned earlier. The thickness of this layer was 3000 Å and was deposited over roughly 20 minutes. This layer would serve as the passivation layer for the device. The thickness of this layer is of critical importance. If it is too thick, its isolating characteristic will prevent the heat dissipation from the active region and if it is too thin, there is a chance that devices are shorted through SiN pinholes or cracks on the sidewalls. Fortunately, the conformal characteristics of deposited dielectric layers with PECVD ensures an even dielectric layer even on the vertical sidewalls. Nevertheless, it is important to deposit adequate thickness to achieve a suitable coverage. The minimum reliable thickness was found to be 3000 Å through empirical studies.

Another photo-lithography step was performed on the passivation layer to open windows on top of the waveguides though which the Ohmic contact would be made later. As shown in Fig. 3.3 the dielectric opening had to fall exactly on top of the waveguides along the 1 cm sample. Any misalignment that caused the window to extend over to the sidewalls would short the lasers. Therefore, accurate angular alignment of the two masks was very important. After patterning the dielectric opening, SiN was etched at the openings and the photo resist was removed by solvents and oxygen plasma.

The next fabrication step was making the Ohmic contact. Since each waveguide would become an individual device it should be electrically isolated from the neighboring waveguides to allow for laser bar measurement. A third photo-lithography was then performed to selectively protect an area between each two waveguide from metalization. However, there is a fundamental difference between this photo-lithography and previous ones. In this step instead of etching the open areas, the metal layers were deposited on top of the

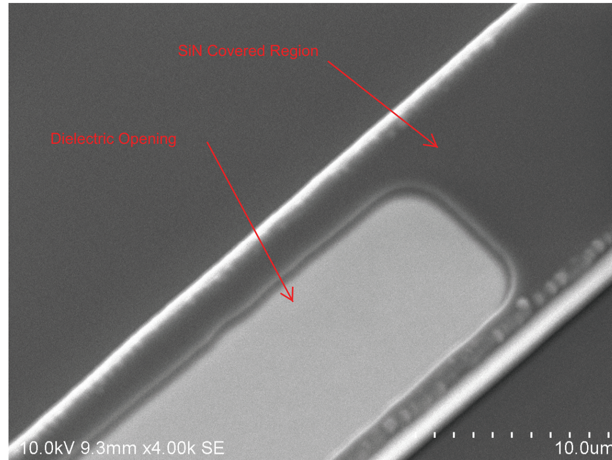

Figure 3.3: Dielectric Opening on top of the laser waveguide

photo-resist and then the left-over photo-resist is removed by the aid of organic solvents. Therefore, it was essential that the solvent reached the photo-resist in places that had to be removed.

Image reversal lithography with a positive or negative photo-resist are both compatible with this process. AZ®5214E that had been used in the prior steps was formulated to work well for negative and positive lithography techniques. In the image reversal case, the bake and exposure were followed by another bake and flood exposure to reverse the soluble parts of photo-resist. Figure 3.4 demonstrates the difference in the shape of the photo-resist in positive and negative lithography. The undercut created in negative lithography would provide the access to the underlying resist as well as the separation between the metal patches.

Another issue which should be addressed when dealing with Ohmic contacts was the thin layer of photo resist that remained in the open areas as a result of saturation of the solvents during the developing process. This thin layer could cause the contacts to degrade

and in some cases it could even cause delamination of the whole patch. A short exposure to a weak oxygen plasma could remove this layer, however it would also affect the undercut and in some cases could diminish it entirely. The power of the oxygen plasma and the duration of exposure had to be accurately calibrated in order to prevent damaging the undercut.

It has to be noted that up to this point the samples had been through multiple steps of fabrication and even before they had been exposed to the ambient for a while. Therefore, a thin layer of native oxide was formed on the InAs cap layer. This layer could degrade the quality of the Ohmic contact. For this reason, right after photolithography the samples were rinsed with a 10% solution of HCL in DI water for 30 second followed by DI water rinse for another 30 second and nitrogen blow dry. This solution is able to remove the native oxide without damaging the photo-resist. The sample were then immediately transferred to a vacuum chamber where the Ohmic contacts are deposited.

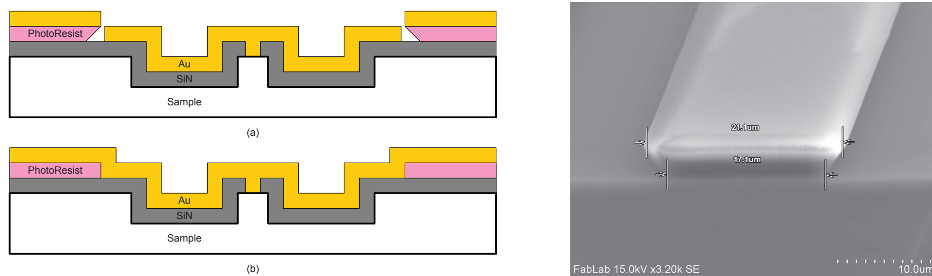

Figure 3.4: (a) Image reversal photo-lithography creating an undercut needed for lift-off (b) regular photo-lithography and SEM picture of a properly created undercut.

The deposition of the Ohmic contacts was done with an electron beam evaporator that hosted multiple target crusibles. In order to make an Ohmic contact to InAs, three metal layers composed of titanium (Ti - 30 nm), platinum (Pt -100 nm) and gold (Au - 300 nm)

were evaporated. Ti promoted the adhesion of the metal layers to the substrate, Pt served as a barrier to stop the diffusion of gold into the semiconductor region and gold functioned as the metal contact layer.

Samples were then removed from the chamber and placed in acetone for a few minutes, until metal liftoff was achieved and were then rinsed with methanol and isopropanol for 30 seconds each. Figure 3.5 shows an ICL sample after this step.

In order to achieve good heat extraction from the active region, an additional gold layer with a thickness equal or more than 3 μm was required. However, depositing such a thick layer using ebeam evaporation was not possible due to inherent inefficiency of the evaporation techniques. Accordingly, electroplating was selected as the method of choice. In this technique, current passes through a solution that contains gold with the sample serving as the cathode. Electrodeposition occurs where current flows. Since the metal paths were electrically isolated, they needed to be somehow connected to provide a single current path. The samples were, thus, placed in an electron beam deposition chamber and 150 nm of titanium was deposited on the one edge of the sample to connect all the waveguides.

Since the waveguides had to be cleaved later to produce high quality facets for the laser cavity, a thick layer of non crystalline material could potentially compromise the cleaving step. Consequently, another negative photolithography step was performed to prevent the deposition of the electroplated gold on a few lanes across the sample and perpendicular to the waveguides. The distance between these lanes were usually 1 mm allowing for cleaving laser waveguides that were multiple millimeters in length.

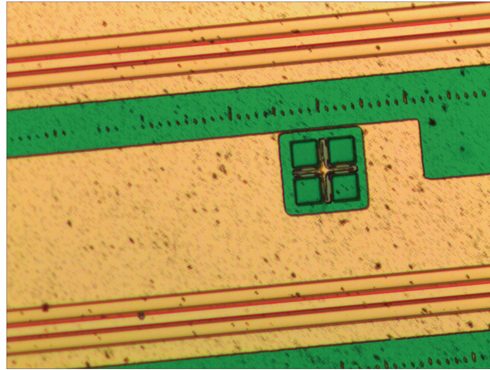

Figure 3.5: an ICL sample after top contact deposition.

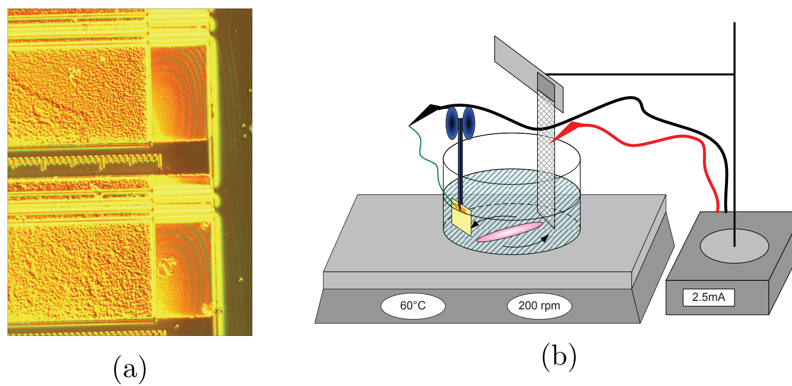

(a)

(b)

Figure 3.6: (a) an ICL sample after electrodeposition of gold (b) Electroplating Setup

In electroplating, the sample was immersed in a gold sulfite solution that was heated to 60 °C while being stirred at 200 rpm for at least 30 minutes prior to use. As shown in Fig. 3.6b, a current source was connected to the positive electrode and the sample was grounded. An electrical current of 2.5 mA was passed through the sample for about 30 minutes resulting in deposition of about 3-5 μm of gold.

Since the electroplated gold is usually rough, with the roughness depending on the

deposition rate, after electroplating and before removing the photo-resist, a thin layer of evaporated gold was deposited to smooth out the surface. Liftoff then cleared the sample of the unwanted metal. The roughness of electro-deposited gold can be visually observed in Fig. 3.6a.

Next, the samples were fixed up side down on thin microscope slides using a solvent soluble wax that melted at 150 °C . Back side of the laser samples were then polished down to 120 μm with silicon carbide (SiC) sand papers of grid 400 and 800. A polishing mount was used to control the thickness of the sample and to keep it flat on the sand paper. After polishing, samples were soaked in warm acetone until they were freed from the glass slide. They were then removed very carefully from the solvent and blow-dried extremely gently given how fragile the laser sample was at the end of the processing.

Each 1 cm $\times$ 1 cm sample included roughly about 30 waveguides which could then be cleaved to different lengths for use as laser bars or individual dies. A summery of the process flow is shown in Fig. 3.8. Figure 3.7 shows an individual laser die after dicing and cleaving as well as the ICL cleaved facet.

3.3 Mask design

The ICL devices were patterned by photolithography; therefore, photo mask design constituted one of the most important steps in the fabrication process. The laser photo-mask included four essential parts.

First was the waveguide mask. This part defined the width of the waveguides, the

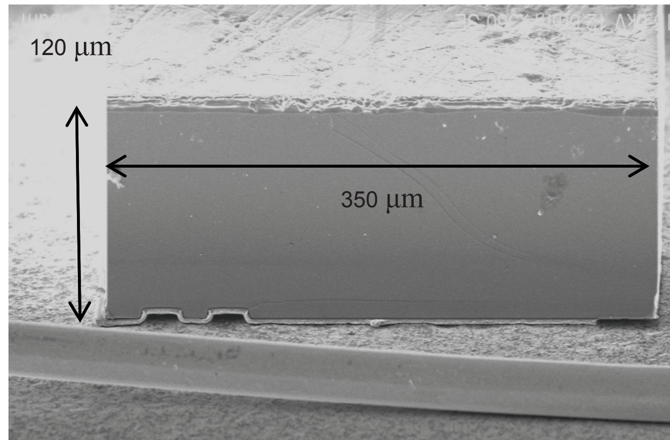

(a)

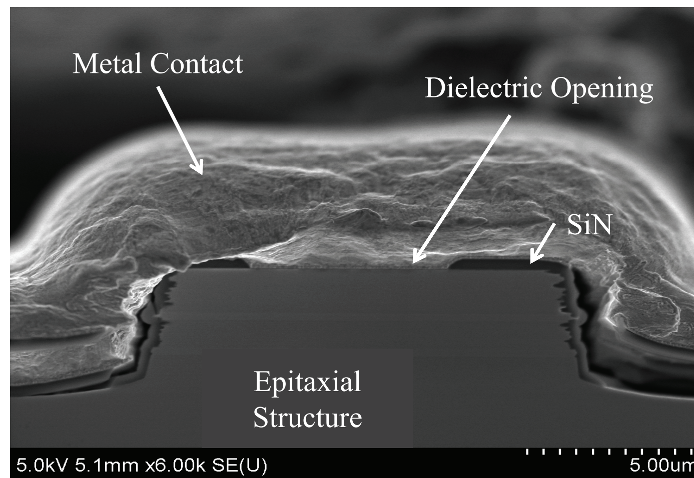

(b)

Figure 3.7: SEM picture of (a) An individual laser Die (b) an ICL cleaved facet

distance from one device to the next, the width of the trench area and the first alignment markers. The waveguide width was obtained from the mode profile simulations. In any case the goal was to achieve the specification with the maximum possible width in order to ease the fabrication process and avoid the need for ebeam lithography. Moreover, a wider width would minimize the effects of scattering losses resulting from the interaction of the mode with the sidewall roughness developed in the etching process.

When fabricating single mode devices for spectroscopic applications, simulations determined the widest possible waveguides for single-mode operation. On the other hand, when the priority was given to power generation, wider ridge lasers were desirable. In these cases, a compromise had to be made between the power generation and the heat extraction from the waveguide.

The second part of the photo-maks was the dielectric opening for patterning the dielectric layer on top of the device. As mentioned earlier, accurate alignment of this mask with the previous pattern on the sample was very important and special alignment markers were designed to facilitate this step. It should be noted that as this window defined the area of the Ohmic contact, it had an impact on the performance of the device. In order to achieve the lowest contact resistivity, the contact area should be as broad as possible. However, the angular alignment became progressively difficult as the opening gets bigger. There were alternative techniques such as self alignment that can replace photolithography and will be discussed in section 3.4.

The third mask was the one that defined the electrical isolation between each waveguide. In this mask a distance had to be considered from the metal path of each device to

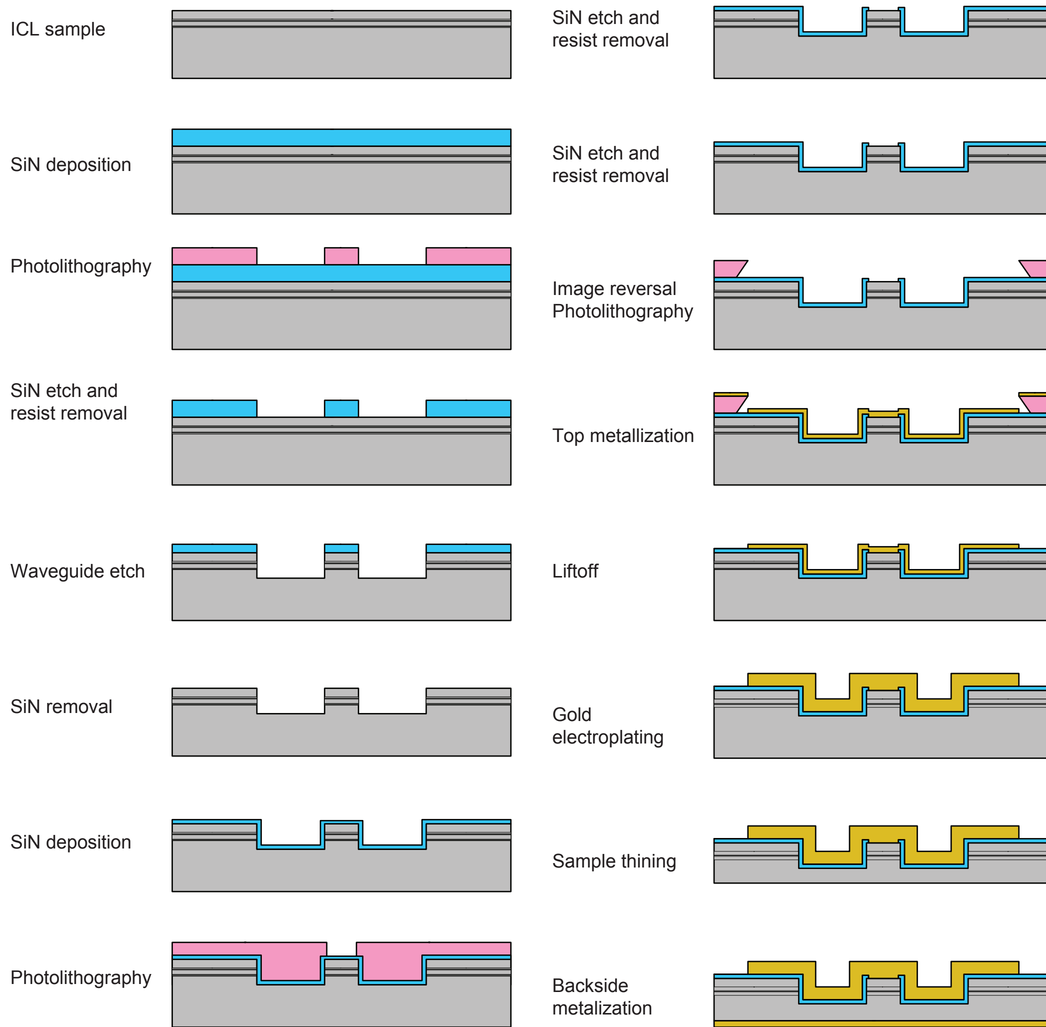

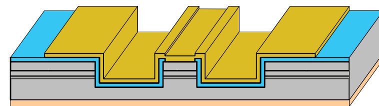

Figure 3.8: Interband Cascade Laser Process Flow

the next for electrical isolation. Moreover, the same gap would be used for dicing of individual laser dies since electroplated gold would be grown on most of the metal covered areas.

The fourth and final mask was the cleaving mask which was identical to the metal mask except for the additional cleaving lanes that had been placed in predefined distances along the waveguides. Each cleaving lane was designed to be 20 μm wide.

3.4 Self-aligned fabrication

As device miniaturization continues, the fabrication steps that require high level of accuracy become more and more challenging. For example single-mode fabrication demands narrow ridge devices with ridge widths of about a few microns, which makes the dielectric opening definition increasingly difficult. Another example is the fabrication of micro-cavity and nano-lasers where the initial structure is usually defined by electron-beam lithography. In these cases self-aligned fabrication methods are highly desirable as they simplify the fabrication process and reduce the time and cost associated with multilevel mask alignment. Planarization is a self-aligned fabrication technique that eliminates the need for critical mask alignment and provides access to the tallest parts of the structure while protecting the shallow regions.

In the case of the double trench structure, implementation of such techniques calls for selective protection of the areas outside of the trench. Masking these areas can be achieved using a metal or dielectric, provided that they have good selectivity over SiN.

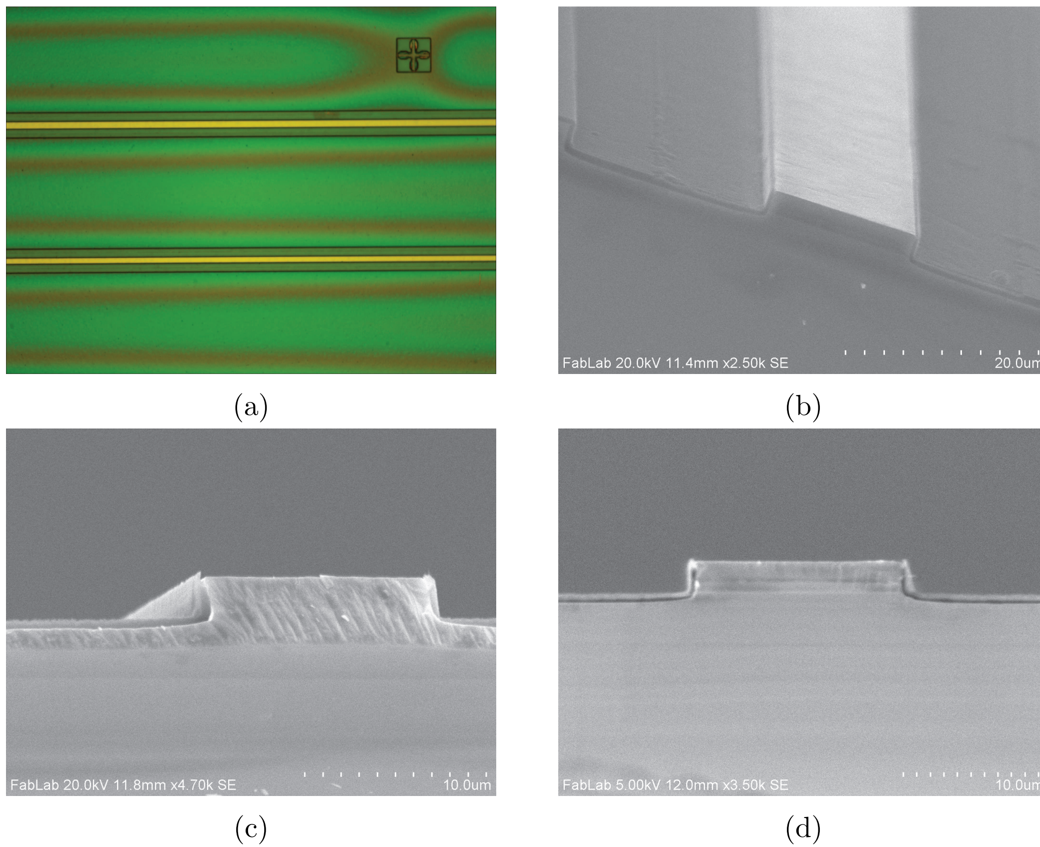

Figure 3.9: Planarization results for double trench waveguides. (a) an optical microscope picture of a planarized and etched sample. (b-d) SEM pictures of the cross section of the diced sample from different angles.

In order to implement the planarization technique, new masks were designed to define and protect the areas outside the trench. A Futurrex planarization polymer (PC3-1500) was employed in combination with SiO_2. This polymer was spun on the sample at 2000 rpm for 2 min and baked at 180°C for 5 min. The baked polymer then was flood etched to reveal the top of the waveguide as shown in Fig. 3.9a. The processed samples shown in these pictures have been diced to enable the SEM imaging of the sample cross section. Etching recipe was developed to etch the polymer an SiN on top of the waveguide in 10 min in order to avoid exposing the side wall's dielectric and shorting the final device. This recipe used the CF_4/O_2 combination and is summarized below

Plasma: RF power:100 W; ICP power: 150 W,
Gas combination: CF_4: 20 sccm; O_2: 5 sccm.

Figure 3.9 shows the result of planarization recipe that was applied to the double trench waveguide. This technique allows for preservation of SiN on the sidewalls as is apparent from Fig. 3.9b and 3.9b

3.5 Sample Packaging

Sample packaging is required for applications where reliable mechanical and thermal performance are required. There individual laser dies were bonded either epi-side up or epi-side down to an AlN sub-mount using a die bonder as shown in Fig. 3.10a. In epi-side down mounting the laser waveguide was immersed into the solder for efficient heat extraction as shown in Fig. 3.10b. For optimal thermal performance epi-down mounting was chosen for ICL packaging [44].

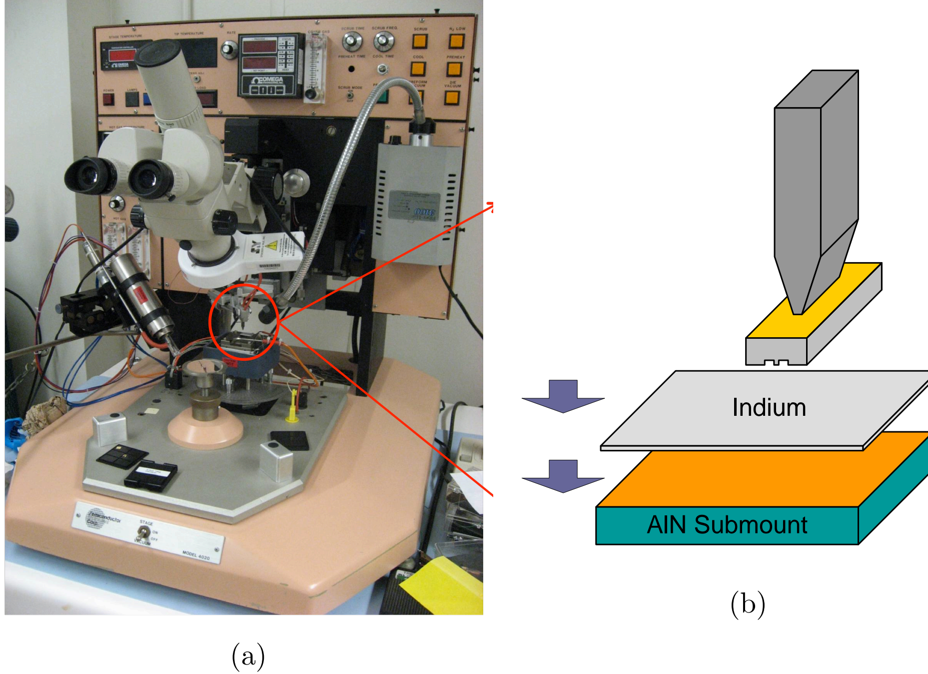

(a)

(b)

Figure 3.10: (a) Laser die bonder (b) Die attach process

The packaging began with thermal evaporation of 3 μm of indium on 3 mm $\times$ 5 mm $\times$ 2 mm aluminum nitride (AlN) sub-mounts. The sub-mounts were kept under vacuum to avoid the oxidation of indium until they were ready to be used. The reason behind the choice of indium for soldering was two fold. First, indium melts at a relatively low temperature that seems to not cause any degradation to the device performance. Second since it is a soft solder, it also compensated for the thermal expansion mismatch between the laser and the mount. This is contrast to gold-tin eutectic solders used for commercial laser packaging.

For epi-down mounting, the thickness of indium should exceed the ridge waveguide

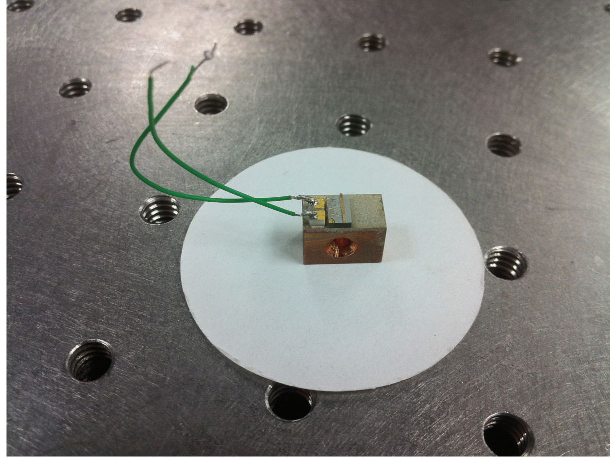

Figure 3.11: A packaged 5 mm interband cascade laser diode.

etch depth. A touch of indium flux prepared the sub-mount surface for the contact. The submount was then placed securely on the bonder heating element and was progressively heated up to 160 °C (indium melting temperature). Meanwhile, using the bonder vacuum tip, the laser die was carried to the sub-mount. The vacuum tip also heated to avoid temperature drop upon contact with the solder. When indium was melted, the vacuum tip places the sample on the edge of the sub-mound and presses into the indium. The sub-mount was then removed from the heater to minimize the heat exposure.

The sub-mounts are subsequently mounted on small blocks machined from copper using H20E silver epoxy and cured at 150 °C for 10 minutes. Electrical connections were created by wire bonding which completed the packaging process. Figure 3.11 shows a finished 5 mm packaged device.

Chapter 4

Towards Room Temperature Operation of ICLs

4.1 Introduction

This chapter focuses on the characterization of ICL devices. First, the measurement setup and methodology are reviewed. Several design variants are characterized and design modifications for improving the ICL performance to achieve RT CW operation are compared. The discussion then concentrates on the different aspects of device performance and unique considerations required for the packaging. Finally, the temperature dependence of device properties are measured and their implications are discussed.

4.2 Characterization Methodology

In a laser diode the relationship between the optical power and the drive current follows [58],

$$P_o = F_f \eta_i N \frac{\alpha_m}{\alpha_m + \alpha_i} \frac{h\nu}{q} (I - I_{th}), \tag{4.1}$$

where I_{th} is the threshold current, α_i is the internal loss, η_i is the internal quantum efficiency, N is the number of cascaded active regions, q is the electron charge, h is the Planck's constant, and ν is the emission frequency. The mirror loss α_m is defined as [58]

$$\alpha_m = \frac{1}{2L} \ln \frac{1}{R_f R_b}, \tag{4.2}$$

where L is the length of the laser cavity and R_f and R_b are the power reflection coefficients from the front and back facets, respectively. Since light is collected only from one facet the factor F_f is needed to calculate the fraction of light coming out of the front facet [58]:

$$F_f = \frac{(1 - R_f)}{(1 - R_f) + \sqrt{\frac{R_f}{R_b}}(1 - R_f)}. \tag{4.3}$$

The term $F_f N \eta_i \frac{h\nu}{q} \alpha_m / (\alpha_m + \alpha_i)$ is usually referred to as the differential efficiency and is denoted by η_d. It is apparent that $1/\eta_d$ varies linearly with the cavity length [58],

$$\frac{1}{\eta_d} = \frac{h\nu}{q} \frac{1}{\eta_i} (1 - \alpha_i \frac{2L}{\ln[R_f R_b]}). \tag{4.4}$$

Therefore, given I_{th} and η_d for several cavity lengths, η_i and α_i may be extracted by linear interpolation. It should be noted that this method is based on the assumption that η_i and α_i do not depend on L. While this is a good approximation for α_i, it may not always hold

for the internal efficiency since shorter cavities with higher threshold carrier concentrations may have lower internal efficiencies. By assuming a linear gain near the threshold, *i.e.*

$$g_{th} = \left(\frac{dg}{dJ} \bigg|_{J=J_t} \right) (J_{th} - J_t), \tag{4.5}$$

where dg/dJ is the differential gain per unit current density, and J_t is the transparency current density, and employing the gain condition for the lasing at threshold,

$$\Gamma g_{th} = \alpha_i + \alpha_m, \tag{4.6}$$

yeilds the threshold current density as

$$J_{th} = J_t + \frac{\alpha_i}{\Gamma \frac{dg}{dJ}} - \frac{\ln[R_f R_b]}{2L\Gamma \frac{dg}{dJ}} \tag{4.7}$$

where Eq. 4.2 is used to evaluate α_m.

As can be seen in Eq. 4.7, J_{th} and L^{-1} also have a linear relationship that can be deduced through a cavity length analysis by measuring several un-coated devices, $R_f = R_b = R$, with different lengths. It has been shown that $J_t \Gamma dg/dJ$ is small compared to α_i in ICLs [3] and therefore the first term in Eq. 4.7 is negligible relative to the second term. Thus, the ratio of the intercept to the slope of the J_{th} versus L^{-1} relation multiplied by $\ln(1/R)$ gives the value of α_i.

Extraction of the internal loss from threshold current density is less sensitive to temperature variations and provides a more reliable method compared to that of the slope efficiency. Besides, measurements of the threshold current density is often acheived with

much higher accuracy than the slope efficiency, especially in cases where the thermal roll off is significant.

In addition to the internal loss, $\Gamma dg/dJ$ at threshold can be obtained from a linear fit to the J_{th} versus $1/L$ data. The 2D carrier density n can be calculated from the current density via

$$n = \frac{q}{\eta_i \tau} J \tag{4.8}$$

where τ is the carrier lifetime.

Temperature dependent measurements of J_{th} and η_d are also performed to obtain the characteristic temperatures T_0, and T_1 from

$$J_{th}(T') = J_{th}(T) \exp(\frac{\Delta T}{T_0}) \tag{4.9}$$

and

$$\eta_d(T') = \eta_d(T) \exp(\frac{-\Delta T}{T_1}), \tag{4.10}$$

respectively [58].

All the aforementioned parameters should be extracted in the pulsed mode, since it allows for measurement of the internal parameters of a laser diode without any complication introduced by thermal effects. Verifications such as the consistency of slope and threshold current density upon slight increase in the duty cycle should be employed to confirm that sufficiently short pulses have been used. This methodology allows for the extraction of internal loss, internal efficiency, modal gain per unit current density, and characteristic temperatures T_0 and T_1 from the pulsed light-current measurement.

4.3 Laser Test Setup

Fabricated samples were measured in the form of a laser bar or an individual die, in continuous wave (CW) or pulsed operation modes. For pulsed characterization, the laser samples were placed on a flat copper block and were probed from the top as shown in Fig. 4.1. The devices under measurement were forward biased by an Avtech voltage pulse generator at a frequency of 1 kHz and duty cycle of 0.05%. A Stanford Boxcar integrator triggered by the function generator sampled the voltages V_1 and V_2, as identified in Fig. 4.2, over a 200 ns sampling window. This window was positioned in the middle of the 500 ns pulse. A Judson lead-selenide (PbSn) detector was put directly in front of the laser to measure the output light. The detector output was fed into a lock-in amplifier which was also triggered with the voltages generator. As the voltage was increased the sampled voltages V_1 and V_2 and the lock-in amplifier output were sent to a computer and voltage-current and light-current characteristics were measured in real time.

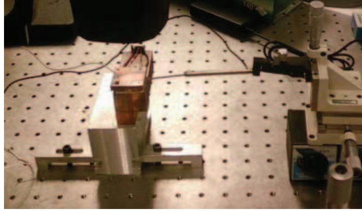

Figure 4.1: Laser bar probe station

The advantage of this method is that many samples of the same length can be measured successively to improves the accuracy of interpolations. Thus, overall characterization of material and device properties were done with this method. However, since the samples were loosely placed on the copper block, the thermal conduction was poor and cooling could not be done effectively. Therefore, this configuration was only suitable for pulsed

measurements.

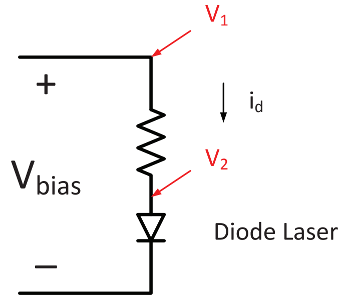

Figure 4.2: Biasing circuit.

For CW measurements, an ILX Lightwave laser diode driver was used to drive the device and the voltage was measured directly across the the laser die. Packaged lasers, as discussed in section 3.5 were used for CW or temperature-dependent measurements to ensure good control over the measured electrical and thermal parameters. Packaged devices were fixed on a thermoelectric-cooled copper holder. The copper holder was designed such that water can circulate within to accelerate the cooling process. A thermoelectric cooler was installed on the copper holder and mounted devices are attached to the cold plate. In order to enable the characterization of laser diodes below the dew point [15 °C], all the electrical connections, as well as the connections to the Peltier cooler, were vacuum sealed and enclosed by an aluminum cap with a glass window, as shown in Fig. 4.3. A vacuum pump was used to draw the air and moisture from the enclosure to prevent water condensation on the laser facet at temperatures below 15 °C . This arrangement also reduced the convectional losses to allow for better thermal isolation of the device.

The experimental setup for wavelength measurement included a Spex 500M monochro-

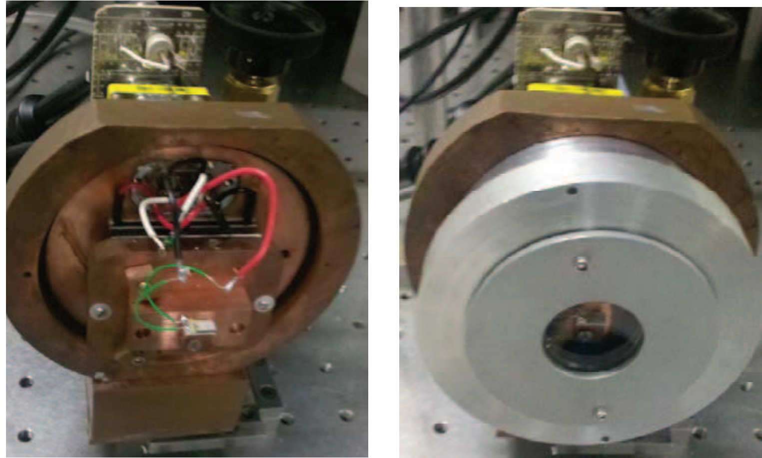

Figure 4.3: The Copper Holder of the ICL characterization setup.

mator with modified grating for mid-infrared as well as a visible laser (HeNe in this case). The setup schematic is shown in Fig. 4.4. A Lightpath aspheric collimating lens with short focal distance of 4 mm was used to collimate the ICL output. The visible laser was used to trace the mid-IR beam and was only turned on during the alignment of the optics.

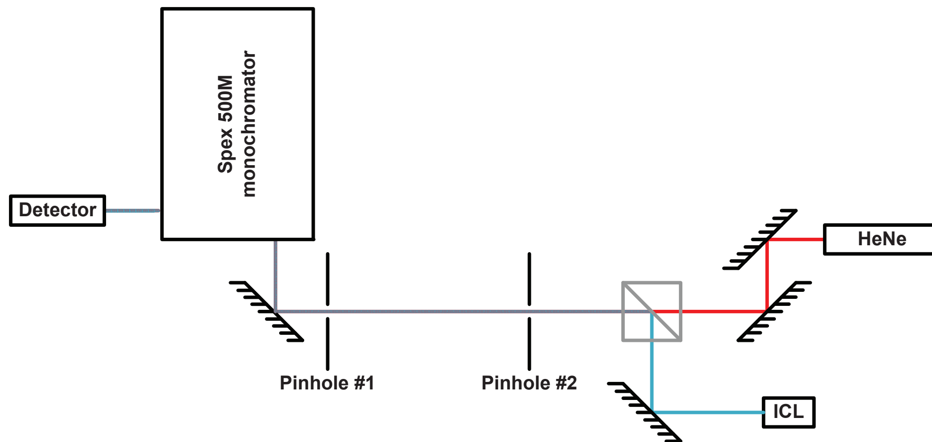

Figure 4.4: ICL wavelength measurement setup.

4.4 Interband Cascade Laser Characterization

In order to achieve high power CW operation, numerous ICL samples were grown and tested, each providing new clues for further progress. The experimental data analysis together with the theoretical simulations resulted in advancements in every generation of ICLs. Some of the grown and fabricated samples and their characteristics are reported in this section.

The number of cascaded active regions, the doping level of the active region, and the length of the electron injector were varied among samples to investigate their impact on the device performance. In this study, the performance of the 12- , 6- and 5-cascade devices are reported. Although more cascades provide more gain, low-cascade-number ICLs are thermally more advantageous due to the low thermal conductance of the GaSb substrate. This leads to a trade off between achieving the highest power and the operating temperature. In order to avoid high internal loss due to the inter-valence absorption in p-doped materials [3] the SCH in these devices were n-doped where tellurium was used as the dopant.

ICL wafers were grown by molecular beam epitaxy (MBE) on a GaSb (001) substrate and fabricated using the techniques explained in chapter 3. Laser samples have been fabricated at the Nano-center at the University of Maryland. The processed samples were first cleaved into laser bars and then characterized using the low duty cycle pulsed measurement technique explained earlier. These characterizations were done in the Laboratory for Green Nano-photonics, Optoelectronics and Nano-sensing at the University of Maryland. The measurements were subsequently analyzed to extract various device parameters such as internal loss, internal efficiency, threshold current density, characteristic temperature and differential efficiency using the method explained in section 4.2. The threshold current

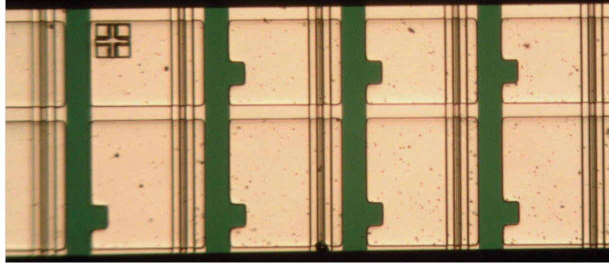

Figure 4.5: 0.5 mm Interband cascade laser bar

for each device was obtained by fitting a straight line to the light-current (LI) curve at values above threshold. The extracted threshold currents for different lengths were then gathered from multiple devices for further analysis.

The fabricated ICLs were also measured in continuous wave mode. Early generations of the devices could sustain CW operation only below ambient temperature, the highest of which was for the 6-cascade laser at 15 °C [3]. Once optimized, the 5-cascade lasers reached CW operation above the ambient temperature with the output power in the order of tens of milli-Watts and WPEs of about 6%.

4.5 Results and Discussions

Multiple lengths of the 12-cascade active region ICL were measured in the pulsed mode at room temperature. The current-voltage (IV) and light-current (LI) characteristics for a typical 1 mm, 2 mm and 3 mm devices are shown in Fig. 4.6. All of these devices were 8 μm wide, differing only in the cavity length. The threshold current for the ICLs in Fig. 4.6a is 183 mA, 268 mA, and 323 mA for the 1 mm-, 2 mm-, and 3 mm-long devices, respectively. The threshold current density was obtained by dividing the threshold current

by the device dimensions. The extracted internal loss for 12-cascade ICL from the length dependent threshold current density analysis, illustrated in Fig. 4.6b, was 8 cm^{-1} and the extrapolated threshold current density at infinite length was 953.2 A/cm^2.

Next, the number of cascades in the aforementioned structure was reduced from 12 to 6. Characterization of these devices revealed an internal loss of 7 cm^{-1}. These results showed that the effect of the number of cascades on the internal loss mostly comes from the relative extent of the optical in the active and SCH regions as reflected in the device confinement factor. [3, 59].

The next ICL design was a 6-cascade device where the p-doping of GaInSb and the GaSb wells in the active region were lowered. The objective of the new design was to assess the contribution of the absorption in these p-doped regions to the laser internal loss [3]. Pulsed mode measurements of fabricated ICL devices of various lengths were performed at room temperature. The LI and IV curves for 1 mm, 2 mm and 3 mm devices are plotted in Fig. 4.7a. The width of these devices was 10 μm and their lengths varies. The threshold current for the displayed devices were 237 mA for 1 mm, 342 mA for 2 mm and 427 mA for 3 mm long lasers. The internal loss obtained from the analysis of the threshold current density versus length was 4.8 cm^{-1} for this structure as shown in Fig. 4.7b [3]. These results show that the 6-cascade device is similar to the 12-cascade in terms of the threshold current density but exhibits a much lower loss. The fewer number of cascades as well as lower p-type doping in the active region are believed to be the reason behind the loss reduction. The lower internal loss is a key merit in the ICL performace as it plays an important role in achieving a high temperature operation for these lasers.

To investigate the effect of the length of electron injector on the device performance a

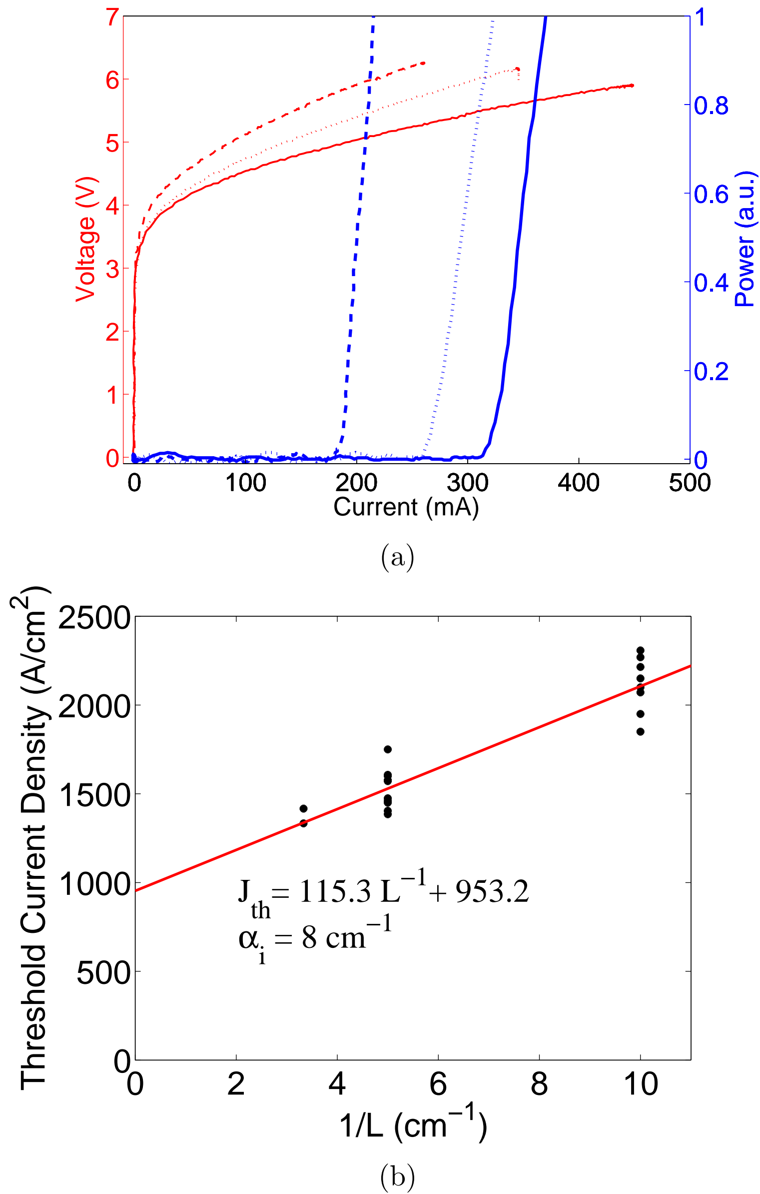

Figure 4.6: (a) IVL curve for 12-cascade ICL for cavity length 0.6 mm (solid line) 1 mm (dashed line) 2 mm (dotted line) (b) Threshold current density versus 1/cavity length

5-cascade ICL wafer was grown with the electron injector length reduced from 53 to 25 nm. IV and LI characteristics of the fabricated devices for 4 different cavity lengths are shown

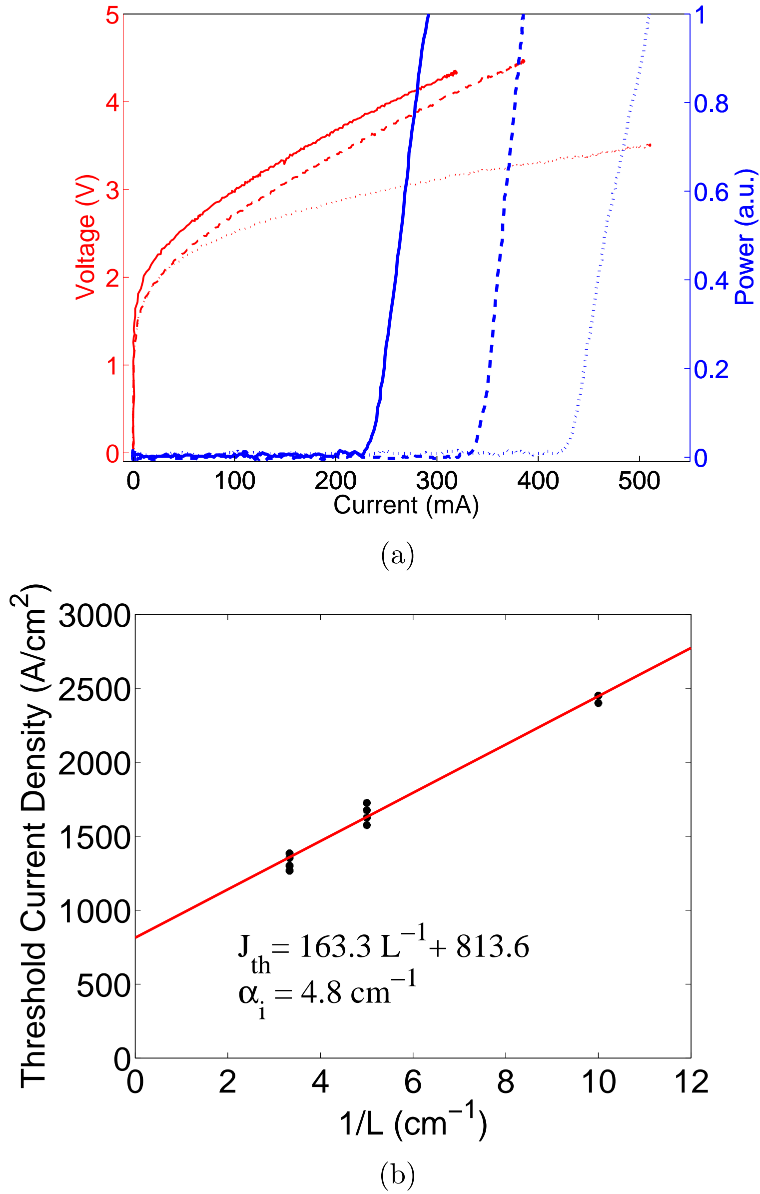

Figure 4.7: (a) IVL curve for 6 cascade ICL for cavity length 1 mm (solid line) 2 mm (dashed line) 3 mm (dotted line) (b) Threshold current density versus 1/cavity length [3]

in Fig. 4.8a. The threshold current for 1 mm, 2 mm, 3 mm and 5 mm devices shown in Fig. 4.8a are 67 mA, 85 mA, 110 mA and 193 mA, respectively. These devices lased at

appreciably lower threshold current density. The lower threshold was attributed to the lower length of the electron injector. This low threshold current density is essential for high temperature, high power CW operation. The threshold current density curve versus inverse length, Fig 4.8b, revealed internal loss of 4.9 cm^{-1} for these devices, similar to their 6-cascade counterparts [3]. It further shows that the main contribution to the internal loss comes from the doping types and levels as well as the extent of the mode penetration into the low and high loss layers. The values of internal loss around 5 cm^{-1} are the lowest reported values for ICLs.

Figure 4.9 shows the emission spectrum of a 3 mm-long 5-stage ICL operated in pulsed mode at room temperature above threshold as measured using the setup explained in section 4.2. The spectrum has a dominant peak at 3.8 μm at RT in pulsed mode operation.

Another 5-cascade ICL design was optimized and tuned for RT emission at 3.5 μm. The wavelength was altered by adjusting the thickness of InAs active e-wells. Moreover, in order to improve the performance of the prior design, additional doping was applied to the electron injection region [2]. ICL devices were subsequently fabricated and characterized. Figure. 4.10a shows the IV and LI characteristics of these lasers for several lengths. This design demonstrated the lowest threshold current density amongst all of the fabricated devices. The 1 mm, 2 mm and 3 mm devices lased at 55 mA, 85 mA and 115 mA, respectively. Figure 4.10b shows the threshold current density versus inverse cavity length from which an internal loss of 5.8 cm^{-1} can be extracted.

The δ-strained active region with an additional hole well and InAs barrier, which is explained in section 2.4, was also fabricated and characterized. This device did not perform

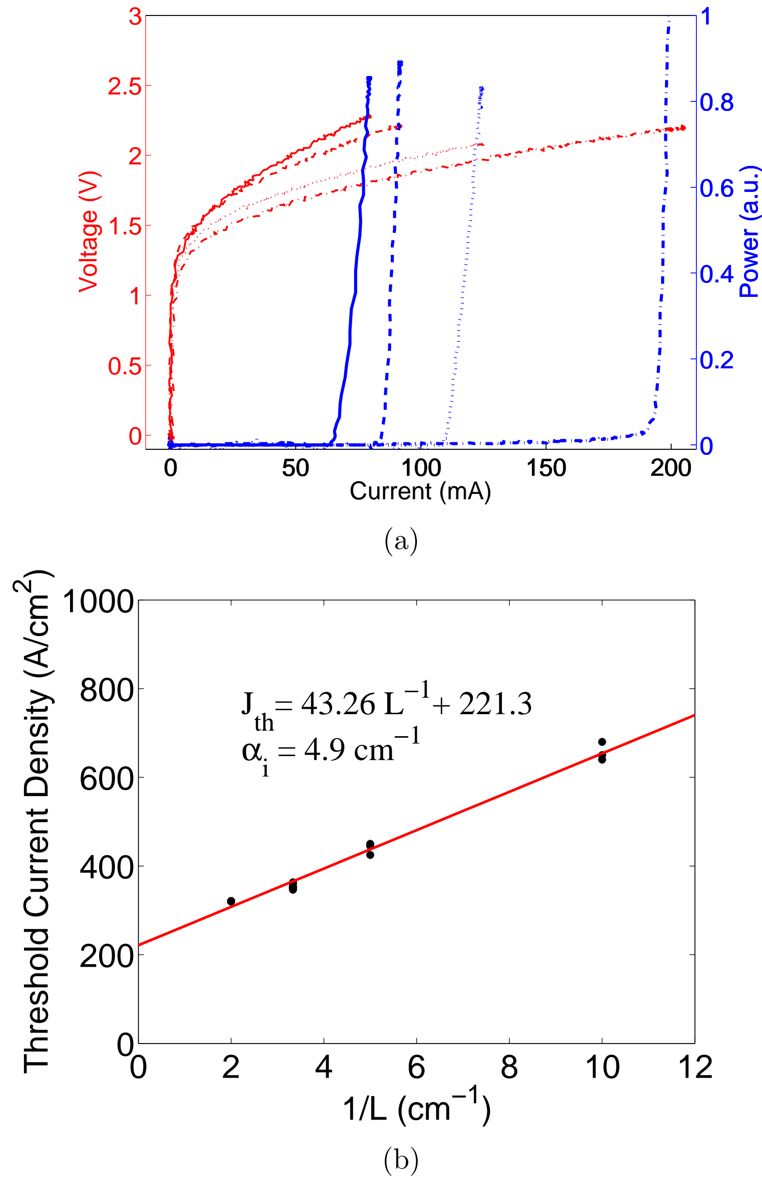

Figure 4.8: (a) IVL curve for 5-cascade ICL for cavity length 1 mm (solid line) 2 mm (dashed line) 3 mm (dotted line) and 5 mm (dotted-dashed line) (b) Threshold current density versus 1/cavity length [3]

as well as the five stage W-shaped active region and it requires further optimization to reach a competitive performance. The LI and IV characteristics for several lengths of this

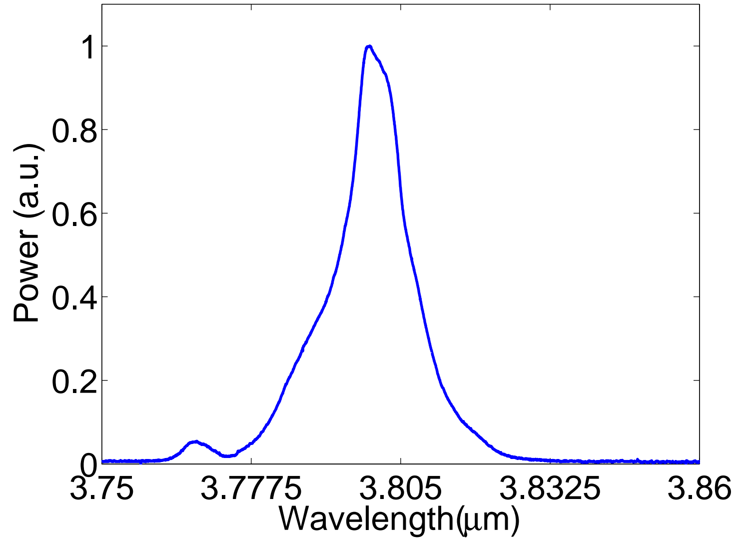

Figure 4.9: Normalized intensity vs. emission wavelength for the 5-cascade ICL at 3.8 μm.

design are shown is Fig. 4.11a. The threshold current is 236 mA for 1 mm device, 306 mA for 2 mm device, 432 mA for 3 mm device and 663 mA for 5 mm device. Figure 4.11b shows the length dependence of the threshold current density. The internal loss of 6.4 cm^{-1} was extracted from a linear fit to these values.

In order to better understand the underlying reason for the lower performance of the δ-strained ICLs, the emission spectrum above threshold was measured in the pulsed mode at RT for a 2 mm-long laser die. The result is shown in Fig. 4.12. The two peaks in the emission wavelength at 3.38 μm and 3.41 μm probably originate from the two transitions in the active region. The presence of multiple transitions results in splitting of the carriers between the available energy states and degrades the laser performance. It might be possible to eliminate the extra transition by optimizing the QW structure.

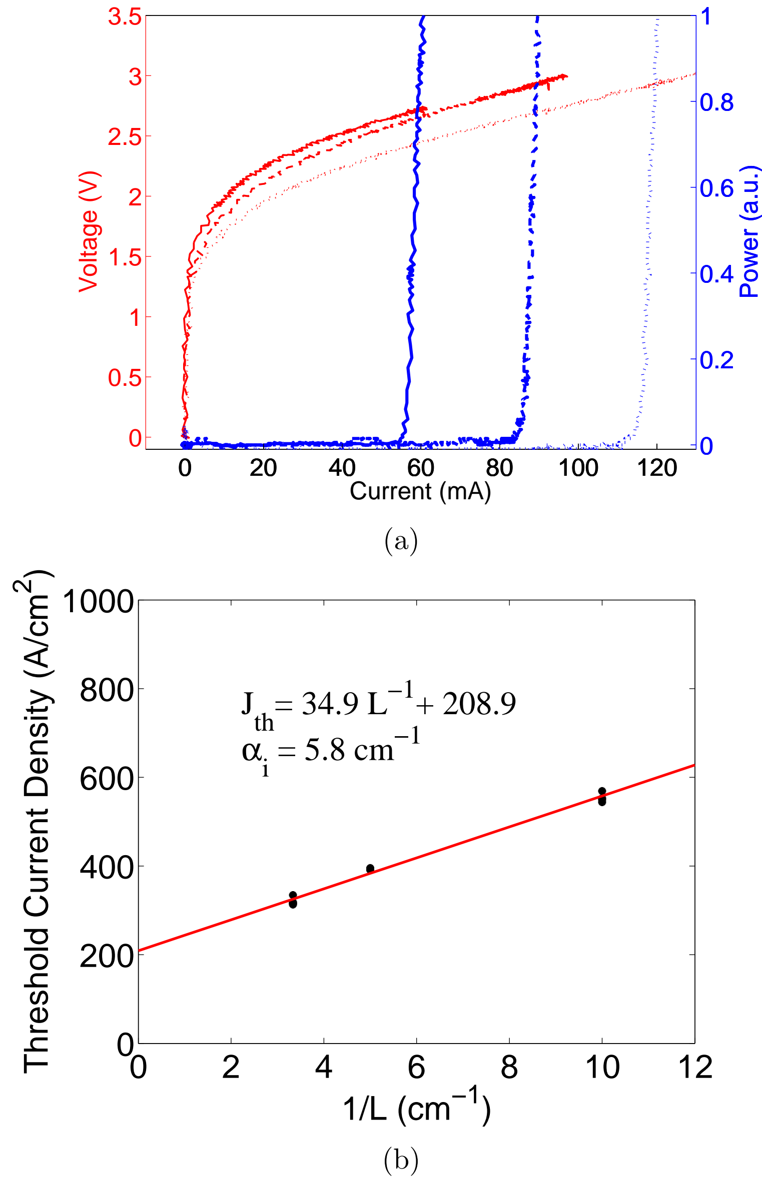

Figure 4.10: (a) IVL curve for 5-cascade ICL for cavity length 1 mm (solid line) 2 mm (dashed line) 3 mm (dotted line)) (b) Threshold current density versus 1/cavity length

Both of the five cascade W-shaped active region ICLs reached CW operation at room temperature. The CW IVL plot for a 3 mm 5-cascade device at 3.8 μm is shown in

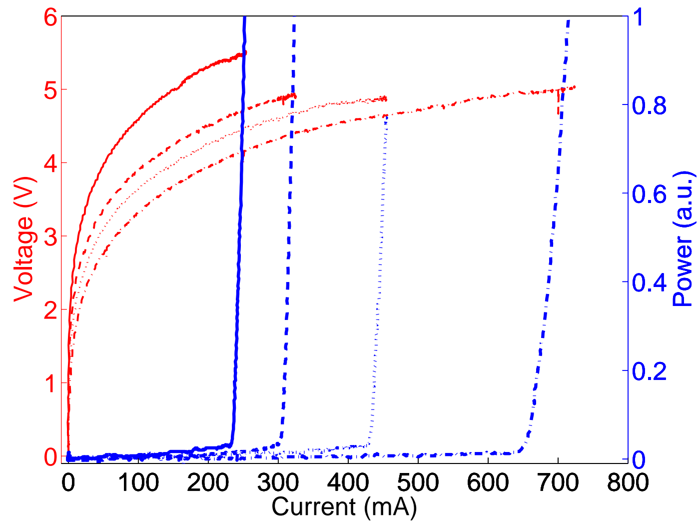

(a)

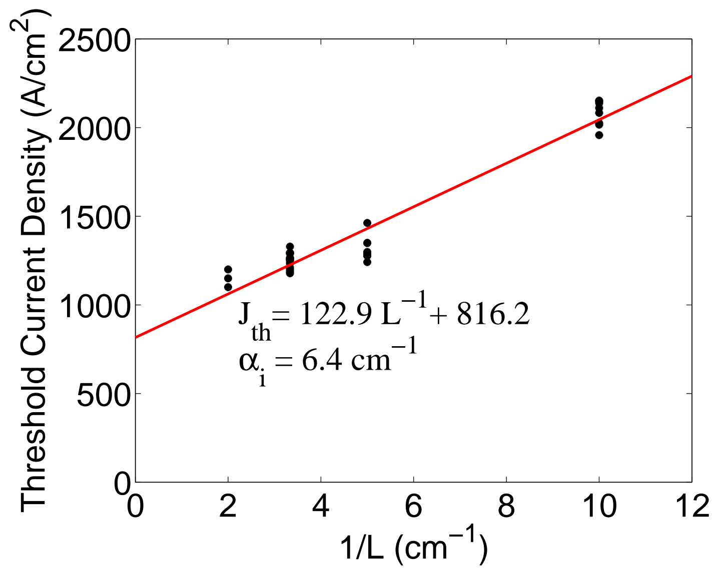

(b)

Figure 4.11: (a) IVL curve for δ-strained 5-cascade ICL for cavity length 1 mm (solid line) 2 mm (dashed line) 3 mm (dotted line) and 5 mm (dotted-dashed line) (b) Threshold current density versus 1/cavity length

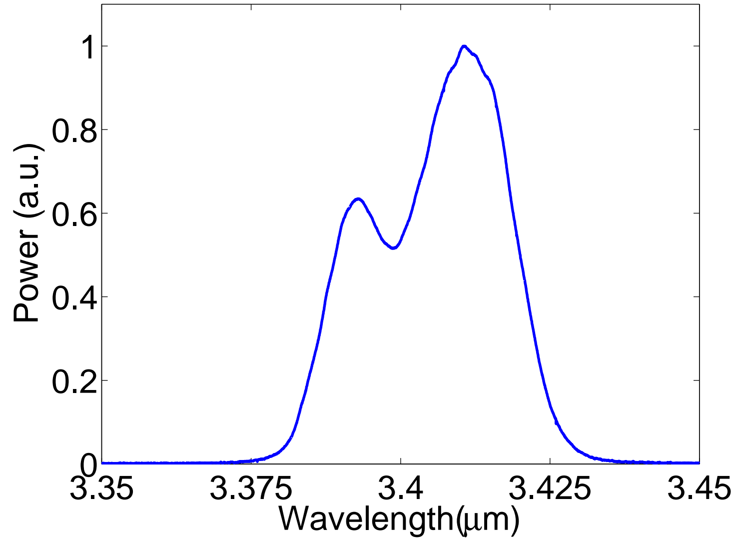

Figure 4.12: Intensity vs. emission wavelength for the δ-strained ICL

Fig. 4.13. This device reached a maximum emission power of 23 mW at the injection current of 630 mA. Also plotted in these figures is the IVLs for HR-coated back facet and un-coated front facet (HR/U). HR coating combination of ($Ta_2O_5/SiO_2/$ $Al/Ta_2O_5/SiO_2$) was evaporated on the back facet of the laser with thickness composition of 5/25/150/5/45 nm, respectively. Subsequently, the light output from the front facet increased to 28 mW at 640 mA. The threshold current of the original un-coated device was 167 mA which decreased to 154 mA after HR coating.

Anti-reflection coating of the front facet of this device resulted in higher output power of 40 mW at room temperature [48].

The highest CW RT power was obtained from a 5 mm long 5-cascade ICL at 3.8 μm, with the IVL characteristic shown in Fig. 4.14. The original 5 mm device lased at 199 mA and reached the maximum output power of 36 mW at 990 mA. HR coating combination identical to the one used for the 3 mm die was applied and reduced the threshold current

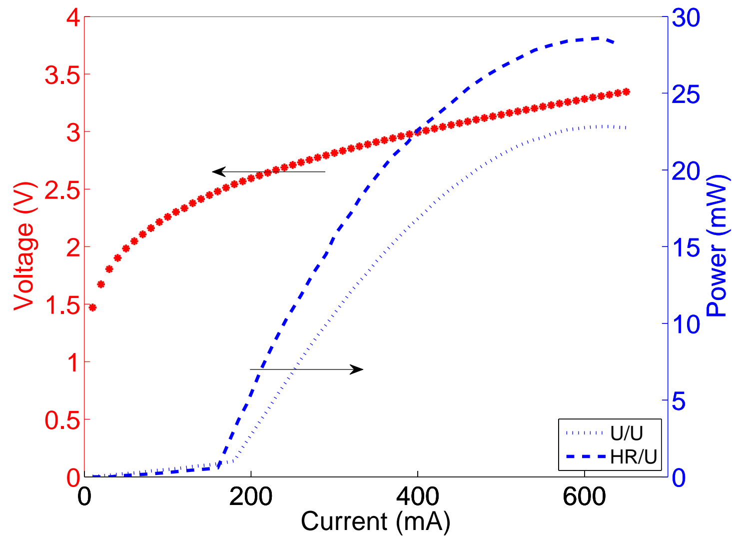

Figure 4.13: CW IVL for a 3 mm long 5-cascade ICL at 3.8 μm

to 173 mA and increased the output power from the front facet to 39.9 mW at 1100 mA. Maximum CW RT power of 62 mW was attained after AR coating of the front laser facet [48].

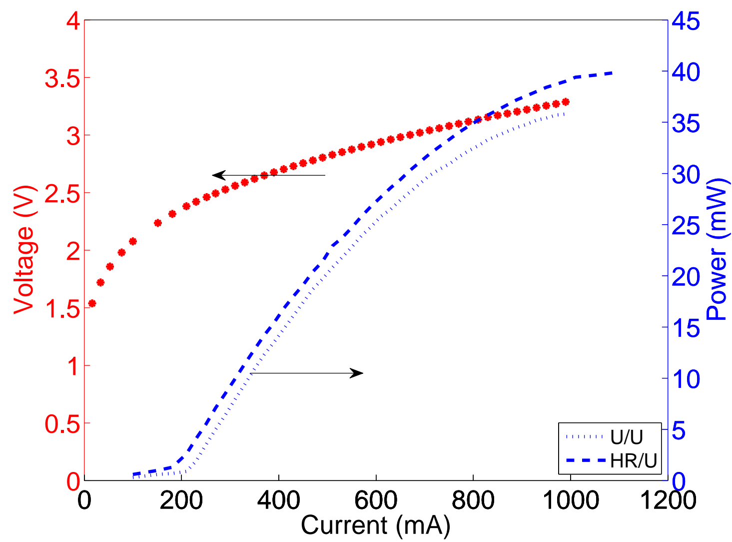

Figure 4.14: (a) CW IVL for a 5 mm long 5-cascade ICL at 3.8 μm

Table 4.1: Summary of experimental results of various active region optimizations

Number of Cascades	**Active Region Desgin Change**	α_i**[cm]**	J_{th}**[A/cm²] (L=3 mm)**	**CW RT**
12	–	8	1350	×
6	Lower number of cascades	7	1317	×
6	Lower p doping in the GaInSb and GaSb QWs	4.8	1300	×
5	Lower length of the electron injector	4.9	365	✓
5	Higher n doping in the electron injector	5.8	325	✓
5	δ-strained active region	6.4	1200	×

The maximum WPE from an un-coated laser die was achieved for the 5-cascade ICL at 3.5 μm. Figure 4.15a shows the IVL curve for a 1 mm-long ICL. This device lased at 80 mA with the maximum power of 20.3 mW reached at 250 mA. This output power was closed to maximum output power for the 3 mm device from the 5-cascade ICL at 3.8 μm. The WPE reached the value of 5.9% at 170 mA, Fig. 4.15b. This value equals the QCL WPEs in 3-4 μm range and compares with the highest values achieved for ICLs. The experimental results obtained from different ICL designs are summarized in Table 4.1.

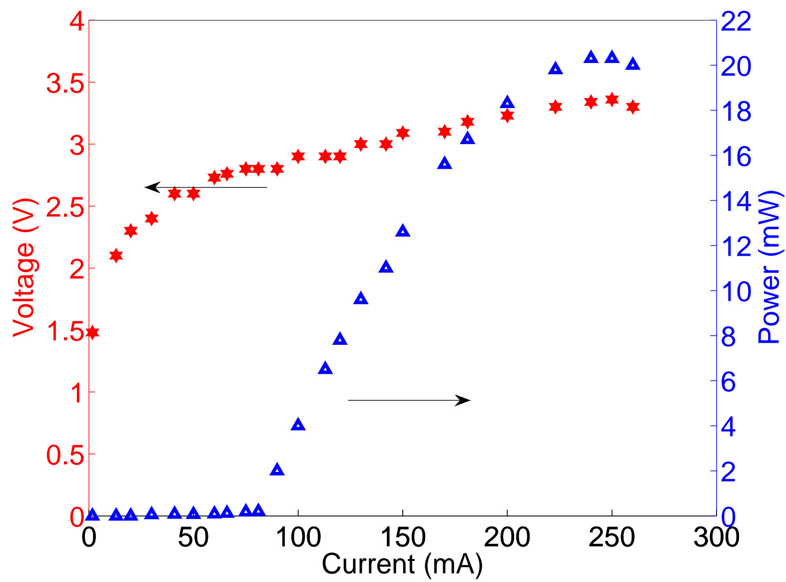

(a)

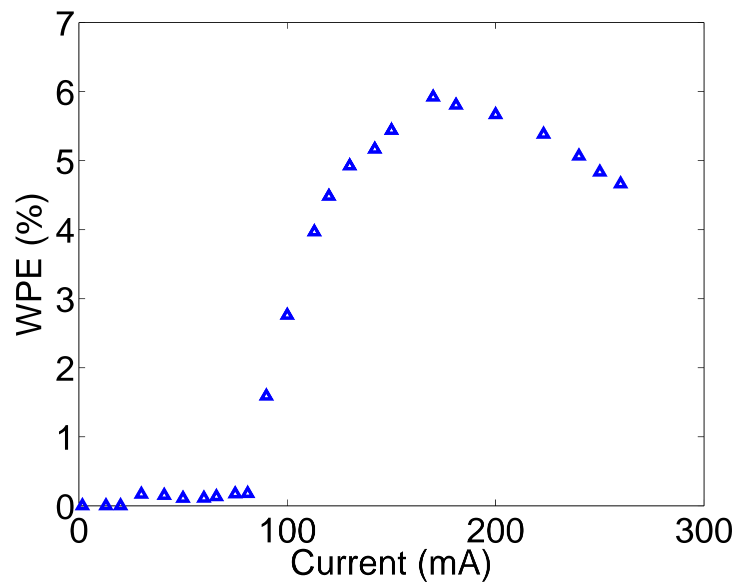

(b)

Figure 4.15: (a) CW IVL for a 1 mm long 5-cascade ICL at 3.5 μm(b) WPE for a 1 mm long 5-cascade ICL at 3.5 μm

4.6 Series Resistance

Large series resistance in a laser diode creates thermal heating and degrades the device performance at high powers and temperatures. Therefore, in the path to achieve less temperature sensitive device operation, this parameter should be minimized. Although most of the series resistance originates from the epitaxial layers, optimizing the contact can also contribute to a lower resistance. Differential series resistance is calculated from the liner fit to the the IV curve at values above threshold and is found to be around 2 Ω for a 2 mm ICL.

4.6.1 Contact Resistance

The two factors determining the values of contact resistance are the contact area and contact sheet resistance. Both of these elements were studied for a typical ICL laser die. Since the cap layer in all the ICL materials is the same, 200 Å of InAs with doping levels of $\sim 10^{18}$ cm^{-3}, the choice of the specific laser material does not affect the result.

The sheet resistance for a metal-semiconductor contact was measured using the Circular Transmission Line Method (CTLM). δ-strained ICL samples were patterned with CTLM structure shown in Fig. 4.16. After the usual HCL treatment, the Ti/Pt/Au stack used in the ICL contact recipe, i.e. (30 nm/100 nm/150 nm), was patterned by standard lithography and liftoff. The contact resistance was subsequently measured by four point probe measurement technique to minimize the effects of the finite resistance of the probes and wires. After measuring the resistance between the gold pad and each of the inner circles, the resistance was plotted versus $\ln(R/r)$, where $R = d + r$ and r is the radius of the inner circle and is equal to 200 μm. d is the difference between the inner and outer

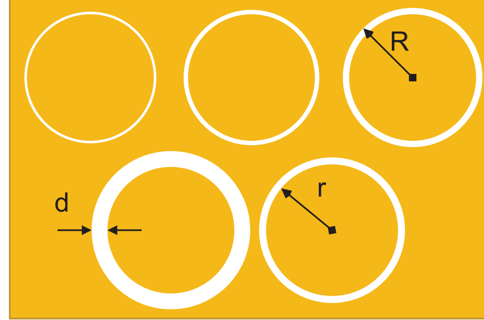

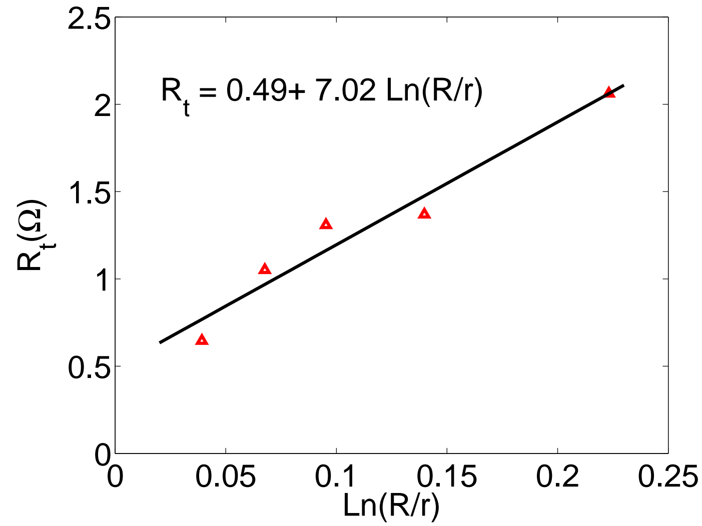

Figure 4.16: CTLM Pattern for r = 200 μm and d=8, 14, 20, 30, 50 μm(left). Measured contact resistance (right).

circles diameter, which equals to 8, 14, 20, 30, 50 μm. The sheet resistance R_{sh} and the contact resistance ρ_c then relate to the slope and Y-intercept of the linear interpolation as

$$\text{Slope} = \frac{R_{sh}}{2\pi} \tag{4.11}$$

$$Y_{\text{intercept}} = \frac{R_{sh}L_t}{r\pi}, \tag{4.12}$$

where L_t is transfer length and is defined as $L_t^2 = \rho_c/R_{sh}$. The resistance values of

$$R_{sh} = 44.10 \qquad \Omega/\square, \tag{4.13}$$

$$\rho_c = 2.16 \times 10^{-5} \quad \Omega.\text{cm}^2. \tag{4.14}$$

were extracted for this specific Ohmic contact. Sheet resistance translates to resistance through $R = R_{sh}W/L$, where W and L are the contact width and length. This means that for a 10 μm ridge laser with 1 mm length the resistance should be 0.216 Ω, which is negligible compared to the overall ICL contact resistance of 1-2 Ω.

Another factor determining the contact resistance is the contact area. The current flowing in the cap layer in the lateral direction experiences nearly two orders of magnitude higher resistance compared to the current flowing in the growth direction. Consequently, the area of the dielectric opening will affect the series resistance observed in the final current-voltage curve of the laser. For verification, 1 mm laser dies from δ-strained sample were fabricated with the largest dielectric opening possible by optical lithography. The upper limit was imposed by the required tilt accuracy in the mask alignment as the contact width approached the width of the waveguide. Surpassing this limit can result in shorting paths in the SiN isolation layer. The SEM picture of the widest achievable dielectric opening is shown in Figure 4.17a.

Figure 4.17b shows the comparison between the IV curves of the two sets of fabrication, namely the 3 μm dielectric opening on 10 μm waveguides and 6-7 μm opening on 10 μm waveguide. The observed improvement can be associated with less obscuration of the contact area with resist residue as the wider openings are used, which is favorable from the

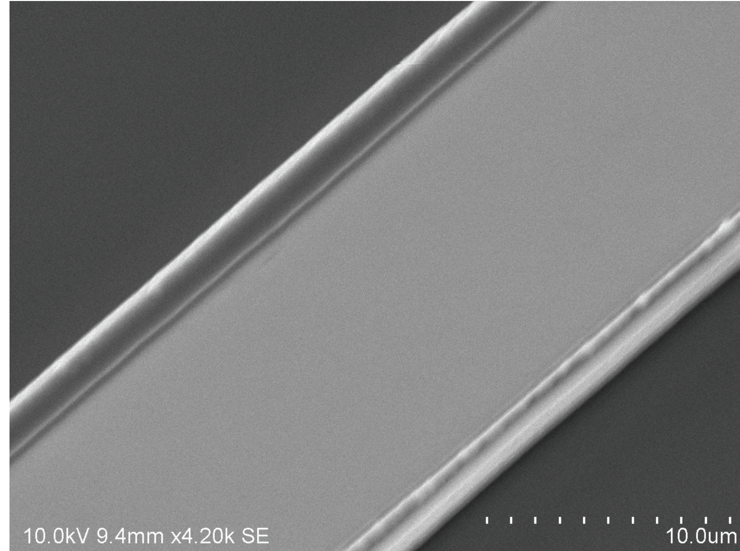

(a)

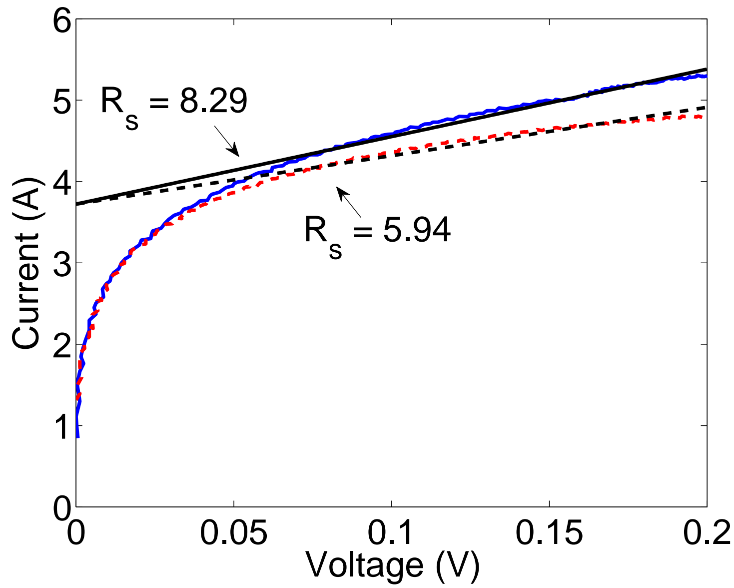

(b)

Figure 4.17: (a) SEM picture of the dielectric opening. The two narrow lines on either side of the waveguide are all that is left from the isolating SiN layer (b) The effect of narrow (solid) and wide (dashed) dielectric opening on the series resistance of a 1 mm δ-strained laser die.

fabrication point of view. However, further improvement was not observed upon employing the planarization techniques indicating the low contribution of this factor compared to the resistance of the epitaxial layers.

4.6.2 Contact Metallization

Another approach to change and improve the series resistance, is to use a different metallization scheme. Since the contact resistance was reasonably low, no effort were made to lower it any further. However, due to laser degradation at high temperatures, other metal combinations were investigated but their different contact resistance was not measured.

4.7 Packaging Considerations

4.7.1 Annealing

The stability of the laser samples at elevated temperatures has always been one of the main concerns for ICLs, especially since the temperature in the active region may rise during the CW operation regardless of the ambient temperature. The thermal resistance of a fabricated device is not isotropic. Efficient heat extraction from the devices can be accomplished by mounting the devices epi-side down which brings the active region closer to the heat-sink. Even though a soft mounting solder, like indium, requires the temperature of the device to be raised to only 160°C for a few minutes, industry standard calls for strength, reliability and resistance to corrosion that is only offered by hard solders such as Au-Sn. The melting temperatures of gold-tin alloys that are commonly used for telecommunication lasers ranges form 280 °C to 380 °C depending on the gold to tin ratio. Therefore, to determine the compatibility of the ICLs with the hard solder packaging technique, an

annealing study was conducted for temperatures around 350 °C . In this study, individual lasers were annealed in the ambient for 5 min at different temperatures from 250 °C to 350 °C and the LI and IV characteristics were measured once the device was returned to RT. Figure 4.18 plots the LI characteristics before and after annealing at 350 °C and shows the increase of threshold current for a 2 mm 12-cascade ICL with a ridge width of 10μm.

The result of annealing over 10 laser dies with different lengths from various wafers showed an increase in the threshold current density and decrease in the slope efficiency. The threshold current density increased by 35% to 40% after 5 min exposure to 350°C .

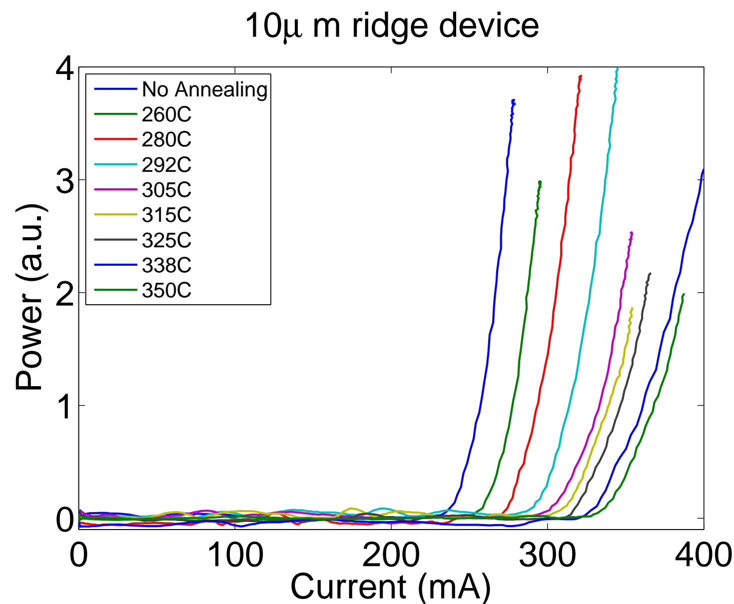

Figure 4.18: LI characteristics for a 10μm ridge 12-cascade ICL subjected to the annealing study. The devices were annealed in ambient and were tested again at room temperature for comparison.

IV characteristic of the 2 mm-long 12-cascade ICL with a ridge width of 10 μm is

shown Fig. 4.19. These graphs show the degradation in the diode characteristics of the laser after the annealing. The ICL devices typically showed a 10-20% reduction in the turn on voltage and 20-30% increase in the series resistance. This degradation seems to be associated with the diffusion of contact metals (most especially gold) into the active region and effectively degrading the quantum well structure. This degradation prohibited the use of Au-Sb solders for device packaging.

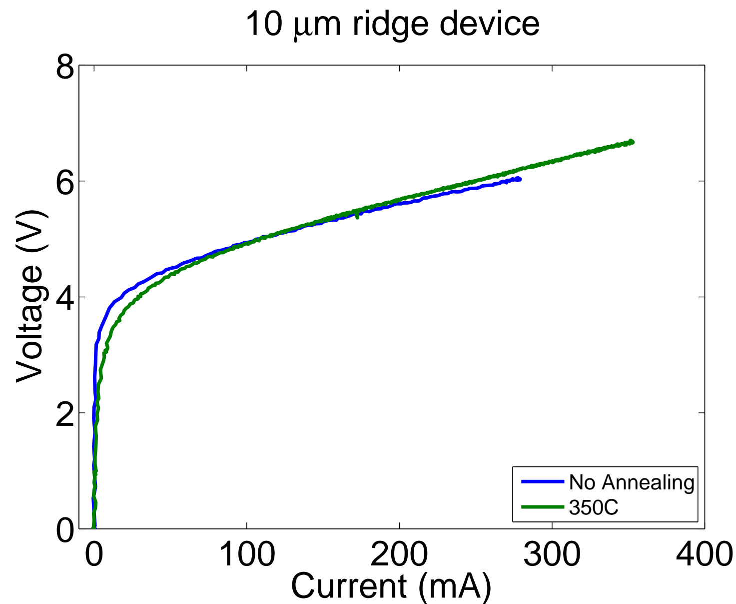

Figure 4.19: IV characteristics for a 10μm ridge 12-cascade ICL subjected to the annealing study.

4.7.2 Metal Diffusion and Contact Metal

ICL wafers are grown in temperatures around 600 °C and it is only after the contact deposition that they become sensitive to elevated temperature. Therefore, degradation of the laser diode characteristics may be associated with the diffusion of contact metal

into the active region, thereby compromising the laser performance. Secondary Ion Mass Spectroscopy (SIMS) is the ultimate way of verifying this theory. However, SIMS measurements were not accessible during the course of this project; therefore, alternative studies were performed to determine the stability of different contact metallization schemes.

The usual Ohmic contact to the laser structure consists of Ti-30 nm /Pt-100 nm /Au-150 nm. Titanium functions as an adhesive layer and platinum works as a diffusion barrier for gold. The thickness of gold in the contact composition is not of critical importance since it will be followed by 3-5 μm of electroplated gold.

Devices that use this composition were annealed to 350 °C for 5 minute (the universal annealing condition for this study) and the threshold current increased by more than 30% after annealing. Other combinations of these material system did not improve the performance. Ti-10 nm/ Pt-200 nm/ Au-150 nm and Pt-5 nm/ Ti-40 nm/ Pt-40 nm/ Au-150 nm did not outperform the standard recipe and Ti-60 nm/ Pt-40 nm/ Au-150 nm failed to achieve a proper Ohmic contact.

Other contact combinations such as Mo-25 nm/ Pt-40 nm/ Au-150 nm and Cr-2 nm/ W-50 nm/Au-150 nm were also applied to ICLs. The Mo/Pt/Au combination exhibited performance similar to the standard ICL contact recipe in terms of temperature degradation, while Cr/W/Au did not meet the Ohmic contact requirements.

The insensitivity of the device performance after annealing to the specific metallization scheme led to the conclusion that the pinholes in the SiN isolation layer are responsible for the metal diffusion. This problem may be resolved by increasing the SiN thickness or

deposition of a thin SiO_2 layer to block the SiN pinholes in future works.

4.8 Temperature Dependent Measurements of ICLs

The temperature dependence of internal laser parameters are of great importance as they directly impact the CW laser operation at and above RT. Even when the laser is kept at room temperature, the temperature inside the active region could be much higher and ultimately contribute to degrading the laser performance. In order to better understand this aspect of the ICL performance, a 1 mm-long device from the best performing structure, Fig. 4.15a, was selected and packaged. The choice of 1 mm cavity length was made to maximize the mirror loss comparable to α_i.

The mounted laser was placed in the vacuum chamber, and was operated at temperatures from -18 °C to 40 °C . The output light was collected using a lens and detected with a small area Judson lead-selenide (PbSn) detector. The reading of the detector was calibrated with the aid of an IR power meter. The lasers were operated in the pulsed mode with a 0.05% duty cycle to ensure that the temperature of the mount is equal to that of the active region. The measurement results are shown in Fig 4.20.

As can be seen from this figure, both the threshold current and the slope efficiency of the device were significantly changed with temperature. The characteristic temperatures T_0 and T_1, as described by Eq. 4.9 and 4.10, were evaluated for the threshold current and slope efficiency, as shown in Fig. 4.21. The data was fitted with a characteristic temperature T_1=90 K for the slope efficiency. This low value of T_1 indicates carrier loss due to auger assisted carrier leakage. The value of $T_0 = 38\ K$ was similarly extracted for the

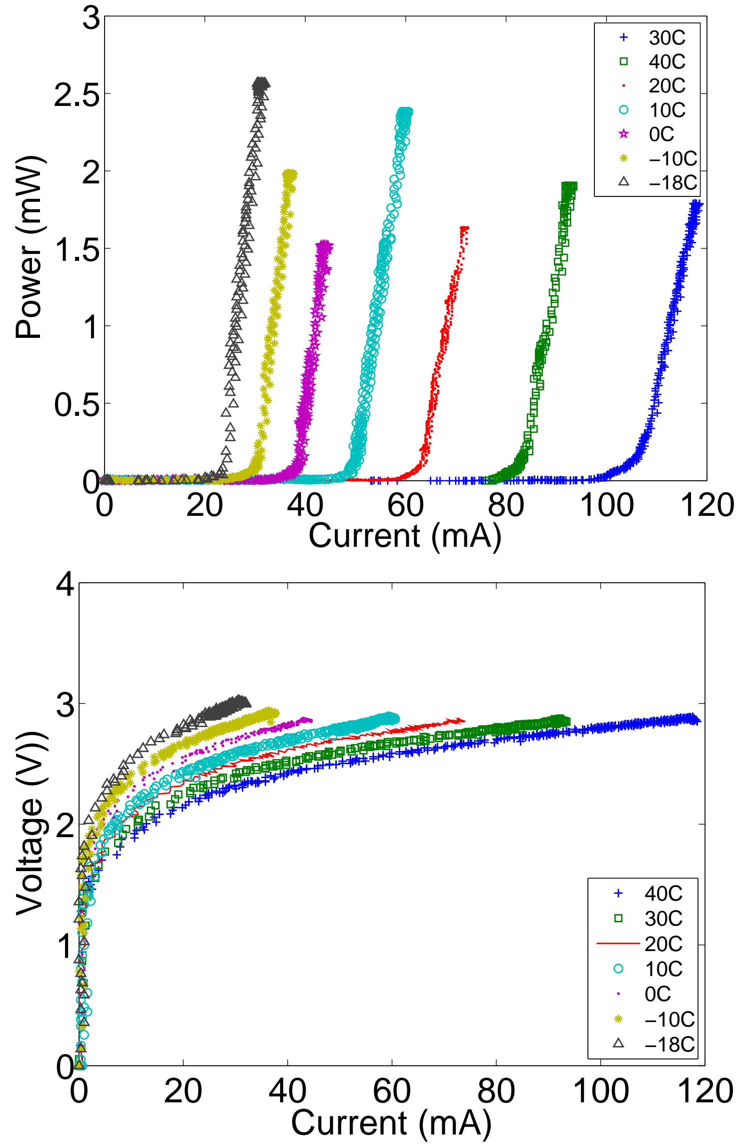

Figure 4.20: IV and LI for a 1 mm 5-cascade laser measured at different temperatures.

threshold current characteristic temperature.

From these measurements it was observed that the differential slope efficiency increased

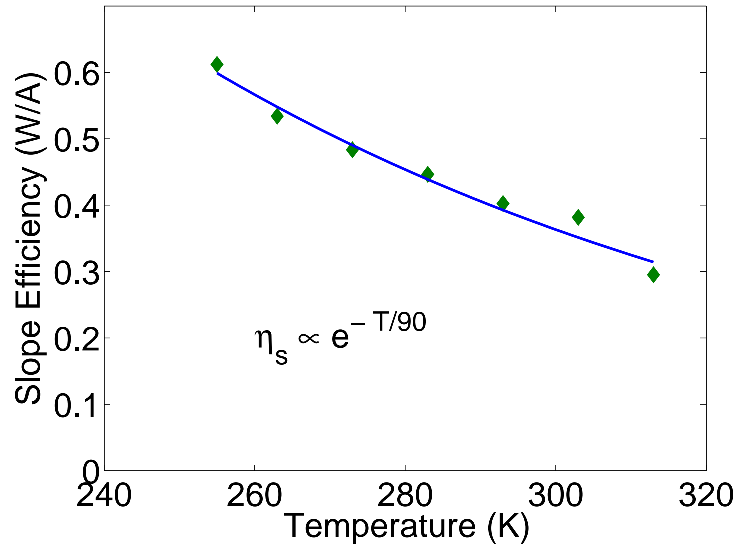

(a)

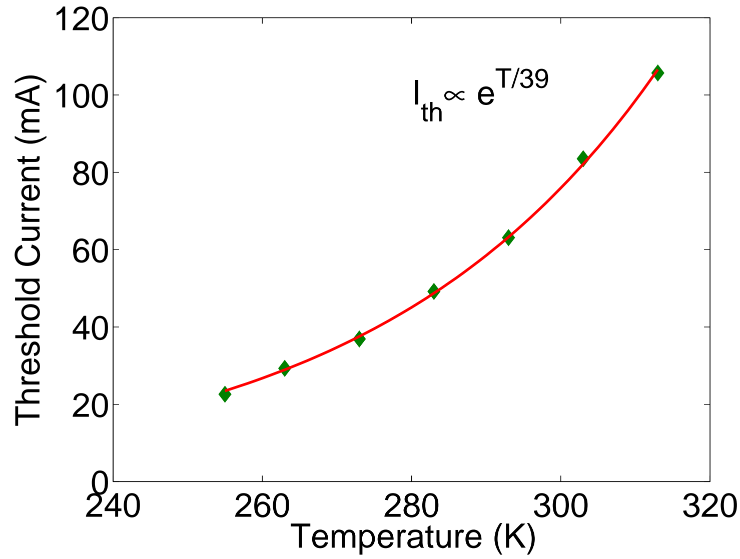

(b)

Figure 4.21: Temperature dependence of (a) slope efficiency [4] and (b) threshold current for a range of temperatures between 250K and 320K

by a factor of about 1.5 when the temperature varied from room temperature to -20 °C . Using the value of the slope efficiency at room temperature, the differential internal

efficiency, η_i, can be calculated through

$$\frac{dP}{dI} = \frac{h\nu}{2q}\eta_i N \frac{\alpha_m}{\alpha_m + \alpha_i}. \tag{4.15}$$

The length dependent analysis of these ICLs resulted in a calculated internal loss of about 5.8 cm^{-1}, as was shown in Fig. 4.10b. This leads to the value of 0.67 for $\alpha_m/(\alpha_m+\alpha_i)$ factor in Eq. 4.15 for a 1 mm long laser. Consequently, an internal quantum efficiency per stage of 31.6% at room temperature was derived.

The strong temperature dependence of the differential efficiency indicates a strong temperature dependence of the internal quantum efficiency, indicating the important role played by carrier leakage in the ICL devices. This behavior will be further investigated in the next chapter [4].

4.9 Conclusion

From the active region design point of view, the effect of the number of cascades on the device performance was experimentally investigated with 5-cascade devices outperforming all their counterparts. Other similar studies also showed that five is the optimum number of cascades that provided a reasonable balance between modal gain, internal loss, threshold power density, and thermal management [16]. Moreover, the level of the p-doping in the active region exhibited strong correlation with the internal loss, and lower loss was achieved with the lower doping level. The most important improvement was accomplished by reducing the length of the injection region which resulted in significant reduction in the threshold current density and enabled the RT CW operation. Novel designs, such as the δ-strained ICL, were also experimentally characterized and the potentials for improvements

were highlighted, most notably in the wavelength measurements. Other characteristics of the ICL devices such as the contact resistance and their permanent degradations at temperatures around 350 °C were investigated. Finally, the temperature dependence of the threshold current and slope efficiency were determined. The low characteristic temperatures of the differential slope efficiency were linked to strong temperature dependence of the internal efficiency.

Chapter 5

Mid-Infrared Anti-Reflection Coatings

5.1 Introduction

Infrared Mid-Infrared Anti-Reflection Coatings (Mid-IR ARCs) are widely used in a variety of applications where a low refractive index substrate like glass is used, *e.g.* passive optical components. In these applications the main focus is on the optical characteristics of the thin films. Whereas, optical coatings for semiconductor lasers not only require the durability and stability of regular ARCs, but also have to possess the right set of electrical characteristics and the index contrast to reach a low reflection on high-index semiconductor substrates. There are also other considerations such as the sensitivity of a particular device to heat, the compatibility of the device with a given material, and the size and geometry of a surface over which the coating is applied. An example of the effect of substrate size on the coating performance is the *border effect* [60], caused by the small surface of a laser facet $\sim 3 \times 10 \mu m^2$ and the large thicknesses of order $\sim 1 \mu m$. These phenomenon can results in

systematically thinner-than-intended coatings in ridge ICL waveguides compared to buried heterostructure geometries that are commonly used in QCLs. One of the applications of the ARCs is to achieve the highest output power for a given device, by increasing the slope efficiency which is the focus of this study. Other applications include wide band ARCs for tunable laser operation. ARCs are especially challenging in the mid-infrared region due to the high thickness of coating material that is required for low reflectivity. For a typical dielectric with the index of refraction ranging from 1.6 to 2.5, the quarter wave thickness is of the order of half a micron. Moreover, the high index of the substrate limits the theoretically achievable performance for a given material combination.

Another difficulty regarding to Mid-IR ARCs stems from the limited choice of material combinations. Most of the materials that are usually favored in Mid-IR optical coatings contain selenium (Se) or lead (Pb). Consequently, their evaporation can lead to generation of toxic fumes and is not allowed in many research environments. Other materials such as germanium or silicon, while transparent in Mid-IR, lack the adequate index contrast to the GaSb substrates of ICLs, a problem that does not exist for glass optical coatings. Moreover, for many of these materials, limited refractive index data is available in the infrared, and even those values reported in the literature considerably vary from one source to another due to different growth conditions. This issue, in turn, calls for in-house characterization of the dielectrics that are intended for optical coatings in the Mid-IR. Needless to say that the materials which are considered for ARC need to have very low absorption in the Mid-IR.

In this chapter, first the theoretical transmission and reflection formalism is reviewed and the ARC design strategy is explained. Next, the fabrication considerations and techniques are explained, and the materials considered for the ICL ARCs are reviewed. The

chapter then moves on to the experimental validation of several coating combinations, where the designed ARCs and their effect on the electro-optical performance of ICLs are explained. The methodology for extraction of the reflectivity is subsequently discussed and applied to the experimental results. Finally, the variation of internal laser parameters with the application of ARC is addressed in the last section, proposing an optimization schemes to design ARCs for Mid-IR cascade lasers.

5.2 Theory of Transmission and Reflection of Light

5.2.1 Fresnel Reflection

Transmission and reflection of electromagnetic waves at the boundary of two dielectric media can be established by considering an incident plane wave and calculating the reflected and transmitted components. Designating the direction perpendicular to the boundary as x, as shown in Fig. 5.1, all the propagation vectors should be in the plane of incidence, *i.e.* the xz plane. Assuming a monochromatic incident plane wave with frequency ω and propagation vector $\mathbf{k}$,

$$\mathbf{E_i} \exp[i\omega t - (\mathbf{k_i}.\mathbf{r})], \tag{5.1}$$

where $\mathbf{k_i}$, is the propagation vector, the reflected and transmitted waves, E_r and E_t can have the same form as Eq. 5.1 with the propagation vector $\mathbf{k_r}$ and $\mathbf{k_t}$, respectively. The magnitude of the wave numbers are:

$$k_i = k_r = \omega\sqrt{\mu\epsilon} = \frac{\omega}{c} n_1 \;\; and \;\; k_t = \frac{\omega}{c} n_2. \tag{5.2}$$

where, n_1 and n_1 are the reflective index of the dielectric media. The continuity of the

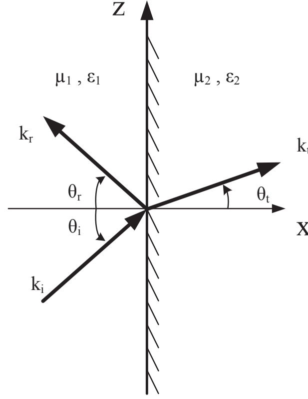

Figure 5.1: Transmission and reflection of a plane wave at the boundary of two dielectrics.

tangential component of the wave vectors requires, $k_{ix} = k_{rx} = k_{tx}$. Therefore,

$$k_i \sin(\theta_i) = k_r \sin(\theta_r) = k_t \sin(\theta_t). \tag{5.3}$$

resulting in the equality of incident and reflected angles, θ_i and θ_r, respectively and,

$$n_1 \sin(\theta_i) = n_2 \sin(\theta_t). \tag{5.4}$$

Equation 5.4 is the well-known Snell's law.

Any electromagnetic wave can be expressed as the linear combination of TE (Transverse Electric) or s (from senkrecht, German for perpendicular) and TM (Transverse Magnetic) or p (parallel) waves. These two polarizations are treated separately in what follows.

5.2.2 Transverse Electric Plane Wave

For TE polarization, the electric fields in medium 1 and 2, $\mathbf{E_1^{\pm}}$ and $\mathbf{E_2^{\pm}}$, respectively, are perpendicular to the plane of incidence and the magnetic fields, $\mathbf{H_1^{\pm}}$ and $\mathbf{H_2^{\pm}}$ lie in the plane

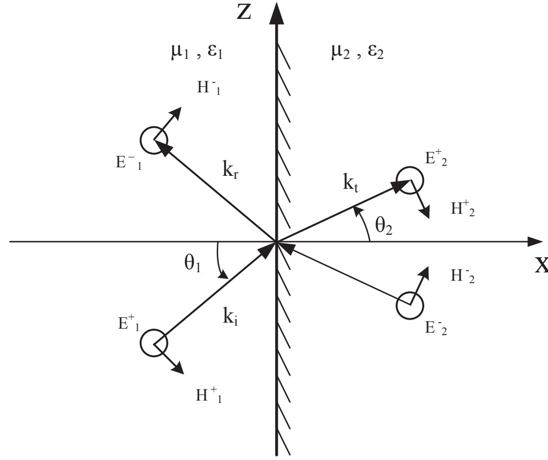

Figure 5.2: Transmission and reflection of a TE polarized plane wave at the boundary of two dielectrics.

of incidence as shown in Fig. 5.2. Therefore, from the continuity of electric and magnetic components parallel to the boundary,

$$\begin{aligned} E_1^+ + E_1^- &= E_2^+ + E_2^- \\ H_1^+ \cos\theta_1 - H_1^- \cos\theta_1 &= H_2^+ \cos\theta_2 - H_2^- \cos\theta_2. \end{aligned} \tag{5.5}$$

Maxwell equations relate the magnitude of electric and magnetic fields of a plane wave as, $H = E/\eta$, where, $\eta = \sqrt{\mu/\epsilon}$ is the characteristic impedance. Using this relation, Eq. 5.5 can be expressed as,

$$\begin{aligned} E_1^+ + E_1^- &= E_2^+ + E_2^- \\ \frac{\cos\theta_1}{\eta_1}(E_1^+ - E_1^-) &= \frac{\cos\theta_2}{\eta_2}(E_2^+ - E_2^-). \end{aligned} \tag{5.6}$$

Equation 5.6 may also be written in matrix form,

$$\begin{pmatrix} 1 & 1 \\ \frac{\cos\theta_1}{\eta_1} & -\frac{\cos\theta_1}{\eta_1} \end{pmatrix} \begin{pmatrix} E_1^+ \\ E_1^- \end{pmatrix} = \begin{pmatrix} 1 & 1 \\ \frac{\cos\theta_2}{\eta_2} & -\frac{\cos\theta_2}{\eta_2} \end{pmatrix} \begin{pmatrix} E_2^+ \\ E_2^- \end{pmatrix} \tag{5.7}$$

or

$$D_{TE1} \begin{pmatrix} E_1^+ \\ E_1^- \end{pmatrix} = D_{TE2} \begin{pmatrix} E_2^+ \\ E_2^- \end{pmatrix} \tag{5.8}$$

where the D_{TEi} is the dynamical matrix of medium i for TE-polarization,

$$D_{TEi} = \begin{pmatrix} 1 & 1 \\ \frac{\cos\theta_i}{\eta_i} & -\frac{\cos\theta_i}{\eta_i} \end{pmatrix}. \tag{5.9}$$

When $E_2^- = 0$, the transmission and reflection coefficients are defined as:

$$r_{TE} = \left(\frac{E_1^-}{E_1^+}\right), \quad t_{TE} = \left(\frac{E_2^+}{E_1^+}\right) \tag{5.10}$$

Assuming non-magnetic media, *i.e.* $\mu_1 = \mu_2 = \mu_0$, the Fresnel equation for TE polarization is obtained,

$$\begin{aligned} r_{TE} &= \frac{n_1\cos\theta_1 - n_2\cos\theta_2}{n_1\cos\theta_1 + n_2\cos\theta_2} = \frac{k_{1x} - k_{2x}}{k_{1x} + k_{2x}} \\ t_{TE} &= \frac{2n_1\cos\theta_1}{n_1\cos\theta_1 + n_2\cos\theta_2} = \frac{2k_{1x}}{k_{1x} + k_{2x}}. \end{aligned} \tag{5.11}$$

5.2.3 Transverse Magnetic Plane Wave

For TM-polarized plane wave the electric field is in the plane of incidence, as schematically illustrated in Fig. 5.3, and the boundary condition for the continuity of parallel components

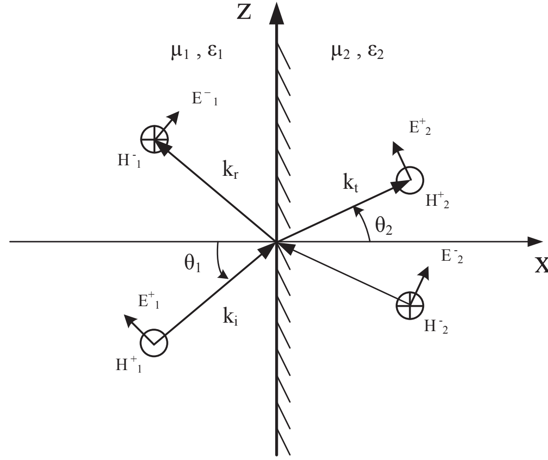

Figure 5.3: Transmission and reflection of a TM polarized plane wave at the boundary of two dielectrics.

of the fields becomes:

$$\begin{aligned} E_1^+ \cos\theta_1 + E_1^- \cos\theta_1 &= E_2^+ \cos\theta_2 + E_2^- \cos\theta_2 \\ H_1^+ - H_1^- &= H_2^+ - H_2^-, \end{aligned} \tag{5.12}$$

which simplifies to,

$$\begin{aligned} \cos\theta_1(E_1^+ + E_1^-) &= \cos\theta_2(E_2^+ + E_2^-) \\ \frac{E_1^+ - E_1^-}{\eta_1} &= \frac{E_2^+ - E_2^-}{\eta_2}. \end{aligned} \tag{5.13}$$

Using the relation between electric and magnetic fields of a plane wave, $H = E/\eta$, equation 5.13 can be expressed in the matrix form,

$$\begin{pmatrix} \cos\theta_1 & \cos\theta_1 \\ \frac{1}{\eta_1} & -\frac{1}{\eta_1} \end{pmatrix} \begin{pmatrix} E_1^+ \\ E_1^- \end{pmatrix} = \begin{pmatrix} \cos\theta_2 & \cos\theta_2 \\ \frac{1}{\eta_2} & -\frac{1}{\eta_2} \end{pmatrix} \begin{pmatrix} E_2^+ \\ E_2^- \end{pmatrix}, \tag{5.14}$$

or equivalently,

$$D_{TM1} \begin{pmatrix} E_1^+ \\ E_1^- \end{pmatrix} = D_{TM2} \begin{pmatrix} E_2^+ \\ E_2^- \end{pmatrix}, \tag{5.15}$$

where the dynamical matrix of TM-wave in the medium i is:

$$D_{TMi} = \begin{pmatrix} \cos\theta_i & \cos\theta_i \\ \frac{1}{\eta_i} & -\frac{1}{\eta_i} \end{pmatrix}. \tag{5.16}$$

Transmission and reflection coefficient at $E_2^- = 0$ are defined as,

$$r_{TM} = \left(\frac{E_1^-}{E_1^+}\right), \quad t_{TM} = \left(\frac{E_2^+}{E_1^+}\right), \tag{5.17}$$

and the non-magnetic media assumption, i.e. $\mu_1 = \mu_2 = \mu_0$, gives the Fresnel equation for TM polarization,

$$\begin{aligned} r_{TM} &= \frac{n_1\cos\theta_2 - n_2\cos\theta_1}{n_1\cos\theta_2 + n_2\cos\theta_1} = \frac{n_1^2 k_{2x} - n_2^2 k_{1x}}{n_1^2 k_{2x} + n_2^2 k_{1x}}, \\ t_{TM} &= \frac{2n_1\cos\theta_1}{n_1\cos\theta_2 + n_2\cos\theta_1} = \frac{2n_1^2 k_{2x}}{n_1^2 k_{2x} + n_2^2 k_{1x}}. \end{aligned} \tag{5.18}$$

Since ICLs are TE polarized, the respective equations for TE polarization has been used in the calculations describes in the rest of the chapter.

5.2.4 Reflectance and Transmittance

The Fresnel coefficients represent the ratio of the amplitude of the transmitted/reflected to the incident field. Transmittance and reflectance are defined as the ratio of the reflected

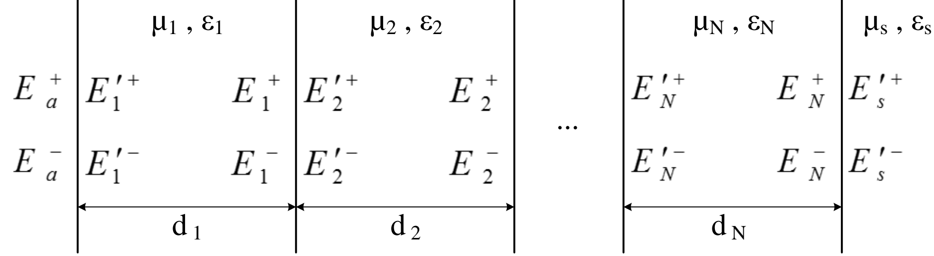

Figure 5.4: Multi-layer dielectric interface

and transmitted power to incident power normal to the boundary.

$$R = \left|\frac{\mathbf{n}\ .\ \mathbf{S_r}}{\mathbf{n}\ .\ \mathbf{S_i}}\right|, \qquad T = \left|\frac{\mathbf{n}\ .\ \mathbf{S_t}}{\mathbf{n}\ .\ \mathbf{S_i}}\right| \tag{5.19}$$

where $\mathbf{S} = 1/2\mathbf{Re}(E \times H^*)$ is the time average Poynting's vector. The transmittance and reflectance are related to the Fresnel coefficients for a nonmagnetic media via,

$$R = \left|r^2\right|, \qquad T = \frac{n_2 \cos\theta_2}{n_1 \cos\theta_1}\left|t^2\right| \tag{5.20}$$

5.2.5 Matrix Formulation for Multi-layer Systems

Equations 5.8 and 5.15 can be used to describe transmission and reflection in such complex multi-layer systems as illustrated in Fig. 5.4. From Eq. 5.8 and Fig 5.4,

$$D_a \begin{pmatrix} E_a^+ \\ E_a^- \end{pmatrix} = D_1 \begin{pmatrix} E_1^{+'} \\ E_1^{-'} \end{pmatrix} \Longrightarrow \begin{pmatrix} E_a^+ \\ E_a^- \end{pmatrix} = D_a^{-1} D_1 \begin{pmatrix} E_1^{+'} \\ E_1^{-'} \end{pmatrix}. \tag{5.21}$$

Moreover,

$$\begin{pmatrix} E_1^{+'} \\ E_1^{-'} \end{pmatrix} = \begin{pmatrix} e^{i\phi_1} & 0 \\ 0 & e^{-i\phi_1} \end{pmatrix} \begin{pmatrix} E_1^+ \\ E_1^- \end{pmatrix} = P_1 \begin{pmatrix} E_1^+ \\ E_1^- \end{pmatrix} \tag{5.22}$$

where P_1 is defined by,

$$P_1 = \begin{pmatrix} e^{i\phi_1} & 0 \\ 0 & e^{-i\phi_1} \end{pmatrix} \tag{5.23}$$

and $\phi_1 = k_{1x}d_1$. Therefore, the electric fields pre- and post-transmission through an N-layer material system are related via,

$$\begin{pmatrix} E_a^+ \\ E_a^- \end{pmatrix} = D_a^{-1} \left(\prod_{j=1}^{N} D_j P_j D_j^{-1} \right) D_s \begin{pmatrix} E_s^{+'} \\ E_s^{-'} \end{pmatrix} \tag{5.24}$$

The overall transformation Matrix M for a multi-layer system is,

$$\mathrm{M} = D_a^{-1} \left(\prod_{j=1}^{N} D_j P_j D_j^{-1} \right) D_s, \tag{5.25}$$

where D_i matrices are defined according to Eq. 5.8 and Eq. 5.15, for the two polarizations.

5.2.6 Mode Decomposition and ARC Design

The transmission and reflection formalism developed in the previous section only applies to plane electromagnetic waves. However, in a semiconductor laser, light is confined in an optical mode which is a composition of series of plane waves. In order to utilize the developed method and optimize the dielectric structure, the optical mode can be decomposed to its plane wave components prior to application of the matrix formulation.

The Fourier transform decomposition of the optical mode,

$$E_{inc}(k_x) = \mathcal{F}\left\{E_{inc}(x)\right\} = \int_{-\infty}^{\infty} E(x)e^{-ikx}dx \tag{5.26}$$

converts the electric field to spatial frequency domain. The x and z components of the

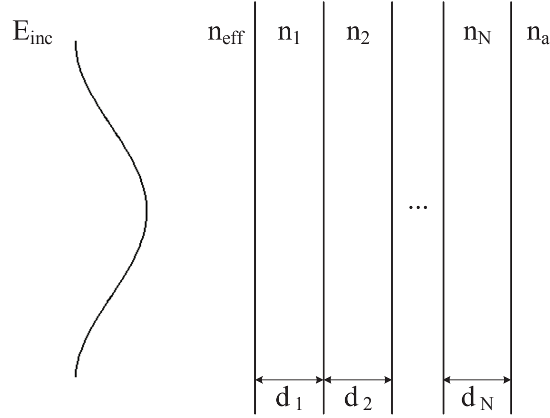

Figure 5.5: Waveguide mode and multi-layer coating

wave vector are related as $k_x^2 = n_{eff}^2 k_0^2 - k_z^2$ where $k_0 = 2\pi/\lambda$ is the free space propagation vector. The angle of incidence for each k_x is defined as $\theta = \tan^{-1}(\frac{k_z}{k_x})$.

The angular span of the mode can also be approximated by a Gaussian beam with divergence cone half-angle of

$$\theta_{max} = \frac{2}{\pi}\frac{\lambda}{2W_0}. \tag{5.27}$$

From the $1/e$ width of the Gaussian fit, W_0, gives the same W_{max} as the angular spread of the mode in k-space.

The reflection coefficient, $r(k_x)$ for each k_x and θ can be determined using the matrix formulation. The reflected field from Eq. 5.10 and 5.17 is

$$E_{\text{ref}}(k_x) = r(k_x)E_{\text{inc}}(k_x). \tag{5.28}$$

The reflectivity is given by the overlap integral between the incident and reflected beams

to account for the amount of light that is coupled back to the waveguide,

$$R = \frac{\left|\int_{-\infty}^{\infty} E_{\text{inc}}(z)E_{\text{ref}}(z)dz\right|^2}{\left|\int_{-\infty}^{\infty} E_{\text{inc}}(z)^2dz\right|^2}. \tag{5.29}$$

5.2.7 Merit Function

For a given set of material refractive indices, the goal is to find the corresponding thicknesses that result in the target reflectance, $R_t(\lambda)$. Defining the parameter space X as:

$$X = \{d_1, d_2, .., d_N\} \tag{5.30}$$

the reflectance will become a function of X and λ, i.e. $R(X, \lambda)$. The mean square formula [61],

$$F(x) = \int_{\lambda_i}^{\lambda_f} [R(x, \lambda) - R_t(\lambda)]^2 d\lambda \tag{5.31}$$

estimates the difference between the reflectivity of a multi-layer system and the target reflectance. A Matlab program [5] based on the described matrix formulation evaluates the merit function for the wavelength of interest over a range of material thicknesses. The thicknesses corresponding to the function minimum are then selected and used in ARC experiments.

5.3 Anti-Reflection Coating Facility with *in-situ* Reflectometry

The e-beam evaporator used for the AR coatings deposition is shown in Figure 5.6. In this evaporator the thickness of the deposited film can be monitored accurately with the *in-*

situ reflectometer [62]. The reflectometer consists of a transmitter and a receiver arm, as

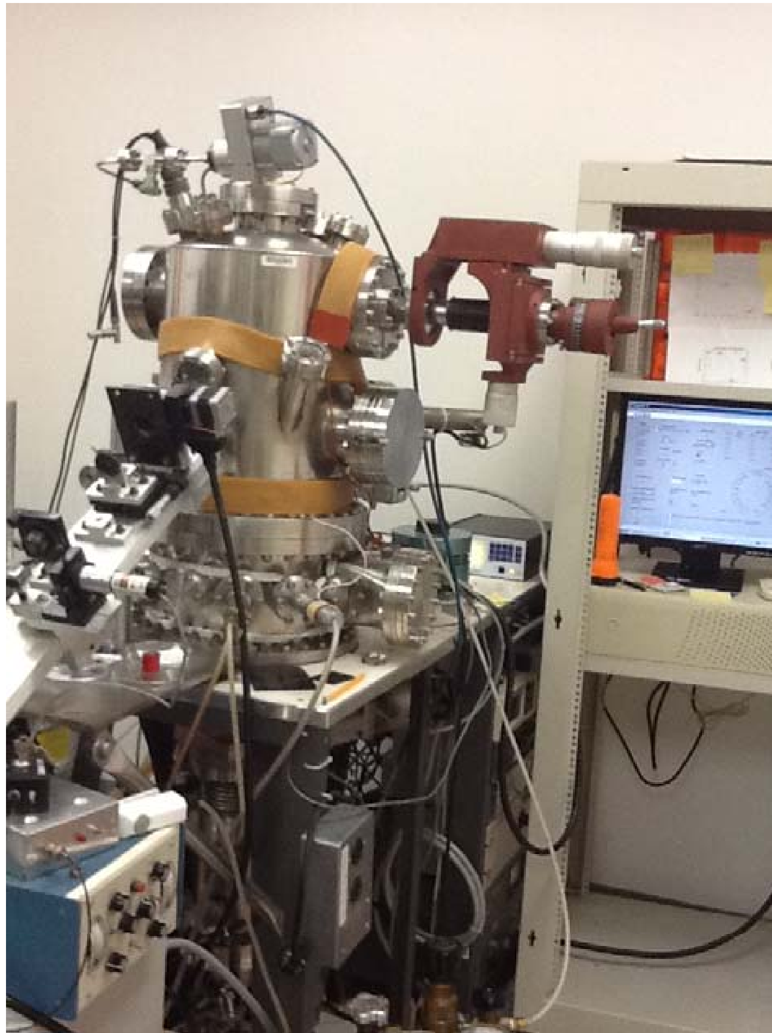

Figure 5.6: E-beam evaporation Facility equipped with an *in-situ* reflectometer.

schematically illustrated in Fig.5.7. The transmitter arm includes a laser diode at 1.31 μm a $\lambda/4$ wave-plate, and a polarizer. The receiver arm consists of a rotating analyzer and

a germanium detector. A 650 nm visible laser diode and multiple irises are placed in the transmitter and receiver arm to aid the alignment. The germanium detector allows for the detection of both lasers. Two Glan-Thomson polarizers are used in the system that work in wavelengths from 350 nm to 2300 nm. The polarizer in the transmitter arm is installed on a Newport URM80APP motorized stage that moves with the resolution of 0.001°. The analyzer in the receiver arm is mounted on a rotary stage which can turn at 60 rpm. The rotary stage also provides the initial revolution angle for referencing.

The transmitter arm is designed at an angle of about 60° with respect to the chamber, which is close to the Brewster angle, suppressing the reflections from a TM polarized light. The collimated laser beam passes through the quarter wavelength plate, which can adjust the polarization. A computerized system then measures the optical power as a function of the analyzer angle in the vicinity of TE and TM polarizations determined by the polarizer in the transmitter arm. The information extracted from these two measurements is used to set the right angle for both polarizer and analyzer to obtain a pure TE-polarized light in order to minimize the measurement error [63].

This system can be used as an ellipsometer as well as a reflectometer, both of which can be employed in monitoring the thickness of optical coatings. Methods based on ellipsometry are, however, very sensitive, computationally demanding, and suffer from accumulative error in multi-layer coatings. Single wavelength laser reflectometry simply uses the extrema of the reflectance curve as an indication of multiples quarter wavelength thicknesses, a method that is also known as the turning-value monitoring [64]. The decrease in the rate of change of the reflectance curve at its extrema is one of the major sources of error in the turning value monitoring method. An improvement over direct turning-point monitor-

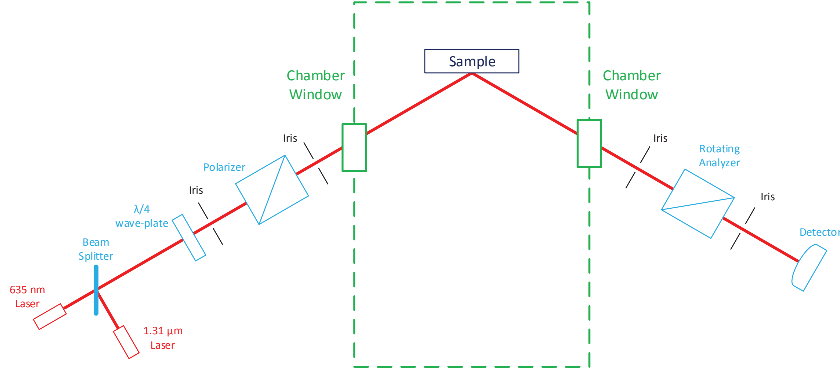

Figure 5.7: schematic of the e-beam evaporation facility equipped with an *in-situ* reflectometer [5].

ing can be achieved by monitoring the reflectance at a shifted wavelength, thereby taking advantage of the much higher rate of change far from the turning points [63]. The turning-value monitoring at a single shifted wavelength has been used in the following coating experiments. Since it is not possible to measure the reflectance directly at the laser facet due to its small dimensions $\sim 30\ \mu m^2$, the monitoring has been done on a witness sample which is usually a 1 cm × 1 cm silicon sample.

Given the refractive indices of the coating layers, and the thicknesses obtained from the ARC design, the theoretical evolution of the optical power during film growth is calculated in order to provide a map for the ARC fabrication. For example, the reflectometry map for the ZnS-YF_3 double layer ARC at $\lambda = 3.4\ \mu m$ with the final thickness of 265 nm for ZnS and 422 nm for YF_3 is given in Fig. 5.8. It should be noted that since monitoring the thickness is performed at $\lambda =\ 1.31 \mu m$ on a silicon sample, the coating material indices as well as the silicon substrate index, used in the generation of deposition map, should be selected form the same point of wavelength in their dispersion curves. The incident beam angle of 60° was also incorporated into the calculations.

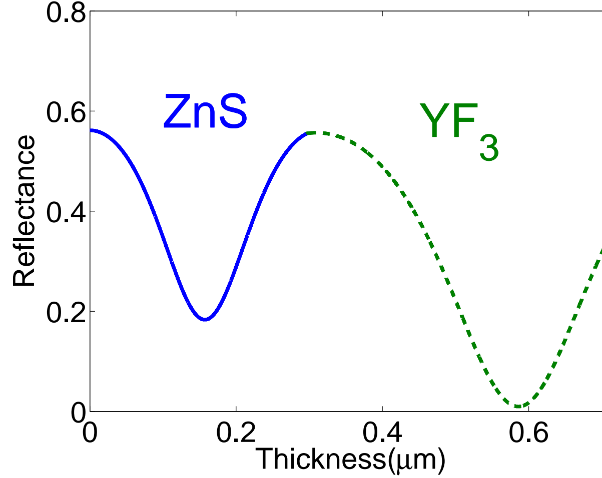

Figure 5.8: reflectometry map for a double layer ZnS-YF_3 AR coating at $\lambda = 3.4\mu m$

5.3.1 Single Layer Coating

A quarter wavelength thick dielectric layer with an index of refraction within the range defined by substrate refractive index and ambient comprises a single layer anti-reflection coating. For single layer coating, from the matrix formulation, it can be shown that the minimum reflectivity at normal incidence and TE polarization is reached when

$$n_1 = \sqrt{n_a n_s}, \tag{5.32}$$

where n_a and n_s are the ambient and substrate refractive indices respectively. The change in the effective index of the optical mode of the laser cavity for the various MBE-grown structures and waveguide designs is relatively small with the average value of 3.59. Therefore, the optimum index of refraction for a single layer coating is about 1.89. Figure 5.9

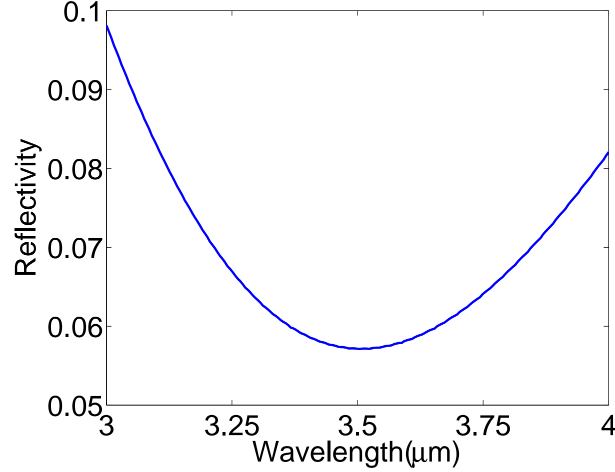

Figure 5.9: Al_2O_3 single layer coating layer reflectivity designed for a 5-cascade ICL at 3.5μm.

shows the reflectivity spectrum of a 610 nm thick single layer Al_2O_3 ARC designed for an ICL at 3.5μm. An index of refraction of 1.54 was used for Al_2O_3 at this wavelength. Optimum index is an ideal condition and represents one of many parameters that determine the choice of the material. These parameters are further discussed in section 5.4.

5.3.2 Multi-Layer Coating

For multi-layer coatings and the normal wave incidence, the optimum index of refraction for each layer is the geometric mean of the indices of refraction of the two adjacent layers. Hence, the index of refraction of the m_{th} layer of an M-layer stack is given by

$$n_m = n_a^{\frac{M+1-m}{M+1}} n_s^{\frac{m}{M+1}}. \tag{5.33}$$

This condition provides the optimum index for broadband coating at normal incidence

and TE polarization. For double layer AR coating, two materials are needed with optimal indices of,

$$n_1 = n_a^{2/3} n_s^{1/3},$$
$$n_2 = n_a^{1/3} n_s^{2/3}, \tag{5.34}$$

where n_a is the air refractive index and n_s is the effective index of the waveguide mode, which is close to 3.59 for a narrow ridge interband cascade laser, yielding ideal index values of $n_1 = 1.53$ and $n_2 = 2.34$.

In general, multi-layer coatings provide more degrees of freedom for tailoring the design to the application needs such as a specific reflectivity or bandwidth requirement. Additionally, the order in which these materials are deposited is also an added freedom to the design of a multi-layer coating. For a double layer coating, for example, the dielectric coatings can be arranged in high-low (H/L) or low-high (L/H) combinations depending of which material is deposited first on the substrate. The order will effect the bandwidth of the coating. Figure 5.10 shows the contour map of the merit function for a wide span of thicknesses. A more focused map over the first minimum, which corresponds to the lowest required thickness of the two materials to provide the minimum reflectivity is also shown. The corresponding reflectivity spectrum for the optimum thicknesses combination, *i.e.* 266 nm of ZnS and 418 nm of YF_3 is shown in Fig. 5.11. This coating is designed for a narrow ridge delta-strained interband cascade laser at 3.4μm.

Comparison between Fig. 5.9 and Fig. 5.11 highlights the feasibility of much lower reflectivity with double layer coating. While single layer coating is certainly an attractive option due to its simplicity, more stringent ARC performance criteria calls for double or even multi-layer coatings.

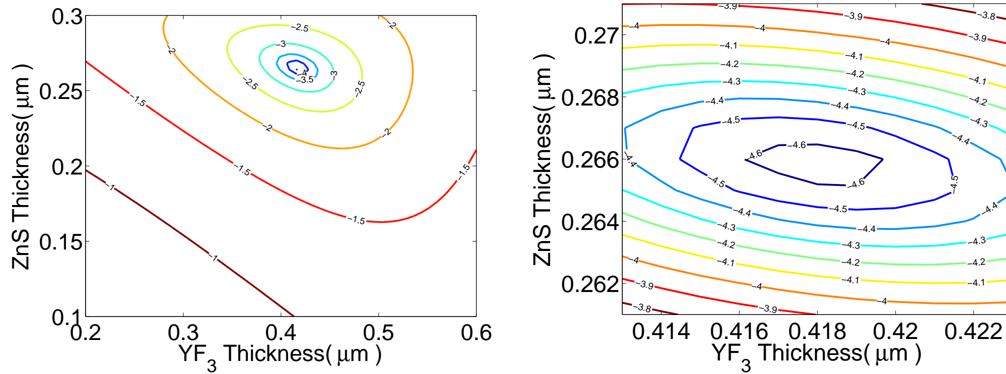

Figure 5.10: ZnS-YF_3 double layer merit function contour.

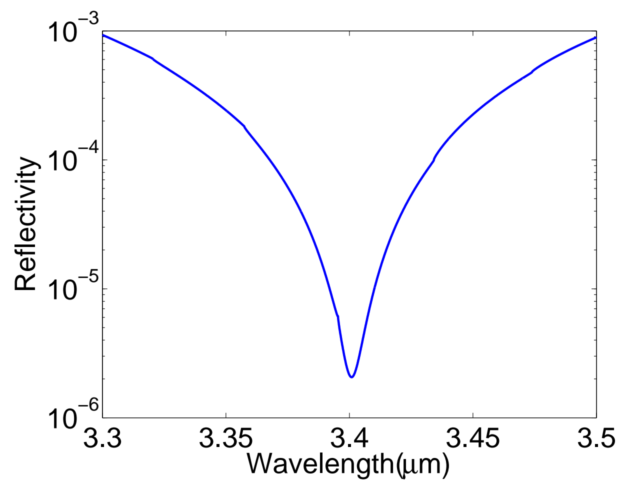

Figure 5.11: ZnS-YF_3 double layer reflectivity spectrum

5.4 Materials for Infrared Coatings

The materials that are considered for anti-reflection coatings must meet the design criteria including transparency in the region of interest and matching refractive index to the application demands as well as capability to form quality thin films by the intended fabrication technique. Due to long wavelengths in the infrared region, coating thicknesses are usually

in the order of hundreds of nanometers, which places an additional restriction on the thin film quality due to the potential for added stress in a thick dielectric film.

The materials that were considered for ICL ARCs underwent three type of characterizations:

- refractive index characterization,
- tape test,
- scanning electron microscopy (SEM).

The refractive indices for common materials can be found in the literature. However, the reported values usually vary considerably from one reference to the other because of the different quality and characteristics of the dielectric films formed by various deposition techniques. In order to estimate the refractive index of the materials deposited using the e-beam evaporator in which the actual ARC is made, a thin layer of the dielectric was deposited on a silicon sample. The refractive index of this thin film was then measured in the visible range, 0.4-0.7 μm using a Woollam ellipsometer.

The refractive index is, in general, a function of wavelength. Dispersion is the change in the refractive index with wavelength. One of the most familiar phenomenon that presents this fact is the formation of rainbow in the sky. Moreover, all of the materials have absorption bands, which lead to anomalous dispersion. The wavelength regions that are far from these absorption bands obey the normal dispersion. The refractive index of a material is usually measured at discrete wavelengths and are fitted with proper dispersion curves. In 1871 Sellmeier proposed a mathematical description that describes the material as a collection of harmonic oscillators with different resonant frequencies/wavelengths.

Sellmeier's equation with general application to various materials and wavelengths is,

$$n^2(\lambda) = 1 + \sum_{i=1}^{m} \frac{a_i \lambda^2}{(\lambda^2 - \lambda_i)} \tag{5.35}$$

where λ_i represents the wavelength of absorption bands, a_i is the harmonic oscillator strengths [65]. The normal dispersion curve was first proposed by Cauchy in 1836,

$$n = A + \frac{B}{\lambda^2} + \frac{C}{\lambda^4} \tag{5.36}$$

where A,B and C are the characteristic constants of the material [66].

It can be shown that in the limit of $\lambda \gg \lambda_i$ i=1,...,m, Cauchy equation can be derived as an approximation to the Sellmeier's equation. Therefore, based on the proximity of the absorption bands of the materials that are used in ICL AR coating to the 3-4 μm region, Cauchy or Sellmeier equations were chosen to fit the experimental ellipsometry data and estimate the refractive index in the mid-IR region.

Additionally, for the multi-layer coating to work and last, the coating must adhere to the substrate. A standard method for qualifying the adhesion of dielectric layer to the substrate, as recognized by American Society for Testing and Materials (ASTM), is the tape test [67]. This method can be easily employed by applying and removing a tape to the calibration sample.

Finally, the SEM images of the dielectric coatings are used to examine the overall appearance of the coating and provide information about the macroscopic quality of the deposited layers. Figure 5.12 shows the SEM picture of double layer ZnS-SiO_2 AR coating

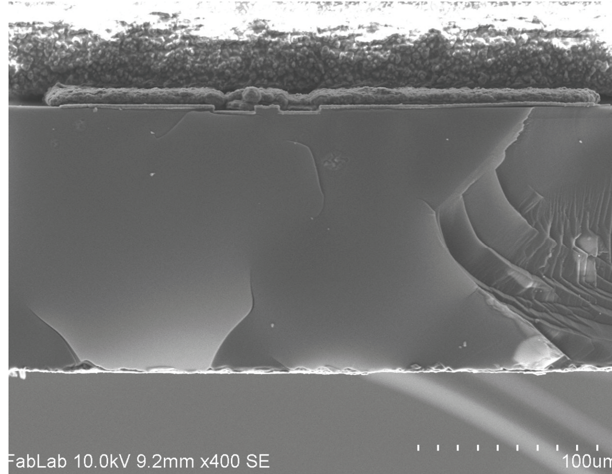

Figure 5.12: ZnS-SiO_2 double layer AR coating in the absence of the Ta_2O_5 adhesion layer.

applied to the facet of an ICL without the Ta_2O_5 adhesion layer. This picture demonstrates the fragility of the coating structure and the peeling at the corners caused by poor adhesion of ZnS and accumulated stress in the deposition of thick dielectric layers.

In order to span a wide range of reflectivity with the simplest coating combination, materials close to the optimum require refractive index were considered. For an ICL ridge waveguide with the optimum single layer coating should have an index of refraction equal to 1.87, *i.e.* the geometric mean of the effective refractive index of the waveguide and air. However, considering the material limitation, it is not possible to match this ideal value. Consequently, the available materials close to this index, Ta_2O_5, ZrO_2, and Al_2O_3, were selected. For double layer coating two materials with high and low refractive indices are required. While choices for a low-index material are relatively broad, there are only a few high-index materials that are suitable for optical coatings in the mid-infrared region and possess the required index difference with the substrate. Given the optimal refractive indices for a double layer coating, ZnS and TiO_2 were considered for the high-index layer

Table 5.1: Thin-film dielectrics and their measured refractive indices

Dielectric Materials	**Approximate Index of Refraction at Mid-IR**
ZrO_2	1.84
Ta_2O_5	1.73
Al_2O_3	1.54
ZnS	2.24
TiO_2	1.77
SiO_2	1.37
YF_3	1.41

with refractive indices around 2. For low-index layers YF_3 and SiO_2 with the index of ~ 1.4 in the infrared region were used. All of these dielectrics were evaporated in the same e-beam evaporation chamber where the actual ARC was made and were characterized individually with a Woollam ellipsometer at shorter wavelengths. The refractive index was then estimated though fitting Sellmeier or Cauchy equation to ellipsometry measurements depending on the material characteristics. The details of these fittings are summarized in Appendix. A. Table 5.1 lists the dielectric materials that have been selected as well as their approximate refractive indices in the Mid-IR.

5.5 Experimental Results

In this section the experimental results for several ARC designs are reviewed. The details of the dielectric thickness and reflectivity for each design are provided in Appendix B

5.5.1 Single Layer AR Coating

Given that the refractive index of ZrO_2 is 1.84 in the infrared region, a 480 nm layer of ZrO_2 was evaporated on the facet of a 5-cascade laser with the $\lambda = 3.5$ μm, as Fig. 5.13 shows. This coating did not result in any improvement in the slope efficiency. Several other experiments with different ICLs also were unsuccessful with this material. Therefore, ZrO_2 was not considered in the following experiments for improvement of laser output power.

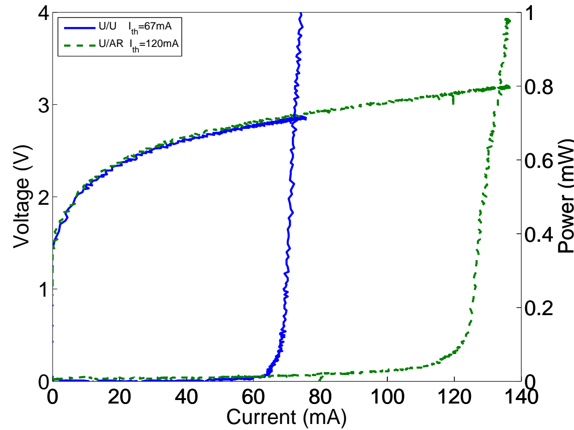

Figure 5.13: ZrO_2 single layer AR coating for 5-cascade laser $\lambda = 3.5$ μm with cavity length of 2 mm.

Ta_2O_5 is the next promising candidate due to its close-to-optimum index of 1.73 and its transparency at infrared. Figure 5.14 demonstrates the single layer coating of a 5-cascade ICL laser with wavelength of 3.8 μm and dielectric thickness of 580 nm.

The degradation in the laser performance was seen on a number of samples. Further investigations showed that this behaviour is associated with the columnar growth of the dielectric, as it is apparent from the SEM picture in Fig. 5.15, resulting in rough surfaces and diffusive reflectance. Therefore, Ta_2O_5 was also ruled out of the selection list for Mid-

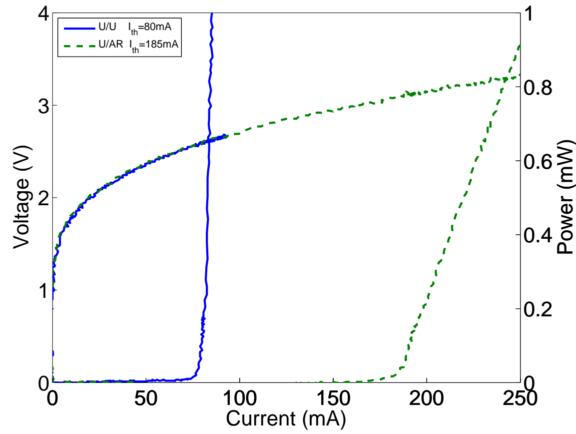

Figure 5.14: Ta_2O_5 single layer AR coating for 5-cascade laser $\lambda = 3.8\ \mu m$ with cavity length of 1 mm.

IR anti-reflection coatings.

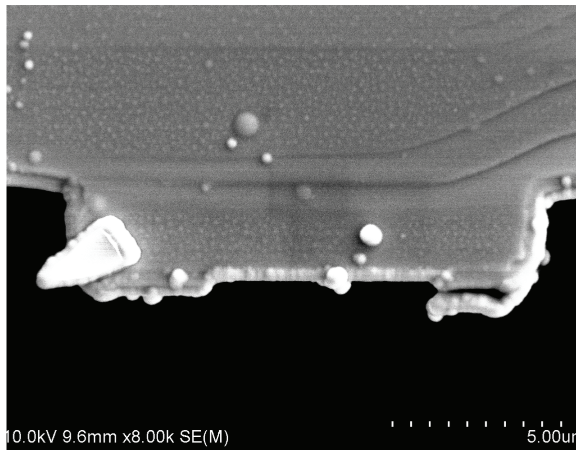

Figure 5.15: SEM picture of the 5-cascade laser coated with 495 nm of Ta_2O_5

Al_2O_3 with the index of around 1.54 in the infrared region is not exactly a perfect match for the single layer AR coating in the first glance. However, this dielectric forms good quality thin films and it is widely used in optics. Figure 5.16 shows a 1 mm ICL with

5-cascade at 3.5 μm coated with a 610 nm single layer of Al_2O_3. The slope efficiency has improved by a factor of 1.33 as emphasized in the inset. Unfortunately Al_2O_3 evaporates at relatively high e-beam gun power and was not compatible with the e-beam evaporator equipped with the *in situ* refractometry. Therefore, it was not possible to monitor the dielectric thickness as accurately as needed for optical coatings. Nevertheless, this result shows that Al_2O_3 is a suitable candidate for a simple single layer coating in the mid-infrared region.

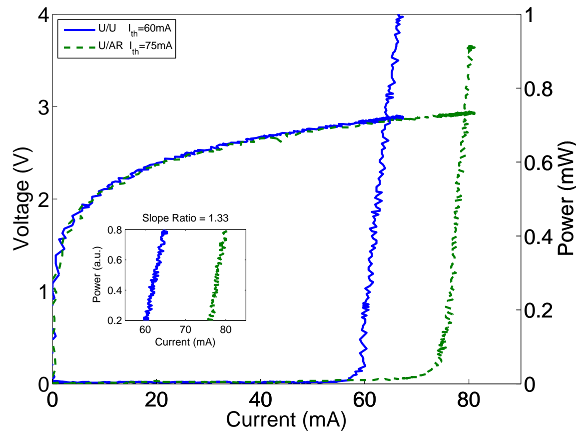

Figure 5.16: Al_2O_3 single layer AR coating for 5-cascade laser at $\lambda = 3.5\ \mu m$ with cavity length of 1 mm.

5.5.2 Double Layer AR Coating in ICL

ZnS-YF_3 combination was first applied in L/H index arrangement to a δ-strained ICL with cavity length of 1 mm. Figure 5.17 shows the measurement result for this device before and after the AR coating. This coating resulted in improvement of the slope efficiency by a factor of 1.5, as shown in the inset.

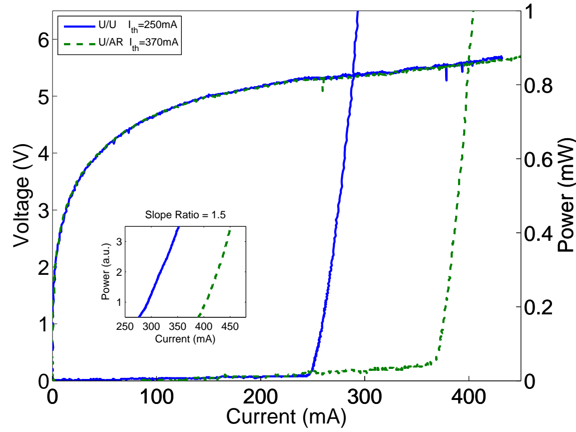

Figure 5.17: YF_3-ZnS double layer AR coating for δ-strained ICL with cavity length of 1 mm.

Figure 5.18 shows the result of H/L combination applied to a δ-strained ICL with cavity length of 1 mm before and after AR coating. The severe degradation of the device was correlated with diffusion of zinc into the active region, which subsequently causes a slow diode turn-on after AR coating as seen in the current-voltage curve of Fig. 5.18. Moreover, this combination failed the tape test that was done on the calibration sample indicating a poor adhesion of this dielectric layers to the substrate.

Comparing this results to the YF_3-ZnS double layer AR coating, where YF_3 was as the first deposited dielectric, suggest that this layer has served as a barrier preventing the diffusion of zinc into the active region, thereby preserving the sharp turn on of the laser diode. Therefore, this finding inspired the idea of preventing the laser degradation due to zinc diffusion by adding an intervening layer between ZnS and the substrate. Since any dielectric layer will add to the number of reflections in the coating, its presence can only be neglected if it is optically thin. Among the materials used in the anti-reflection coatings Ta_2O_5 showed superior adhesion quality and therefore, was used to remedy the adhesion

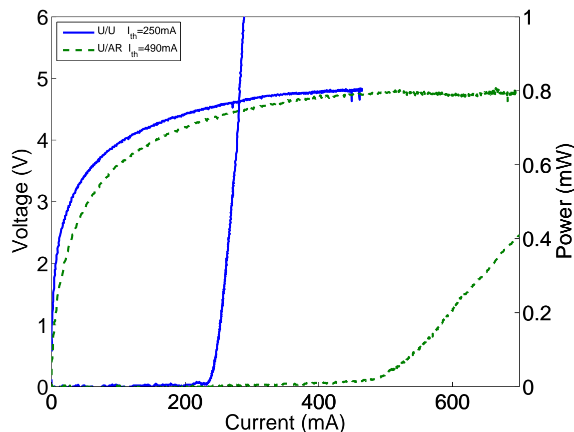

Figure 5.18: $ZnS-YF_3$ double layer AR coating for δ-strained ICL with cavity length of 1 mm.

of ZnS as well as its diffusion. Several experiments showed that a 10 nm layer of Ta_2O_5 is not enough to achieve an acceptable level of adhesion as qualified by the tape test and at least 20-30 nm should be deposited prior to evaporation of ZnS.

Subsequently, a $ZnS-YF_3$ double layer coating was designed and applied to δ-strained ICL at $\lambda = 3.4$ μm with cavity length of 2 mm. The measurement of light-current measurement before and after coating showed a slope efficiency improvement of 1.5 times, as shown in Fig. 5.19.

Thus, the YF_3-ZnS thin film coating shows potential for Mid-IR application both in High-Low and Low-High combinations.

Another material combination considered for double layer AR coating was TiO_2-SiO_2. Since titanium possesses excellent adhesion property, the use of Ta_2O_5 was not required for this combination. Figure 5.20 illustrates a 5-cascade ICL at $\lambda = 3.5$ μm and cavity length of 1 mm before and after a double layer TiO_2-SiO_2AR coating. The coating improved the laser slope efficiency by a factor of 1.47.

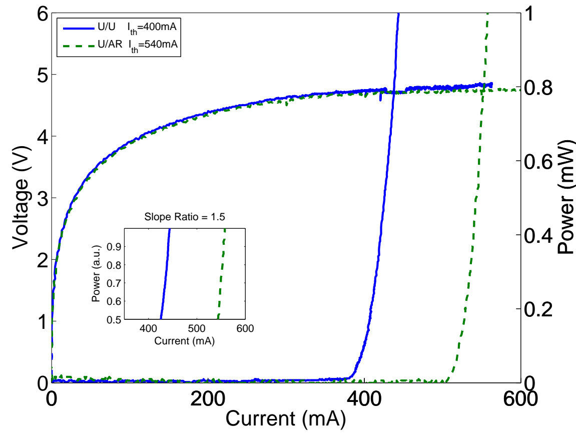

Figure 5.19: ZnS-YF_3 double layer AR coating applied to a δ-strained ICL with cavity length of 2 mm and a Ta_2O_5 adhesion layer of 20nm.

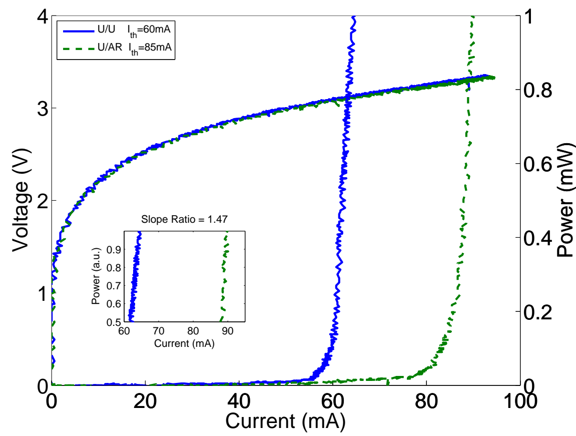

Figure 5.20: TiO_2-SiO_2 double layer AR coating for 5-cascade ICL at $\lambda = 3.5$ μm with cavity length of 1mm

The final AR coating combination that was applied to the interband cascade lasers was the ZnS-SiO_2 double layer. As it was the case with ZnS-YF_3 combination, a 20-30 nm of Ta_2O_5 is required for proper adhesion and for blocking the Zn diffusion.

Figure 5.21 shows the result of a double layer ZnS-SiO_2 that was applied to a 5-cascade ICL with at $\lambda = 3.8\ \mu m$. This combination resulted in improvement of slope efficiency by a factor of 1.95.

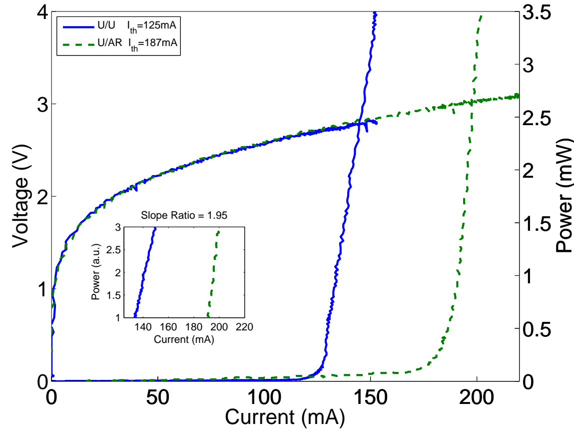

Figure 5.21: ZnS-SiO_2 double layer AR coating for 5 cascade ICL at $\lambda = 3.8\mu m$ with cavity length of 1mm and a Ta_2O_5adhesion layer of 20nm.

The performance of this AR coating is superior to the other combination that were studied. The results of the reflectivity analysis, to be explained in the next section, show that this coating approached the closest reflectivity to 1%. Therefore, when combined with high reflectivity coating, this combination can result in considerable improvement in an interband cascade laser output power. Subsequently, very low reflectivity double layer ZnS-SiO_2 coating was designed and applied to a 1 mm ICL at $\lambda = 3.5\mu$m.

The improvement of the slope efficiency shown in Fig. 5.22 is less than the case where a moderately low reflectivity was targeted. In the following section this behavior will be investigated.

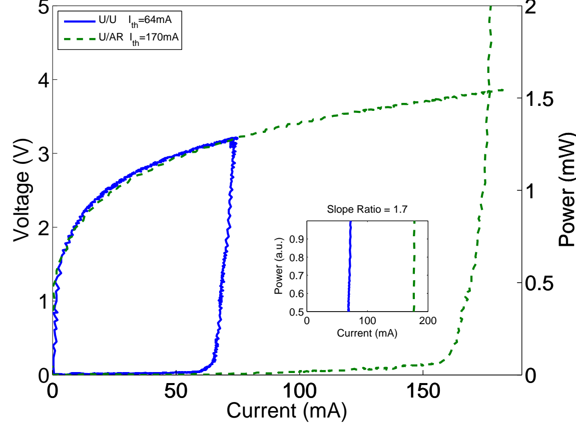

Figure 5.22: ZnS-SiO$_2$ double layer AR coating for 5 cascade ICL at $\lambda = 3.5\mu m$ with cavity length of 1mm and a Ta$_2$O$_5$adhesion layer of 20nm.

5.6 Anti-Reflection Coating and Measurement of Reflectivity

The reflectance of the applied AR coating can be extracted from the changes in the threshold current before and after the coating. Assuming a linear dependence for the threshold current density on gain [17], J_{th} of a laser will depend on mirror loss according to Eq. 4.7, repeated here for convenience,

$$J_{th} = J_t + \frac{\alpha_m + \alpha_i}{\Gamma \frac{dg}{dJ}} \tag{5.37}$$

where J_t is the transparency current density α_i is the internal loss of the waveguide, α_m is the mirror loss, Γ is the optical confinement factor and $\frac{dg}{dJ}$ is the differential gain per unit current density at transparency. Assuming that J_t is negligible compared to $\alpha_i/\Gamma\frac{dg}{dJ}$ [3], Eq. 5.37 can then be approximated as

$$J_{th} = \frac{\alpha_m + \alpha_i}{\Gamma \frac{dg}{dJ}} = \frac{1}{\Gamma \frac{dg}{dJ}} \left(\alpha_i + \frac{1}{2L} \ln \frac{1}{R_f R_b} \right) \tag{5.38}$$

The AR coating reflectivity can then be extracted by comparing the threshold current before and after the coating

$$\frac{J_{th,A}}{J_{th,B}} = \frac{\alpha_{m,A} + \alpha_i}{\alpha_{m,B} + \alpha_i} \tag{5.39}$$

where the subscript A and B refer to the parameter values after and before the coating is applied. In order to extract $\alpha_{m,A}$, the value of α_i is required. Thus, two separate experiments must be conducted to extract the reflectivity of the coatings. One is a cavity length analysis to extract α_i using multiple lengths as described in section 4.2 and, second, comparing the threshold current densities before and after coating. Another way of extracting the coating performance is through the ratio of the output power from the two laser facets that is usually denoted by β and defined as

$$\beta \equiv \frac{F_f}{F_b} = \frac{1 - R_f}{1 - R_b} \sqrt{\frac{R_f}{R_b}}. \tag{5.40}$$

Using Eq. 5.40 requires access to both facets of the laser but is independent of the internal parameters of a particular laser diode. Since the dielectric coatings are often deposited at elevated temperatures in order to promote the formation of a denser and higher quality film, they need to be mounted on a thermally conductive fixture, which often limits access to one of the facets and prohibits the use of Eq. 5.40. Therefore, Eq. 5.39 together with internal parameters extracted from device characterizations were used to evaluate the coatings.

The current-voltage-light (IVL) characteristics were measured before and after the coat-

Table 5.2: Summary of AR coating experiments

AR coating material combination	ICL Material	L [cm]	α_i[cm^{-1}]	$I_{th,A}/I_{th,B}$	$R_{f,A}$	Target Reflectivity
Al_2O_3	ICL-1	0.1	5.8	1.25	0.12	0.05
YF_3-ZnS	ICL-3	0.1	6.4	1.48	0.05	0.01
(Ta_2O_5)ZnS-YF_3	ICL-3	0.2	6.4	1.35	0.05	0.01
TiO_2-SiO_2	ICL-1	0.1	5.8	1.41	0.06	0.01
(Ta_2O_5)ZnS-SiO_2	ICL-2	0.3	4.9	1.49	0.02	0.01
(Ta_2O_5)ZnS-SiO_2	ICL-1	0.1	5.8	2.6	7.2E-4	1E-5

ing were applied in the pulse mode with 0.05% duty cycle to avoid self-heating effects. Threshold current and slope efficiency were extracted from the LI characteristics of the lasers.

The reflectivities calculated for the different AR coatings ranges from 0.12 to 7×10^{-4}. Table 5.2 summarizes the ratio of the change in the threshold current before and after anti-reflection coating, the length of the particular device and its internal loss extracted from the length dependent measurement as well as reflectivity of the coating extracted from the change in the threshold current according to Eq. 5.39. The target reflectivity is also reported in the last column of Table 5.2 [68].

The highest improvement of slope efficiency by a factor of 1.95 was achieved by ZnS-SiO_2 double layer AR coating with 2% reflectivity where the threshold current density was

increased by 49%.

5.7 Carrier Leakage in ICLs

Extensive research has been dedicated to the band structure engineering in order to increase the carrier confinement in the active quantum wells of Mid-IR lasers. However, they are still suffering from low characteristic temperatures for the threshold current and more importantly the slope efficiency [3, 17]. These issues have been attributed to alternative non-radiative paths that allow the carriers to escape to higher energy levels resulting in leakage currents. In particular, surface roughness scattering due to large band offsets in the active region that exceed 2 eV, shown in Fig. 2.1, and auger assisted carrier leakage can play a significant role in ICL leakage currents. Another mechanism that could potentially contribute to temperature sensitivity in a cascaded structure is backfilling of the lower laser level by electrons in the injector. However, this mechanism is specific to QCLs and does not play a role in ICL operation [69]. ICL active region optimizations require a significant overlap between electron and hole wave functions [2]. This is in contrast to QCLs where the design focuses mostly on electron wavefunctions. This inherent difference between the two makes active region bandgap engineering more challenging in ICLs [5]. Moreover, ICL has so far been limited to GaSb material systems which limits the material selection for quantum wells and barriers, again restricting the flexibility of the bandgap engineering.

High power operation can be achieved by increasing the number of cascades, and/or the active area through modifying the physical dimensions of the waveguides. These strategies, however, increase the self-heating of the device in CW operation. Facet coating is another approach to enhance the output power by increasing the differential efficiency. In order

to achieve higher performance through optical coating of the laser facets, the effect of the mirror reflectivity on the internal characteristics of the devices needs to be carefully examined. Anti-reflection coatings in essence increase the waveguides loss and, therefore, results in a higher threshold current. This phenomenon, consequently, raises the carrier density of the laser and could potentially lead to even higher leakage current. A higher leakage reduces the internal quantum efficiency, thereby, possibly counter-balancing the positive effect of the increased mirror loss in enhancing the external slope efficiency. In fact, it has been observed for quantum cascade lasers that the slope efficiency actually decreases for low reflectivity AR coatings compared to uncoated devices [70]. Thus, optimal AR coatings need to be designed for power enhancement in IC lasers. In this section, different levels of AR coatings with reflectvities ranging from 0.15 to 7×10^{-4} are applied to ICLs and the device performance in terms of increase in threshold current, leakage current and slope efficiency are studies. The leakage current is extracted and its dependence on increased carrier concentration is assessed. The wide range of AR coating reflectivities accessible through *in-situ* monitoring of the dielectric thickness allowed for the study of the effect of carrier leakage in ICLs. These are the first experimental results on this subject. These results provide an understanding of how the leakage current increases with carrier concentration within the active region and offers a method for optimizing the AR coatings and maximizing the slope efficiency in ICLs.

5.7.1 Extraction of Leakage Current

Here, single- and multi-layer AR coatings that were applied to ridge waveguide ICLs covering a wide range of reflectivities have been analyzed to investigate the dependance of internal laser parameters on mirror loss and carrier concentration. These results include Al_2O_3 single layer AR coating and ZnS-YF_3, ZnS-SiO_2 and TiO_2-SiO_2, double layer AR

Table 5.3: Internal loss, wavelength of emission and cavity length dependence of threshold current for the ICLs that have been used in this study

ICL Material	**Threshold Current Density [A/cm^2] vs. inverse cavity length [cm^{-1}]**	$\alpha_{\mathbf{i}}$[cm^{-1}]	λ[μm]
ICL-1	$J_{th} = 34.90L^{-1} + 208.9$	5.8	3.5
ICL-2	$J_{th} = 43.26L^{-1} + 221.3$	4.9	3.8
ICL-3	$J_{th} = 122.9L^{-1} + 816.2$	6.4	3.4

coatings with reflectance ranging from 0.15 to 7×10^{-4} as summarized in Table 5.2. The refractive indices of these materials were measured and the coatings have been designed for the specific ICL wavelength and fabricated using the methodology described in previous sections.

The J_{th} and L^{-1} relation for all ICL samples used in this study as well as the internal loss and the emission wavelengths are summarized in Table. 5.3. The differential quantum efficiency is related to the facet reflectivity via

$$\eta_d = F_f \eta_i N \frac{\alpha_m}{\alpha_m + \alpha_i} \tag{5.41}$$

where η_i is the differential internal efficiency per stage, N is the number of stages which is equal to 5 in this case, and F_f is the fraction of total output power delivered from the front facet, determined by both facet reflectivities and is given by [58]

$$F_f = \frac{1 - R_f}{(1 - R_f) + \sqrt{\frac{R_f}{R_b}}(1 - R_b)} \tag{5.42}$$

The modification of facet reflectivities affects the slope efficiency by changing F_f and α_m. Furthermore, due to the increase in carrier concentration leading to higher leakage current, η_i can also reduce appreciably. The differential internal efficiency is a measure of the fraction of the total current above the threshold that results in carrier generation in the active region. By using a four-level system, Botez et al. [69,71] expressed η_i in terms of the differential pumping efficiency η_p and the laser transition differential efficiency η_{tr} [54] as

$$\eta_i = \eta_{tr}\eta_p = \eta_{tr}\left(1 - \frac{J_{leak,th}}{J_{th}}\right) \tag{5.43}$$

where $J_{leak,th}$ is the leakage current density and J_{th} is the threshold current density.

It is this leakage current which is attributed to the high temperature sensitivity of the threshold current density and slope efficiency of ICLs. The low characteristic temperature of the threshold current and the slope efficiency, T_0 and T_1, respectively, indicate a sizable contribution from the carrier leakage. As described in section 4.8, T_1 and T_0 are estimated to be around 90 K and 38 K, respectively.

The same leakage current can also play an important role in the case of AR coated devices. Due to a considerable increase in the threshold current density, particularly at very low reflectivity, the threshold carrier density before and after coating changes dramatically which in turn affects the internal device parameters. Leakage current can then be extracted from the changes in the slope efficiency.

Though the leakage current did not explicitly appear in Eq. 5.37 for threshold current, it can be easily shown that it is indeed part of the threshold current density. Using $J = (q/\eta_i' \tau)n$, where n is the carrier concentration and η_i' is the internal efficiency, Eq. 5.37 becomes

$$J_{th} = \frac{q}{\eta_i' \tau}\left[n_t + \frac{\alpha_m + \alpha_i}{\Gamma \frac{dg}{dJ}}\right]. \tag{5.44}$$

Substituting the value of $\eta_i' = \eta_{inj}\eta_p \approx \eta_p$ in Eq. 5.44, where η_{inj} is the carrier injection efficiency, gives

$$J_{th} = \frac{q}{\tau}\left[n_t + \frac{\alpha_m + \alpha_i}{\Gamma \frac{dg}{dJ}}\right] + J_{leak}. \tag{5.45}$$

Thus, the linear approximation of gain to threshold current density in Eq. 5.37 accounts for the leakage current within its formulation.

Using Eq. 5.41, the change in the differential quantum efficiency is related to the internal laser parameters by

$$\frac{\eta_{d,A}}{\eta_{d,B}} = \frac{F_{f,A}\eta_{p,A}\frac{\alpha_{m,A}}{\alpha_{m,A}+\alpha_i}}{F_{f,B}\eta_{p,B}\frac{\alpha_{m,B}}{\alpha_{m,B}+\alpha_i}}. \tag{5.46}$$

where F_f, α_m, are obtained from the reflectivity in Table 5.2. A and B subscripts correspond to values after and before coatings, respectively. The ratio of differential pumping efficiency after and before the AR coatings, $\eta_{p,A}/\eta_{p,B}$, is calculated from Eq. 5.46. In this calculation, it is assumed that the laser transition differential efficiency η_{tr} does not change in the process. The laser transition differential efficiency is not temperature dependent and

is not expected to change with AR coatings significantly.

In order to obtain the value of the leakage current, the absolute value of the uncoated laser internal differential efficiency is required. η_i was calculated using the calibrated slope efficiency as described in section 4.8 with a measured value of 31.6% which is mainly limited by the leakage current. Using the initial value of internal efficiency for the uncoated device and the change of the internal efficiency obtained from Eq. 5.46, the final η_i after coating is calculated. The threshold current densities before and after the coating are then inserted in Eq. 5.43 to obtain the leakage current with the additional assumption that the η_{tr} is unity. Here, it is important to note that the initial value of η_i and the contribution from the transition efficiency will solely effects the ratio of the leakage current to threshold current before and after the application of AR coating. The ratio of the internal efficiency and subsequent optimization of anti-reflection coating is independent of these assumptions. The extracted values of the ratio of the differential efficiencies; internal differential efficiencies and leakage currents after and before are summarized in Table 5.4 [68].

5.7.2 Discussion

As seen from the Table IV, the ratio of the differential efficiency before and after coating increases with reduced facet reflectivity up to 2% (as is expected) but then decreases for the lowest reflectivity of 7×10^{-4}. Similar results have been previously seen in AR coatings on QCLs where the slope efficiency decreased at very low reflectivity [60, 70]. The reason for this trend lies in the change of the internal efficiency as seen from the data in Table 5.4. The degradation in the differential internal efficiency, η_i, before and after coating worsens as the reflectivity of the facet reduces. The improvement of the differential efficiency resulting from lowering the mirror loss compensates only part of the degradation of internal

Table 5.4: summary of the extracted reflectivities, the ratio of slope efficiency, internal differential efficiency, threshold current and leakage current after and before the AR coating is applied [68]

AR coating material combination	$\mathbf{R_{f,A}}$	**L [cm]**	$\frac{\eta_{d,A}}{\eta_{d,B}}$	$\frac{\eta_{i,A}}{\eta_{i,B}}$	$\frac{I_{th,A}}{I_{th,B}}$	$\frac{I_{leak,A}}{I_{leak,B}}$	$\frac{I_{leak,A}}{I_{th,A}} / \frac{I_{leak,B}}{I_{th,B}}$
Al_2O_3	0.12	0.1	1.33	0.91	1.25	0.72	1.03
YF_3-ZnS	0.05	0.1	1.5	0.83	1.48	0.74	1.07
(Ta_2O_5)ZnS-YF_3	0.05	0.2	1.5	0.76	1.35	0.76	1.10
TiO_2-SiO_2	0.06	0.1	1.47	0.85	1.41	0.73	1.06
(Ta_2O_5)ZnS-SiO_2	0.02	0.3	1.95	0.81	1.49	0.75	1.08
(Ta_2O_5)ZnS-SiO_2	7.2E-4	0.1	1.7	0.67	2.6	0.79	1.17

efficiency caused by the increased carrier concentration. The relationship between the ratios of the internal efficiency after and before coating as a function of the reflectivity of the facet is plotted in Fig. 5.23. The internal efficiency ratio changes logarithmically with reducing the facet reflectivity indicating a more drastic change for ultra-low reflectivities. The decrease in the internal differential efficiency results from a substantial increase in the leakage current as larger proportions of the carriers are leaking at lower reflectivity as compared to the uncoated device. The results also show how the leakage current increases as the carrier concentration increases in the active region. The initial value of internal efficiency is required to calculate the ratio of leakage current to the threshold current and its change with the mirror loss. For an internal efficiency of 31.6% and laser transition efficiency of unity, the leakage to threshold current ratio increased by as much as 17% by increasing the mirror with low reflectivity AR coated samples. However, the trend

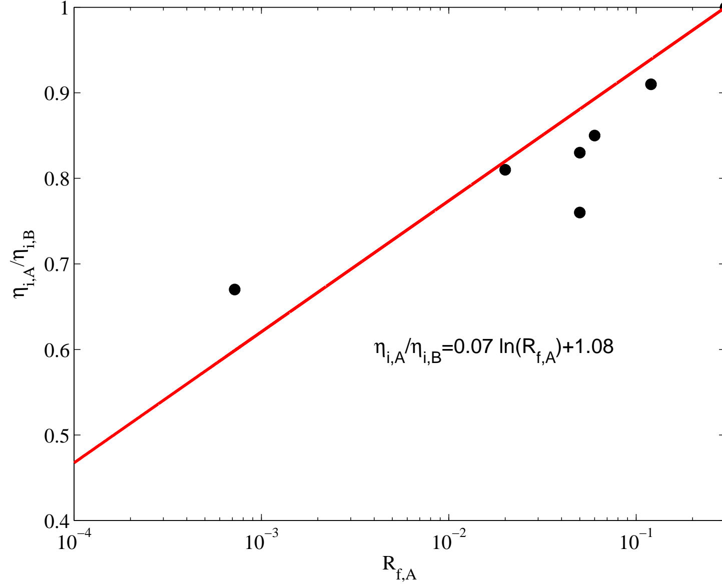

Figure 5.23: The ratio of internal differential efficiency after and before the coatings ($\eta_{i,A}/\eta_{i,B}$) as the facet reflectivity is changed.

of increase in the leakage current and the ratio of the internal efficiency are of greater importance. This leakage current is attributed to the thermal excitation of the injected electrons to higher energy levels in the active region. Electrons in these higher energy levels can either relax to lower energy levels or escape to continuum. The barrier height in the active and injection region play an essential role in determining the leakage current in ICLs.

These results suggests that the optimization procedure for designing the anti-reflection coatings for achieving the highest differential efficiency must take into account the introduction of additional leakage in the device. For high power applications where maximum differential efficiency is required, very low reflectivities can be counterproductive as they result in substantial increase in the leakage current and degrade the device performance. The increase in the leakage current would in turn decrease the differential efficiency resulting

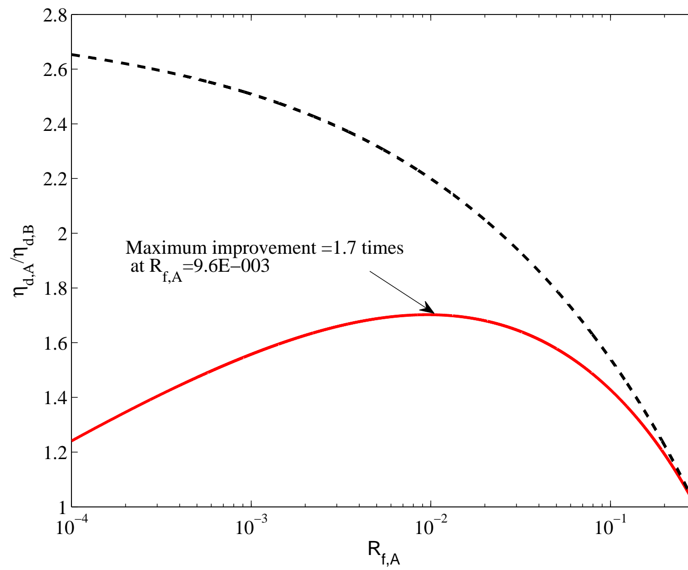

Figure 5.24: Ratio of differential quantum efficiencies vs. Reflectivity considering the decrease in the internal differential efficiency (Solid line). Slope efficiency vs. reflectivity is also plotted for constant internal differential efficiency (dashed-line) for comparison.

in a less efficient device. In order to visualize such dependencies, the ratio slope efficiency was calculated for a 1 mm device with internal loss of 6 cm^{-1}, using the fitted logarithmic function for internal efficiency. For comparison, the ratio of the slope efficiency was also calculated for the same device assuming a constant internal efficiency. The results for both scenarios are plotted in Fig. 5.24. As it can be seen from this plot, the slope efficiency improves at first by lowering the reflectivity but starts to decrease as the reflectivity is further lowered. For this particular case, the maximum slope efficiency improvement is 1.7 times and is obtained at a front facet reflectivity of $\sim$1%. It should be noted that this value changes for different device lengths and also depends on the internal loss. High reflectivity coating of the back facet is also recommended and would allow for higher improvement with lower reflectivities [68].

5.8 Conclusions

In conclusion, in this chapter several dielectric materials were considered for the mid-IR anti-reflection coatings and were experimentally evaluated through single and multi-layer coating designs. These materials were optically characterised and the fabrication conditions were optimized to yield the best coating. ZnS, YF_3, SiO_2, TiO_2, and Al_2O_3 were selected from the initial list as the most promising candidates. AR coating were designed and applied to several. The change of threshold current and slope efficiencies were followed to characterise the coating and investigate the change in internal laser parameters resulting from the coating application. It was shown how the leakage current increases with carrier concentration in the active region and the resulting reduction of the internal efficiencies limits the improvement of the slope efficiency with AR coatings. While the reduction of the front facet reflectivity allows for higher output power, the cost of increasing the

carrier density has to be accounted for in order to find the optimum balance. If other laser parameters are also affected, for example if the internal loss increases as a result of the increase in carrier density, there could be a further reduction of the slope efficiency after a certain point in lowering the facet reflectivity. These changes are expected to be small compared to the effective loss associated with carrier leakage. Based on our previous findings and similar works on Mid-IR QCL, the relatively low characteristic temperature of the threshold current density and the slope efficiency in the semiconductor lasing materials are linked to carrier leakage from the active quantum wells. The results of the anti-reflection coating also indicate the sensitivity of these devices to the number of carriers in the active region. Better carrier confinement in QCLs through application of high barriers and tapered injectors [69, 72] has led to substantial improvement in QCL performance at room and high temperatures. Future work should focus on implementing similar ideas for ICLs to improve their performance and stability. A substantial improvement in the wall-plug efficiency and in the amount of power that can be extracted from ICL lasers is expected by appreciably reducing the carrier leakage in these types of lasers.

Chapter 6

Mid-IR Subwavelength Lasers

6.1 Introduction

The size mismatch between electronic and photonic devices is mainly due to the fundamental difference between the wavelength of electrons and infrared photons. Material selection and fabrication techniques can reduce this gap significantly, analogous to the way a silicon nano-wire replaces an optical fiber in on-chip optical communication applications and brings down the waveguide diameter to the nanometer scale [73]. The coherent light sources are no exception to this miniaturization demand. Additionally, devices with smaller dimensions allow for high density integration, require less power, and enable high speed switching [74]. Vertical cavity surface emitting lasers (VCSELs) [75], photonic crystals (PCs) [76], micro-disk lasers, [77] exemplify devices that operate with much lower mode volumes compared to conventional semiconductor lasers. However, the overall structure size remained significantly larger than the laser wavelength at least in one of the dimensions for all these cases [73].

In 1946, Purcell proposed that in subwavelength cavities, spontaneous emission rate will increase and the relaxation lifetime will decrease when the spontaneous emission is coupled to a single cavity mode [78]. This phenomenon is the main idea behind a thresholdless laser, first proposed by Kobayashi et al. [79] [80]. Therefore for a thresholdless laser, the loss due to coupling of spontaneous emission to free space modes is eliminated through application of subwavelength cavities with sparse modal content. [80].

The first step in pursuit of a truely subwavelength laser was the study of metal loss compensation by semiconductor gain media [81] [82] and subsequent proposals for possible laser structures [83]. However, it was generally believed that the only candidate for small lasers are the dielectric cavities with a low loss and it was not clear that the metal losses can be overcome by semiconductor gain materials [84]. The first demonstration of lasing in metallic-coated nano cavities, reported in 2007 [85], was a paradigm shift in laser miniaturization, resulting in replacement of dielectric cavities with metallic ones altogether [86]. This electrically pumped nano-laser consisted of a semiconductor heterostructure pilar coated with SiN and covered by gold with a final outer diameter of 260 nm and height of 300 nm. Lasing was observed at 77 K and 1.44 μm and light was collected through the substrate. This cavity and similar structures rely on dielectric modes and are, therefore, diffraction limited in all three dimensions.

In 2009, lasing in metal-insulator-metal subwavelength waveguides was demonstrated in near-IR at 78 K with electrical injection [87]. The rectangular cavities were chosen to permit independent size reduction in different dimensions. The waveguide width in this study was varied from 90 nm to 350 nm with the smallest width equivalent to the optical thickness of $\lambda/4$, far below the diffraction limit, owning to the plasmonic nature of the

MIM structure. RT pulsed operation was also observed in wider devices. In the years that followed, there have been numerous demonstrations of subwavelength lasers. In the metallodielectric lasers by Nehzad et. al., bulk InGaAsP gain medium was covered by SiO_2 and aluminium to form cylindrical cavities with 450 nm (0.32λ) diameter supporting purely dielectric modes. Pulsed operation at RT was observed at $\lambda = 1.43$ μm [81]. Thresholdless lasing has also been demonstrated at 4.5 K and near infrared wavelength from a coaxial cavity based on traveling surface plasmon polaritons (SPPs) with InGaAsP QW gain medium [88].

The idea of spacer (Surface Plasmon Amplification by Stimulated Emission of Radiation) is behind the smallest nano-laser reported to date. Spasers rely on localized SPP modes and can surpass the diffraction limit in all three dimensions. The first spacer proposed by Bergman et al., [89] consisted of gold nano particles covered with dye molecules with an overall diameter of 44 nm ($\lambda/12$) and lasing at 531 nm which is the surface plasmon resonance of gold nano-particles [90].

Even though, RT operation is required for on-chip applications of nano-lasers, the first demonstrations are realized at low temperature. This is because of high semiconductor gain and low metal loss at cryogenic temperatures. This has been the case for most of the semiconductor laser technology [91]. It is worth noting that the last three nano-lasers that were mentioned previously are all optically pumped. Real applications, however, require RT CW operation of electrically pumped devices. Metallic cavities do provide a certain advantage in this regard. Encapsulating the gain medium in a metallic shell allow for the electrical connections to be integrated with the laser in contrast to conventional semiconductors, where the connections were usually separated by intermediate cladding layers to

avoid high losses [91]. In addition to facilitating the electrical connections, metals can serve as efficient heat-sinks due to their high thermal conductivities.

Another advantage of metallic nano-cavities is that varying the emission wavelength is readily controlled during the device fabrication. The dimensions of the cavity is what ultimately defines the resonant mode and by adjusting these dimensions, the wavelength can be positioned anywhere within the gain window of the active material [91]. The digital tunability of nano-lasers allows for selection of emission wavelength during design and fabrication. This tunability is experimentally demonstrated in electrically pumped metallic nano-pillars, where wavelength versus diameter with a slope of 2.7 was achieved [92].

Among different proposed cavity shapes, circular cavities can generate azimuthal polarization [92,93], with possible applications in atom trapping [94], imaging, [95] and subwavelength scanning [96]. As mentioned earlier selecting the desired mode with the required polarization can easily be achieved in nano-cavities by adjusting the cavity dimensions. Nevertheless, due to the emission of light from a subwavelength aperture, nano-lasers usually suffer from highly diverging beams [92]. Slight modifications to circular cavities can improve divergence, e.g. implementation of a horn antenna in the lower part of the cavity, as suggested by Hill and Marell in 2011 [97]. In this scheme, the cavity parameters, such as confinement and quality factors, can be designed independently from the beam shaping antenna [97] and tapering the pilar can be realized by implementing the proper etching techniques [98].

Even though subwavelength cavities have been demonstrated in telecom wavelengths, there are still challenges associated with their relatively high threshold gain requirements.

Due to the longer wavelengths of mid-IR, compared to the telecommunication lasers, the cavity can have a larger gain medium without compromising its subwavelength character. A larger gain volume translates into a lower carrier density which, in turn, relaxes the temperature constraints. The lower metal loss in the infrared region is also advantageous in reducing the cavity loss. Moreover, the large volume of the gain medium means an improved fabrication tolerance. The roughness of the sidewalls that contributes to non-radiative recombination are a smaller fraction of the total volume in the mid-IR range. Nano-laser cavities with azimuthal polarization may be arranged in arrays for high resolution imaging in infrared [96].

Miniature mid-IR lasers can be used in a verity of applications for on-chip sensing and optical communications. To our knowledge there has been no experimental demonstration of a nano laser in mid-IR to date. This chapter focuses on design and optimization of mid-IR micro cavities based on plasmonic coaxial waveguide structures. Here a systematic design methodology is developed and described that can be applied in mid-IR as well as other wavelength ranges. These structures are particulary interesting for deep subwavelength confinement of mid-IR light. Combined with W-structure QW associated with ICLs plasmonic coaxial microcavities are demonstrated to be capable of providing nano-lasers. The enhanced Purcell factors of these cavities shows great potential for thresholdless operation.

6.2 Surface Plasmon Polaritons (SPP)

Coherent charge oscillations on metal surfaces can support wave propagation at a metal-dielectric interface. These electromagnetic surface waves are tightly confined to the in-

terface boundary and are called surface plasmon polaritons. In order to review the basic properties of surface plasmon polaritons, the first step is to derive the wave equation. For monochromatic radiation in linear and isotropic media, in the absence of external excitations, Maxwell curl equations read,

$$\nabla \times \mathbf{E} = -i\omega\mu\mathbf{H}, \tag{6.1a}$$

$$\nabla \times \mathbf{H} = i\omega\epsilon\mathbf{E}, \tag{6.1b}$$

where $\mathbf{E}$ and $\mathbf{H}$ are the electric and magnetic field vectors, respectively, and μ and ϵ are the permeability and permittivity of the medium, respectively. As shown in Fig. 6.1, for propagation along the z axis, due to homogeneity in the y and z direction, both electric and magnetic fields are simplified to

$$\mathbf{E}(x, z, t) = \mathbf{E}(x)\exp(-i\omega t + i\beta z), \tag{6.2a}$$

$$\mathbf{H}(x, z, t) = \mathbf{H}(x)\exp(-i\omega t + i\beta z), \tag{6.2b}$$

where β is the complex propagation constant. Inserting Eq. 6.2 in 6.1 results in the Helmholtz wave equations, *i.e.*

$$\frac{d^2\mathbf{E}(x)}{dx^2} - k_x^2\mathbf{E}(x) = 0, \tag{6.3a}$$

$$\frac{d^2\mathbf{H}(x)}{dx^2} - k_x^2\mathbf{H}(x) = 0. \tag{6.3b}$$

where

$$k_x^2 = \beta^2 - \omega^2\mu\epsilon. \tag{6.4}$$

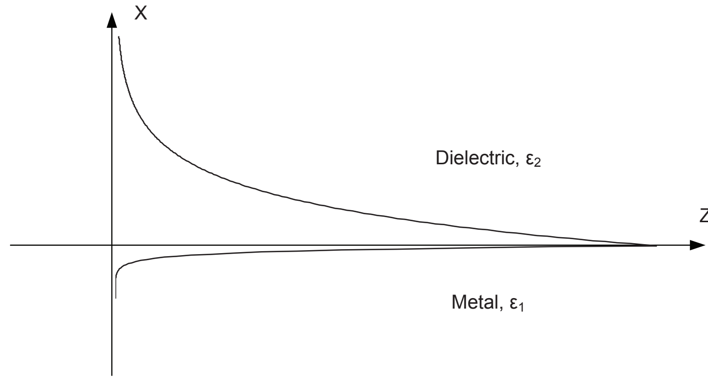

Figure 6.1: Transverse field profile of a surface plasmon polariton along a meta-dielectric interface.

Equations 6.3 and 6.1 hold in both half spaces. For TM waves, with non-vanishing field components H_y, E_x, and E_z, 6.3b results in

$$H_y(x) = C_i \exp(-k_{x,i}x) \tag{6.5}$$

where C_i and $k_{x,i}$ refer to the amplitude and decay constant in the media with relative dielectric permittivity of $\epsilon_{r,i}$ for $i = 1, 2$.

Substituting 6.5 in 6.1, returns [99]

$$E_x(x) = \frac{\beta}{\epsilon_0 \epsilon_{r,i}\ \omega} H_y = C_i \frac{\beta}{\epsilon_0 \epsilon_{r,i}\ \omega} \exp(-k_{x,i}x), \tag{6.6a}$$

$$E_z(x) = sgn(x) \frac{ik_{x,i}}{\epsilon_0 \epsilon_{r,i}\ \omega} H_y = sgn(x) C_i \frac{ik_{x,i}}{\epsilon_0 \epsilon_{r,i}\ \omega} \exp(-k_{x,i}x). \tag{6.6b}$$

Assuming the metal is the lower half space with $x < 0$ and dielectric is the upper half space with $x > 0$, as shown in Fig. 6.1, and using the boundary conditions, *i.e.* continuity

of the tangential field component H_y and E_z, requires that $C_1 = C_2$ and

$$\frac{k_{x,1}}{\epsilon_{r,1}} = \frac{k_{x,2}}{\epsilon_{r,2}} \tag{6.7}$$

Therefore, the propagation constant in the z direction follows

$$\beta = k_0\sqrt{\frac{\epsilon_{r,1}\epsilon_{r,2}}{\epsilon_{r,1}+\epsilon_{r,2}}}. \tag{6.8}$$

Equation 6.8 is is often referred to as the dispersion relation for SPPs.

Using the same technique for TE waves, with non-vanishing field components E_y, H_x, and H_z, 6.3a yields

$$C(k_{x,1}+k_{x,2}) = 0. \tag{6.9}$$

Since a confined mode requires that $k_{x,1} < 0$ and $k_{x,2} > 0$,the condition 6.9 is satisfied only when $C = 0$. This is an important conclusion as it shows that SPPs are only supported by parallel or TM polarization, where the magnetic field is parallel to the dielectric-metal boundary. It can be seen from Eq. 6.9 that this is a direct consequence of opposite signs of permittivity at the interface.

The complex refractive index of metals is described using the Drude dielectric function,

$$\tilde{n}^2 = \epsilon = 1 - \frac{\omega_p^2}{\omega^2 + i\gamma\omega} \tag{6.10}$$

where ω_p is the plasma frequency, and γ is the damping coefficient. It is worth noting that the plasma frequency is given by $\omega_p = \frac{ne^2}{\epsilon_0 m}$, where n is the electron density, e is the electron charge, and m is the effective mass of electrons in the metal band structure. The damping coefficient $\gamma = 1/\tau$, where τ is the relaxation time of the free electrons. Together they

relate the macroscopic behaviour of metals to the lattice potential and electron interactions and is called the plasma model.

Figure 6.2 shows the real and imaginary parts of silver refractive index reported in the literature for λ from 0.206 to 12.40 μm [Babar and Weaver 2015 [6]], and from 0.188 to 1.937μm [Johnson and Christy 1972 [7]], and the fitted curves using the extended Drude model dielectric function [100]

$$\epsilon = \epsilon_\infty - \frac{\omega_p^2}{\omega^2 + i\gamma\omega} \tag{6.11}$$

where $\omega_p = 1.4 \times 10^{16}[rad/s^{-1}]$, $\gamma = 2.6 \times 10^{13}[rad/s^{-1}]$, and $\epsilon_\infty = 5$. ϵ_∞ in the extended Drude model accounts for the deviation of metal from free electron gas model in frequencies close to ω_p.

In the absence of damping, $\gamma = 0$, metal permittivity can be simplified to $\epsilon = 1 - \omega_p^2/\omega^2$. Using the simplified dielectric function for the metal in the SPP dispersion relation Eq. 6.8, it can be shown that $\epsilon_1 + \epsilon_2 = 0$ for $\omega_{sp} = \omega_p/\sqrt{1+\epsilon_2}$. ω_{sp} is the surface plasmon frequency. The plasma frequency and surface plasmon frequency divide the frequency domain into three regions as shown in Fig. 6.3.

- $\omega_p < \omega$

  In this region $\epsilon_1 > 0$ and metal behaves like a dielectric. It should be noted that the validity of Drude model at high frequencies is limited to frequencies below the interband transition of metals.

- $\omega_{sp} < \omega < \omega_p$

  where $\epsilon_1 < 0$ and $\epsilon_1 + \epsilon_2 > 0$. Since $\epsilon_1\epsilon_2 < 0$, in this region β is purely imaginary and, therefore, no propagation is allowed in the frequency range for an ideal metal.

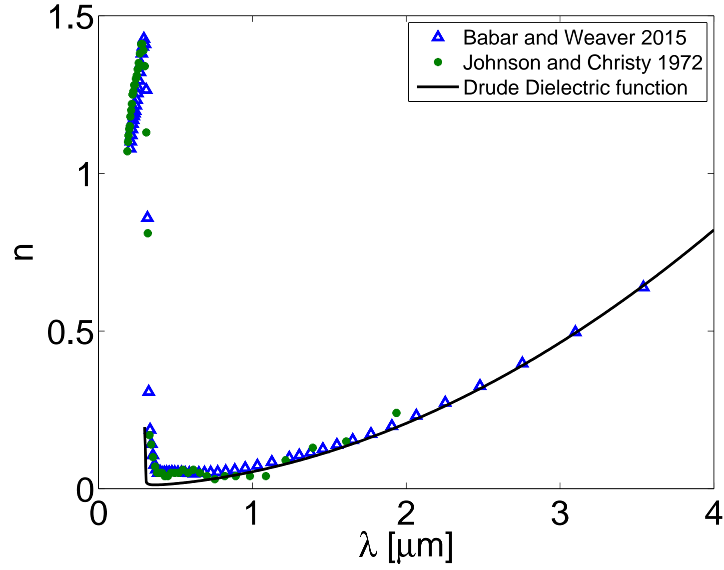

(a)

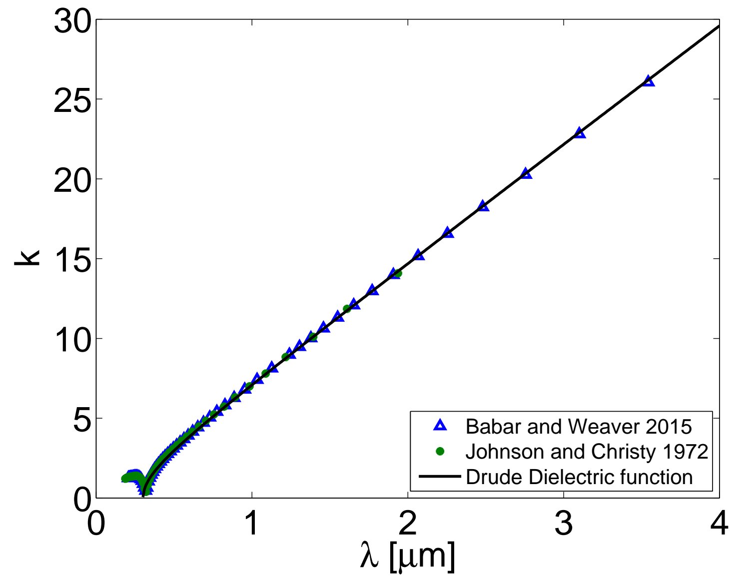

(b)

Figure 6.2: Real and imaginary part of silver refractive index, Babar and Weaver 2015 (triagles) [6], Johnson and Christy 1972 (starts) [7], and fitted curve using the extended Drude model dielectric function with $\omega_p = 1.4 \times 10^{16}[rad/s^{-1}]$, $\gamma = 2.6^{13}[rad/s^{-1}]$, and $\epsilon_\infty = 5$

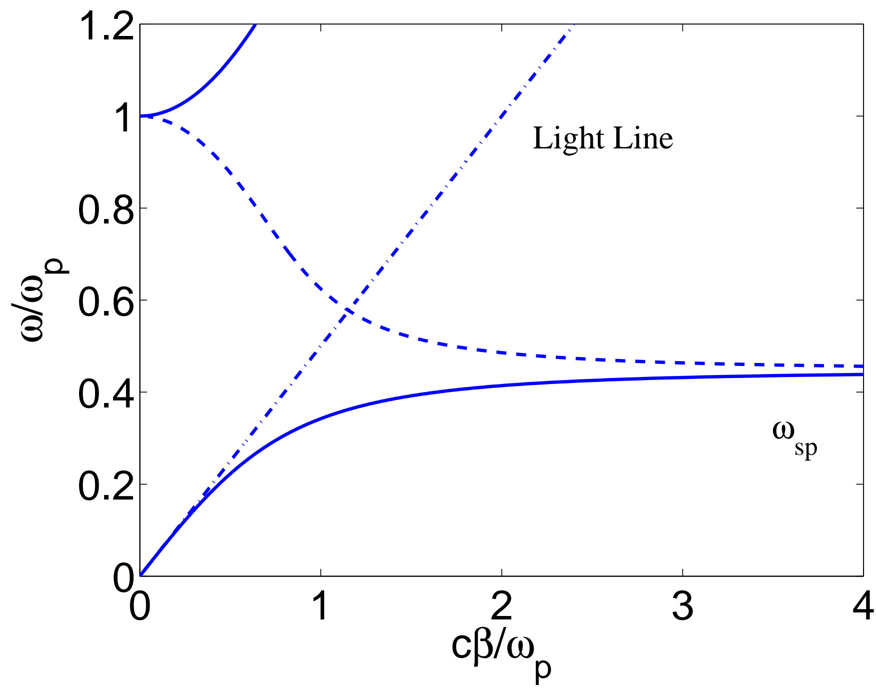

Figure 6.3: Dispersion curve for surface plasmon for an ideal metal. The real (solid line) and imaginary (dashed line) part of the propagation constant β are shown as well as the light line. Frequency and propagation constant are both normalized to the plasma frequency.

- $\omega < \omega_{sp}$

  The propagation constant β varies from close to the light line for very low frequencies to infinity for ω_{sp}. In this region $\epsilon_1 < 0$ and $\epsilon_1 + \epsilon_2 \leq 0$ and the dispersion curve is on the right side of the light line resulting in bound states. For frequencies close to ω_{sp}, in addition to longitudinal confinement, the mode is also confined in the transverse direction according to $k_x = \sqrt{\beta^2 - \omega^2 \mu \epsilon}$. The modes close to the light line are loosely confined with lower propagation loss.

In the case of real metals $\gamma \neq 0$ and, therefore, $\epsilon_1 + \epsilon_2$ never goes to zero. This effectively means that the propagation constant does not go to infinity and always has a real part allowing for quasi bound propagation in $\omega_{sp} < \omega < \omega_p$ frequency range. In practice $\gamma \ll \omega_p$ even at room temperature and, therefore, confinement well below diffraction limit in the dielectric can be achieved using SPP. However, there is a trade-off between the propagation loss and confinement as highly confined modes suffer from larger loss in the z direction.

6.3 Metallic Optical Resonators

Metallic cavities enable the utilization of highly confined modes that are essential for laser miniaturization. Reduction of the cavity mode volume below the λ^3 of the resonating mode leads to the emergence of cavity quantum electrodynamics (QED) phenomena, such as spontaneous emission enhancement known as Purcell effect [78]. Moreover, due to the presence of metals, some of the conventional definitions used for laser cavities should be revised to incorporate loss and dispersion. Quantum mechanical treatment of the entire device forms the basis of the development of nano-laser theory, and, in general applies to the entire field.

A resonator is often characterized at the resonant frequency ω_0 with its quality factor,

Q, defined as

$$Q = \omega_0 \frac{\text{Stored Energy}}{\text{Power loss}}. \tag{6.12}$$

For an optical resonators, power loss = $v_g \alpha \times$ Stored Energy, where α is the Beer's law absorption coefficient for the beam intensity propagation through a medium, $I = I_0 \exp(-\alpha x)$, and v_g is the group velocity of the resonator mode $v_g = c_0/n_g$ where n_g is the group index. Therefore,

$$Q = \frac{\omega_0}{v_g \alpha} = \frac{\omega_0}{\delta\omega}, \tag{6.13}$$

where $\delta\omega$ is the linewidth of the resonant mode [101]. Given that photons are lost with a rate of $v_g\alpha$, the quality factor can be rewritten as $Q = \omega_0 \tau_p$, where τ_p is the photon lifetime in the cavity.

In cavities with high number of modes and uniform coupling to free space, the spontaneous emission factor in the rate equations, β_{sp}, is the inverse of the number of modes within the spontaneous emission bandwidth [58]. However, reduction in the number of modes results in the enhancement of this factor and the observation of Purcell effect. The lasing threshold is, thus, lowered as more of the spontaneous emission couples to the lasing mode and β_{sp} will approach unity in the case of a truely thresholdless laser. For example, coaxial nano-laser at 4.5 K with spontaneous emission factor of β_{sp}=0.99 has been demonstrated [88].

The fraction spontaneous that is coupled to the lasing mode is called the spontaneous emission factor β and is related to the Purcell factor F via,

$$\beta = \frac{F\beta_0}{1 - \beta_0 + F\beta_0} \tag{6.14}$$

where β_0 is the bulk spontaneous emission factor without the Purcell enhancement, *i.e.* $F = 1$, and $\beta = \beta_0$, and β approaches 1 when $F \to \infty$ [86]. Therefore, the Purcell factor is a key parameter to quantify the degree of light-matter interaction [102] in a cavity. F depends fundamentally on the level of confinement in the cavity which is determined by two main parameters:

- quality factor Q
- effective mode volume; V_{eff}.

The effective mode volume is defined as [102, 103]

$$V_{\text{eff}} = \frac{\int \epsilon(r)|E(r)|^2 d\mathbf{r}}{\epsilon(r_{\text{max}})|E(r_{\text{max}})|^2} \tag{6.15}$$

where r_{max} is the location of the maximum electric field. The effective volume is usually normalized to and expressed in terms of $(\lambda/2n)^3$. By applying the Fermi's golden rule, the Purcell factor is obtained as the ratio of spontaneous emission rate in the presence of the cavity with respect to bulk and is expressed in terms of cavity parameters [102],

$$F = \frac{6Q(\lambda/2n)^3}{\pi^2 V_{\text{eff}}}. \tag{6.16}$$

where n is the index of refraction at the location of maximum field. As seen from Eq. 6.16, there are two mechanisms that increase the coupling of the spontaneous emission factor to the lasing mode. First, increasing the cavity quality factor, *i.e.*, decreasing the linewidth of the lasing mode, and, second, is the reduction of the effective mode volume.

For metallic cavities, in general, Q is usually low due to metal loss. However, plasmonic cavities excel at reducing the effective mode volume through highly confined fields

in transverse directions. In contrast, laser waveguide consists of dielectric cavities with weakly guided modes, which, in turn, allows for plane wave approximation of electromagnetic fields.

The weekly guided modes and the dielectric nature of conventional Fabry-Pérot lasers has led to the commonly used power confinement factor,

$$\Gamma_p = \frac{\int_{\text{active}} \frac{1}{2}\text{Re}(\mathbf{E} \times \mathbf{H}^*).\hat{\mathbf{z}}d\mathbf{s}}{\int_{\text{all}} \frac{1}{2}\text{Re}(\mathbf{E} \times \mathbf{H}^*).\hat{\mathbf{z}}d\mathbf{s}} \tag{6.17}$$

where z is the direction of propagation. Using Eq. 6.17 the confinement factor for a 5-cascade ICL with 500 nm SCH is calculated to be 0.16.

This definition, although generally useful, is no longer valid for subwavelength metallic cavities. For a strongly guided mode Eq. 6.17 results in larger than unity values of Γ [104]. In those cases the energy confinement factor Γ_E must be used and is defined as,

$$\Gamma_E = \frac{\text{stored energy in the active medium}}{\text{total stored energy}}. \tag{6.18}$$

Equation 6.18 approaches to 6.17 only if the longitudinal component is negligible.

Electromagnetic energy is defined through the Poynting's theorem

$$\int_V \left[\mathbf{E} \cdot \frac{\partial \mathbf{D}}{\partial t} + \mathbf{H} \cdot \frac{\partial \mathbf{B}}{\partial t}\right] d\mathbf{r} = \int_V \left[\mathbf{J} \cdot \mathbf{E} + \nabla \cdot (\mathbf{E} \times \mathbf{H})\right] d\mathbf{r}. \tag{6.19}$$

For a linear dispersionless medium $\mathbf{D} = \epsilon\mathbf{E}$ and $\mathbf{B} = \mu\mathbf{H}$, where ϵ and μ are the complex

permittivity and permeability of the medium, respectively. Therefore

$$u = \frac{1}{2}(\mathbf{E}\cdot\mathbf{D} + \mathbf{B}\cdot\mathbf{H}) \tag{6.20}$$

denotes the total electromagnetic energy density. Accordingly, the Poynting's theorem can be rewritten as [105],

$$\frac{\partial u}{\partial t} + \nabla\cdot\mathbf{S} = -\mathbf{J}\cdot\mathbf{E} \tag{6.21}$$

where $\mathbf{S} = \mathbf{E}\times\mathbf{H}$ is the Poynting vector.

The first term on the left hand side of Eq. 6.21 represents the rate of change in the stored electromagnetic energy. The second term corresponds to power flow and the right hand side is the dissipated power at a given point in the volume of interest [105].

In dispersive media, Eq. 6.20 is no longer valid and the effective electromagnetic energy density follows

$$u_{\text{eff}} = \frac{1}{2}\text{Re}\left[\left.\frac{d(\omega'\epsilon(\omega))}{d\omega'}\right|_{\omega'=\omega}\right]|\mathbf{E}|^2 + \frac{1}{2}\text{Re}\left[\left.\frac{d(\omega'\mu(\omega))}{d\omega'}\right|_{\omega'=\omega}\right]|\mathbf{H}|^2, \tag{6.22}$$

where $\mathbf{E}(\mathbf{r})$ and $\mathbf{H}(\mathbf{r})$ are the harmonic electric and magnetic field. The first and second term describe the electric and magnetic energy density, respectively. Noteworthy, in metals below the plasma frequency, where the real part of permittivity assumes a negative value, Eq. 6.22 ensures a positive energy density. For a non-magnetic medium, $\mu = \mu_0$, Eq. 6.22 simplifies to,

$$u_{\text{eff}} = \frac{1}{2}\text{Re}[\epsilon_g(\omega) + \epsilon(\omega)]|\mathbf{E}(\mathbf{r})|^2 \tag{6.23}$$

where,

$$\epsilon_g(\omega) = \left.\frac{d(\omega'\epsilon(\omega'))}{d\omega'}\right|_{\omega'=\omega} \tag{6.24}$$

is the group permittivity.

Hence, the energy confinement Eq. 6.18 reads,

$$\Gamma_E = \frac{\displaystyle\int_{V_a} d\mathbf{r}\frac{1}{2}\mathrm{Re}\left[\epsilon_{g,a}(\omega) + \epsilon_{R,a}\right]|\mathbf{E}(\mathbf{r})|^2}{\displaystyle\int_{V} d\mathbf{r}\frac{1}{2}\mathrm{Re}\left[\epsilon_{g}(\omega) + \epsilon_{R}\right]|\mathbf{E}(\mathbf{r})|^2}, \tag{6.25}$$

where the subscript a refers to the active region [106].

6.4 Principles of Lasing in Metallic Cavities

Is there a fundamental limit on the size of a laser?

Conventional dielectric semiconductor lasers are 1D cavities with weekly guided modes in the transverse direction while the cavity is formed between two mirrors in the longitudinal direction. In order to form a standing wave in a resonator of length L, the electric field must repeat itself after a round-trip,

$$r_1 r_2 \exp([G_m - \alpha_i]L)\exp(-2j\beta L) = 1, \tag{6.26}$$

where r_1 and r_2 are the field reflectivity coefficients for the resonator mirrors, α_i is the waveguide internal loss, β is the propagation constant, and G_m is modal gain. The fraction of the material gain that contributes to the amplification in the cavity is determined by

the overlap of the electromagnetic mode and the gain medium, namely, the confinement factor, $G_M = \Gamma g_m$. From Eq. 6.26 and using $\beta = 2\pi n_{\text{eff}}/\lambda_0$ the phase condition imposes a lower bound on the resonator length via [58],

$$L = \lambda_0/2n_{\text{eff}} \tag{6.27}$$

where λ_0 is the free space wavelength and n_{eff} is the effective index of the mode. This is the so called diffraction limit. The only mechanism that can lower the absolute value of L is the increase in the mode effective index. The effective index in a 5-cascade dielectric waveguide is approximately 3.6 for, corresponding to a minimum L around 500 nm. In order to increase the effective index above the ordinary semiconductor values, SPPs should be used. As seen from Fig. 6.3, the effective index goes to infinity for localized SPPs and allows for reduction of cavity beyond the diffraction limit. This is the fundamental concept behind a spaser. For frequency ranges lower than ω_{sp}, corresponding to propagating SPPs, the dispersion relation provides effective indices higher than the dielectric waveguide, represented by the light line, which allows the phase condition to be fulfilled with smaller values of L. The penalty for increasing the effective index is the increased propagation loss.

Equation 6.26 also requires the field amplitude to be amplified to compensate for the waveguide loss and mirror reflection. Therefore [58].

$$\Gamma g_{th} = \alpha_i + \alpha_m = \alpha_{tot} \tag{6.28}$$

where α_m represents the loss of photons through the cavity mirrors is equal to $\frac{1}{L}\ln(\frac{1}{r_1 r_2})$. Hence, increasing the length of the resonator lowers the gain requirement by virtue of reducing the contribution of mirror loss to the total cavity loss. Consequently, reducing

the cavity length in the longitudinal direction increases the gain requirement significantly. This is the biggest challenge that must be overcome as the laser cavity size is reduced [104].

As mentioned in the discussion leading to Eq. 6.13, the quality factor is related to the optical loss via $Q = \omega_0/v_g\alpha_{tot}$ and, therefore, the threshold gain can be expressed in terms of the cavity quality factor

$$\Gamma g_{th} = \frac{\omega_0}{v_g Q} = \frac{2\pi n_g}{\lambda_0 Q} \tag{6.29}$$

where n_g is the mode group velocity. In the study of laser cavities, it is useful to break the quality factor into two parts: Q_{mat} and Q_{rad}. Q_{mat} refers to material loss in the cavity and Q_{rad} describes the radiation out of the cavity. Using this notation the cavity quality factor can be rewritten,

$$Q^{-1} = \frac{v_g(\alpha_m + \alpha_i)}{\omega_0} = Q_{\text{mat}}^{-1} + Q_{\text{rad}}^{-1}. \tag{6.30}$$

Subsequently, an external efficiency η_{ext} can be defined

$$\eta_{\text{ext}} = \frac{Q}{Q_{\text{rad}}}, \tag{6.31}$$

which quantifies the external radiation efficiency of the laser cavity [107].

The size limitation in the transverse direction is driven by the confinement requirement and is due to low index contrast in dielectric guides. As the waveguide dimensions become comparable to the wavelength, the mode extends considerably out of the waveguide and the confinement factor becomes very poor. When confinement is imposed using metal to form the cavity, the transverse size can be reduced to diffraction limit. Surpassing this

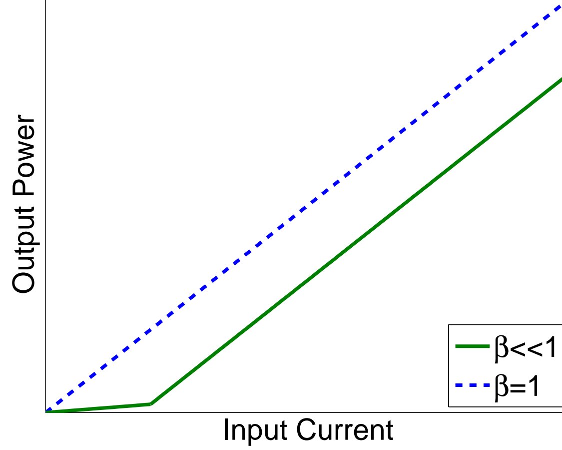

Figure 6.4: Output power in vs derive current for a conventional semiconductor (solid line) and in the limit when spontaneous emission is only coupled to a single lasing mode (dashed line).

limit is only possible through the use of SPPs. As shown in Eq. 6.4 and Fig. 6.3, plasmonic modes can be confined in the transverse direction below the diffraction limit, which is not achievable in a dielectric cavity.

Reducing the cavity size in all three dimensions results in significant reduction of the effective mode volume V_{eff}. Therefore, Purcell factor F, which is inversely proportional to the effective volume, is increased in accordance with Eq. 6.16 and the spontaneous emission coupling factor β is enhanced according to 6.14. The output power of a laser above the threshold reads [58],

$$P_{\text{out}} = \frac{\hbar\omega}{q}\eta_i \frac{\alpha_m}{\alpha_m + \alpha_i}(I - I_{\text{th}}) \tag{6.32}$$

whereas below threshold it follows

$$P_{\text{out}} = \frac{\hbar\omega}{q}\eta_i' \frac{\alpha_m}{\alpha_m + \alpha_i}\beta I. \tag{6.33}$$

These two relations manifest themselves in the famous LI curve for a semiconductor

laser. In the limit of 100% efficiency, $\eta_i = \eta_i' = 1$ as β approaches unity, *i.e.* as the spontaneous emission is only coupled into a single lasing mode, the onset of threshold disappears from input/output laser characteristic and the laser becomes *thresholdless*, as shown in Fig. 6.4 [80]. This behavior has been experimentally demonstrated in coaxial laser cavities at near infrared frequencies at cryogenic temperatures [88].

6.5 Mid-IR Microcavities Design and Simulations

As discussed earlier in previous sections, plasmonic cavities based on SPP standing waves are very effective in reducing the mode volume, thereby, confining the field well below the diffraction limit. Circularly symmetric cavities are particularly interesting for a number of important applications such as imaging. From a wide range of cavity configurations, coaxial cavity was chosen for its interesting properties, plasmonic modes, and compatibility with mid-IR active region. Therefore, in this section, we focus on a coaxial cavity and study the structure in great detail. Figure 6.5 illustrates the general schematics of a coaxial cavity. Due to its high plasma frequency and low loss, silver will be used throughout this section as the metal in the core and cladding of the cavity structure. Figure 6.2 depicts the dielectric function of silver at room temperature as obtained based on Drude model fit to the experimental data of Babar and Weaver 2015 [6]. A semiconductor active region with an effective refractive index of 3.41 at transparency is also considered as the gain medium which partially fills the interior volume. At low temperature, $T = 4K$, the imaginary part of the silver's dielectric function is scaled down by a factor of 100 [85], and a temperature variation of $dn/dT = 2e^{-4}[1/K]$ is assumed for the semiconductor region resulting in an optical index of 3.35 [85,88]. All the simulations are conducted based on the finite-element method (FEM) using COMSOL multiphysics.

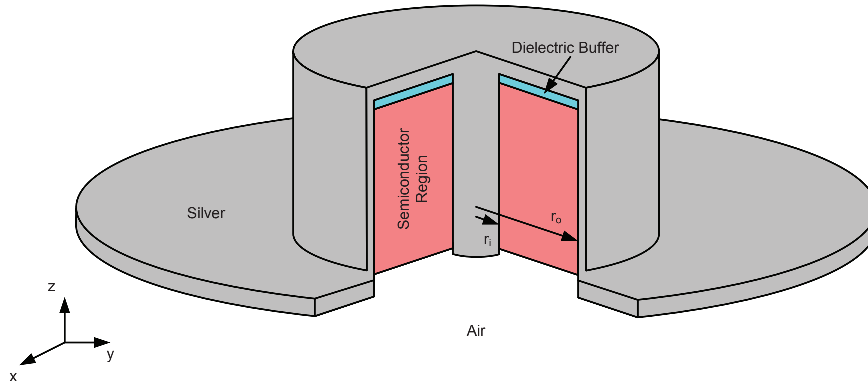

Figure 6.5: The Coaxial cavity

An illustrative way to design and optimize the plasmonic coaxial cavity involves treating the structure in terms of its basic building blocks, namely, the silver nanowire, coaxial gain region,and surrounding metal. Here, the coaxial cavity is envisioned as a finite coaxial waveguide with proper reflectors at both ends. The modes of a coaxial waveguide, especially its SPP mode, can be well understood as the result of the coupling between a nanowire waveguide at the core to the surrounding cylindrical waveguide. This picture provides deep insight into the nature of the underlying modes, which is essential for optimization of the cavity structure. Full-wave 3D simulation results will be applied at the end to verify and refine the obtained results. A similar cavity structure has been perviously studied at 1.44μm [88].

To understand the role of the nanowire, first an infinitely long silver nanowire embedded in a semiconductor medium is simulated. This structure supports a single mode. Figure 6.6 shows the magnitude of the electric field for the corresponding mode of a 200nm-diameter

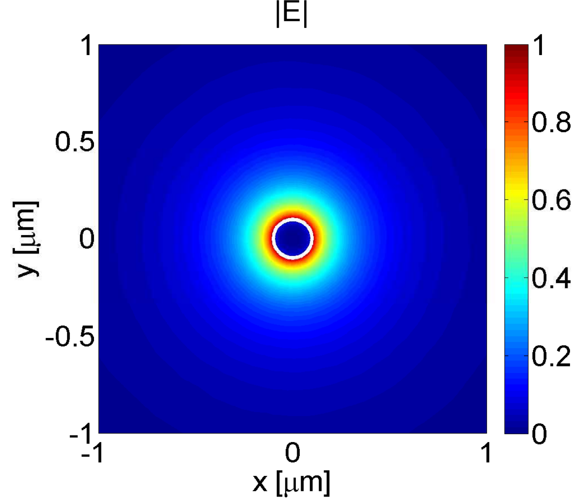

Figure 6.6: Magnitude of the electric field for a silver nanowire of 100 nm radius in a semiconductor medium

silver nanowire at $\lambda = 3.5\mu m$. As is evident from the mode profile, optical energy exponentially decays away from the silver-semiconductor boundary. Given the small penetration of the fields into the metal, light is tightly confined to the vicinity of the nanowire in the dielectric. This behaviour is closely reminiscent of the surface-wave character of SPPs at flat metal-dielectric boundaries.

Figure 6.7 plots the real and imaginary parts of the effective index as a function of the nanowire radius. The fact that the real part is greater than the dielectric's index of refraction confirms that this mode is indeed of plasmonic nature. Thus, similar to a flat metal-dielectric boundary, metal nanowires inside a dielectric medium can support propagating SPPs and, therefore, guide light. As the simulations demonstrate, the modal characteristics, however, significantly depend on the nanowire radius. In the limit of a large radius, the effective index approaches to that of a silver-dielectric flat boundary SPP, $i.e.$ $\sqrt{\epsilon_1 \epsilon_2/(\epsilon_1 + \epsilon_2)}$. Reducing the radius, on the other hand, results in an increase in

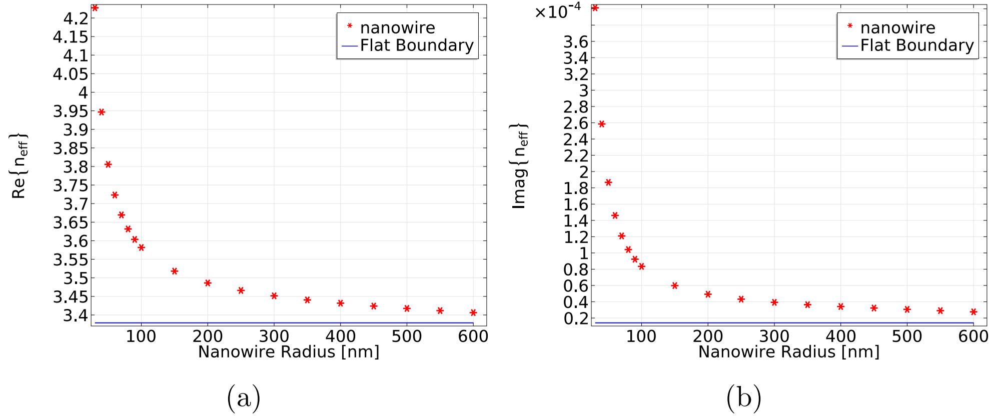

Figure 6.7: (a) Real and (b) Imaginary part of the effective index of a nanowire silver waveguide in the semiconductor medium versus the nanowire radius

the modal loss and effective index. Figure 6.7 indicates that the most interesting range of radii, from an applied viewpoint, is between 100 nm to 300 nm where the real part appreciably varies without much increase in the loss. Below 100 nm the loss shoots up and above 300 nm the confinement offered by the plasmonic mode is not fully exploited.

As the next step, a dielectric-filled metal cylindrical waveguide is studied. In analogy with the nanowire case, the metal is assumed to be silver and the inside dielectric is taken to be made of the ICL semiconductor at transparency. Figure 6.8 depicts the magnitude of electric field of the fundamental mode. Evidently, the optical energy is distributed within the entire dielectric region, with its peak located at the center. This mode much resembles that of a microwave cylindrical waveguide with PEC walls. The mode nature can be traced back to successively reflecting light rays at the metal-dielectric boundary.

The real and imaginary parts of the effective index are plotted versus the waveguide radius in Fig. 6.9. The mode exhibits a clear cut-off, where the effective index becomes

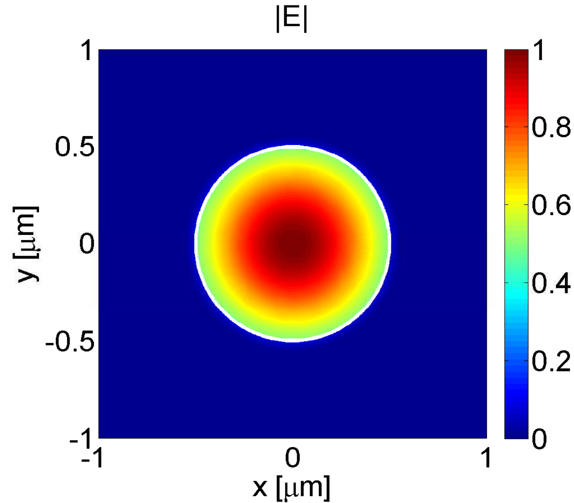

Figure 6.8: Magnitude of the electric field for a semiconductor Pillar of 500 nm radius embedded in silver

purely imaginary. The non-plasmonic nature of this mode is evident from its effective index being always smaller that the dielectric's index of refraction.

When combined together, a nanowire and a circular structure form a coaxial waveguide. As an example, Figure 6.10 shows $|E|$ for the plasmonic mode supported by such a waveguide with inner radius (r_i) of 100 nm and outer radius (r_o) of 400 nm. A simple comparison between this mode and the silver nanowire mode reveals that both essentially rely on the propagation of SPPs along the nanowire at the silver-semiconductor boundary. The outer conductor of the coaxial waveguide, however, limits the lateral extension of the pure nanowire plasmonic mode, thereby producing a highly confined optical guided wave.

The effective index of this mode is plotted versus the wavelength from visible to infrared in Fig 6.11. The plasmonic mode is the one with an effective index higher than the semiconductor refractive index. As seen in the figure, this mode does not show a cut-off,

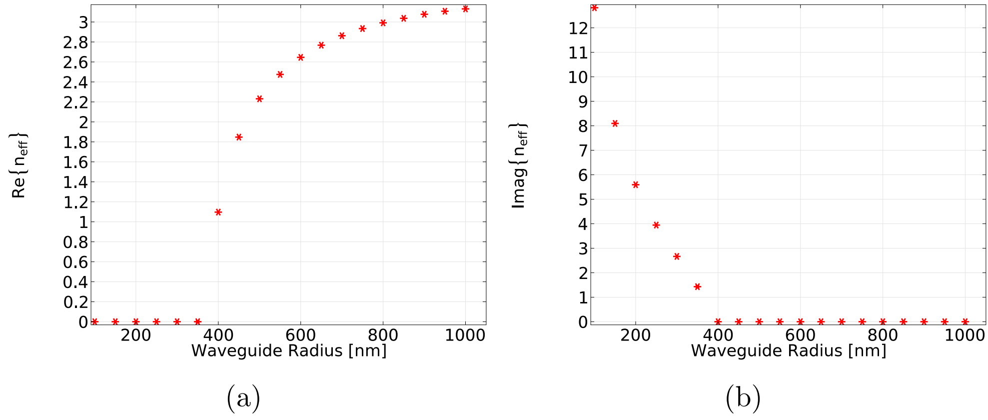

Figure 6.9: (a) Real and (b) Imaginary part of the effective index of a circular semiconductor waveguide surrounded by silver

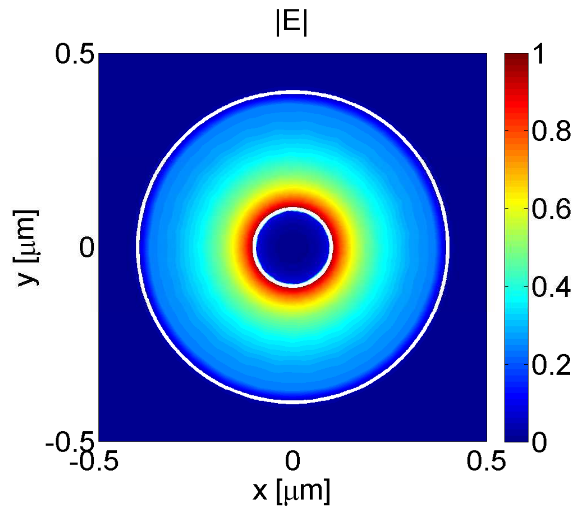

Figure 6.10: Magnitude of the electric field for the plasmonic mode of a coaxial waveguide with silver as inner and outer metal. The inner and outer radii are 100 nm and 400 nm respectively

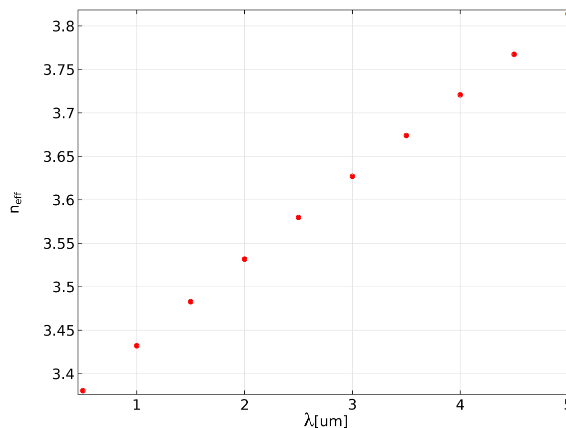

Figure 6.11: Real part of the effective index for the fundamental mode of a coaxial waveguide with inner radius of 100 nm, outer radius of 400 nm

and, therefore, is useful over a large range of wavelengths.

Figure 6.12 shows the change in the real and imaginary part of the waveguide effective index for a fixed outer radius as the inner radius varies. For $r_i \ll r_o$, the effective index is dominated by the nanowire characteristics and closely resembles Fig.6.7. As r_i approaches r_o, the mode strongly interacts with the outer metal, which is evident from the additional loss. Therefore, for a given r_o, *i.e.* the transverse footprint of the final structure, there is an optimum r_i that minimizes the waveguide loss.

The step-by-step analysis allows us to develop a methodology for optimizing the structure for any wavelength operation. In order to obtain an initial design for the transverse dimensions, a favourable r_i is first chosen from nanowire simulation. Then, r_o is taken as the minimum outer diameter for which the loss is not significantly increased compared to the pure nanowire mode. For an r_i/r_o combination, an effective index is derived for a given wavelength.

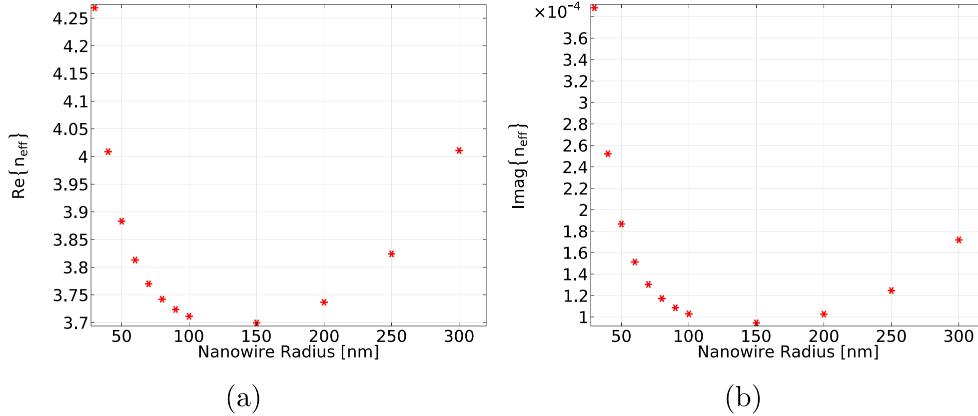

Figure 6.12: (a) Real and (b) Imaginary part of the effective index of a coaxial waveguide versus inner metal radii. The outer radius is kept constant at 400 nm

In order to determine the length of the cavity the transverse resonance technique (TRT) is used. TRT is a powerful means for analyzing optical and microwave resonators and waveguides [108, 109]. This method involves modeling the cavity as a terminated waveguide which supports resonant mode(s) as the result of the formation of standing waves associated the underlying guided mode(s). The resonance condition, thus, corresponds to that of a terminated transmission line, thereby, simplifying a vectorial 3D problem to a 1D scalar one. This approach is particularly helpful while designing a cavity based on a particular waveguide. The main advantage of TRT lies in its ability in identifying the role of the modal characteristic of the underlying guided mode(s), *i.e.* effective mode index, as well as the magnitude and phase of the terminal reflections in the formation of the resonant mode. In the following, TRT will be applied to design suitable cavity resonators for mid-IR micro-cavities based on the surface plasmon polariton modes of the previous section. Nevertheless, since TRT is only an approximate solution to the actual problem, the results will be re-examined in the next section for accuracy and further optimization

using a full-wave 3D analysis.

To form a coaxial cavity, the corresponding waveguide needs to be terminated at both ends. Considering the fabrication aspect of such a structure, silver naturally will terminate the top surface of the cavity since it will be deposited not only on the cavity side walls, but also on the top surface. Nevertheless, the silver cladding can potentially support a SPP mode of its own at the silver-semiconductor boundary on the top surface of the cavity. Such an unwanted mode competes with the desired cavity mode and acts as an additional loss channel. A simple remedy to this problem is to insert a dielectric buffer with sufficient index contrast to the semiconductor medium in order to lift the degeneracy between the desired SPP mode and the unwanted one.

The air can straightforwardly play the role of the termination at the other end, as it is common to etch away the substrate to achieve better reflection on the bottom side of the cavity. Having these two types of terminations in mind, TRT method was used to calculate the resonant wavelength of a 1D transmission line that consists of an *effective* semiconductor region terminated by air on one side and by SiO_2/silver on the other side. The effective index of the coaxial waveguide with $r_o = 400\ nm$ and $r_i \approx 100\ nm$ was used for the effective semiconductor region.

The index profile and the electric fields are shown in Fig. 6.13. Due to the asymmetric terminations, the electric field maximum is not at the center of the cavity. Figure 6.14 shows the dependance of the resonant wavelength on the semiconductor and the SiO_2 buffer heights.

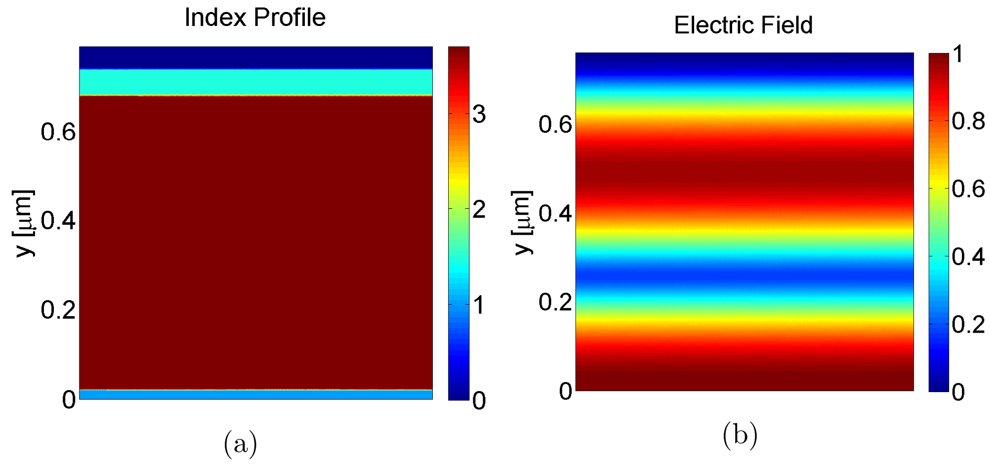

Figure 6.13: (a) Refractive index profile and (b) electric field of a 1D resonator comprised of a semiconductor medium with effective refractive index of 3.7 terminated on one side with an air interface and on the other side with a SiO_2/silver boundary

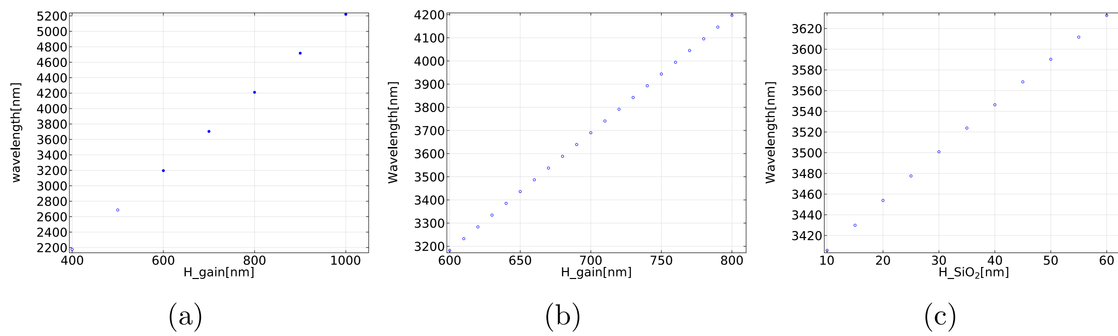

Figure 6.14: Dependance of the resonant wavelength on (a,b) the height of the semiconductor and (c) height of the SiO_2s layer

Once an estimate of the cavity dimensions are obtained, the cavity can be simulated in order to calculate the fundamental resonance parameters. As described in the previous section, the quality factor is the main cavity parameter that should be calculated and optimized as it is directly related to the threshold modal gain and carrier density. It is also beneficial to divide the cavity loss into material and radiation loss especially in the case of laser cavities. The former identifies the lost energy and the latter is related to the useable output radiation. Other figures of merit include the confinement factor, which relates the modal gain to the material gain, and effective mode volume and Purcell factor, which determines the contribution of cavity quantum electrodynamic (QED) effects in the cavity behaviour.

The next round of optimization, therefore, involves the cavity as a whole. So far, it was concluded that the inner radius of the cavity is around 100 nm and the height of the semiconductor region and the dielectric buffer are 660 nm and 30 nm, respectively. In order to maximize the cavity quality factor, a series of iterative simulations with parameter sweep were performed for both r_i and r_o. These simulations showed that the optimum inner diameter is indeed at 100 nm and the cavity quality factor is monotonically reduced as r_o is increased.

The curve associated with $\mathrm{Q_{cav}}$ in Fig. 6.15a demonstrates variations of Q versus r_o. The overall quality factor can be divided into the radiation and loss contributions as described in Eq. 6.30, both of which are also plotted in this figure. $\mathrm{Q_{rad}}$ is calculated by setting the imaginary part of silver permittivity to zero. $\mathrm{Q_{mat}}$ is scaled by a factor of 5 in Fig. 6.15a for ease of illustration. As the outer cavity radius is decreased, the material loss is increased and Q deviates from its radiative value. Since these simulations are using the

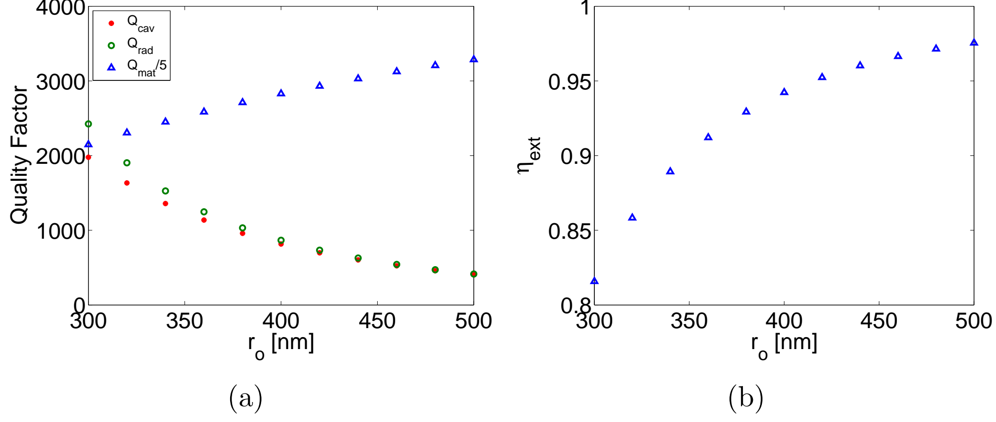

(a) (b)

Figure 6.15: (a) Quality factor as a function of outer radius of the coaxial cavity at 4K. Overall quality factor (stars) as well as Q_{rad} (circles) and $Q_{mat}/5$ (triangles)(b)External cavity efficiency as a function of cavity outer radius, both at 4K. Simulation was perform using eigenfrequency solver of COMSOL multiphysics in 2D axisymmetric mode.

low temperature dielectric constants, Q_{mat} is much higher that Q_{rad} and the radiative loss ultimately determines the quality factor especially at larger values of r_o. That explains the monotonic dependence of the quality factor to the cavity outer radius.

Fig 6.15b shows the external efficiency $\eta_{ext} = Q/Q_{ext}$ as a function of r_o. High values of η_{ext} are due to low material loss. Figure 6.16 shows the magnitude of the electric field as well as the cavity index profile for the coaxial cavity with $r_i = 130\ nm$, $r_o = 400\ nm$, height of the semiconductor region of 660 nm and dielectric buffer of 30 nm.

For room temperature values of the dielectric permittivities, the same strategy was followed. First r_o was set to 550 nm and r_i was varied to obtain the maximum Q which resulted in $r_i = 130\ nm$. Next r_i was kept at 130nm and r_o was varied. The maximum Q in this case was achieved at 400 nm. The next iteration resulted in $r_i = 140\ nm$ and $r_o = 400\ nm$ which confirms the convergence of this algorithm. This result is also in agree-

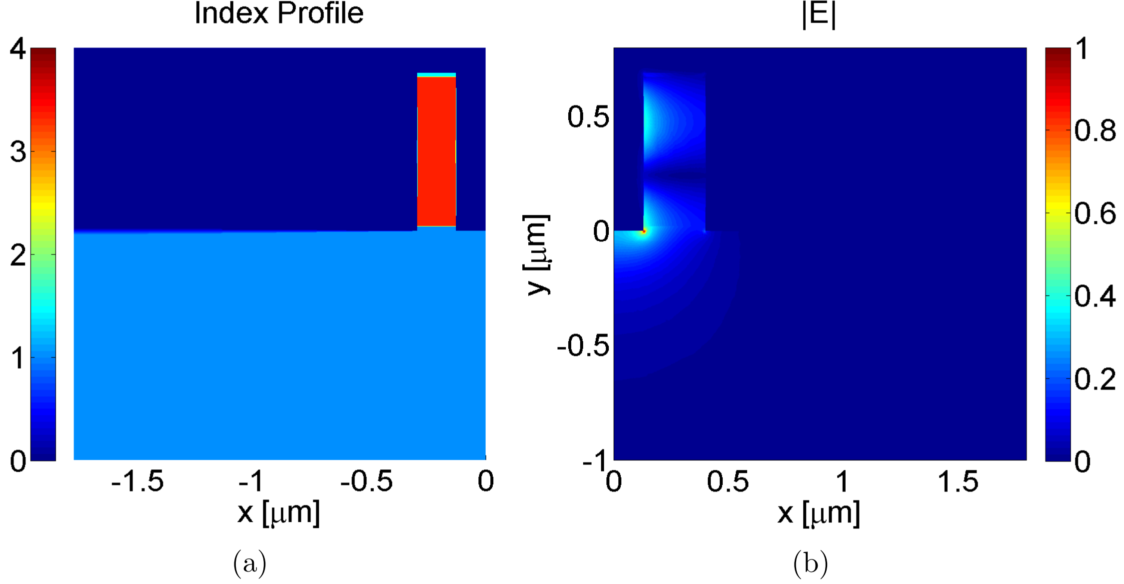

Figure 6.16: (a) Index profile and (b) magnitude of electric field for a vertical cross section of a coaxial cavity with $r_i = 130\ nm$, $r_o = 400\ nm$, height of the semiconductor region of 660 nm and dielectric buffer of 30 nm at 4K.

ment with what is approximated from the 2D waveguide analysis and proves the validity of this method.

As shown in Fig.6.17b, contrary to the low-temperature case represented in Fig. 6.15, the quality factor at RT exhibits a maximum value for a certain outer diameter. The reason for this behaviour becomes more obvious when the quality factor is split into absorption loss and radiation loss as shown in Fig. 6.17a. Due to higher loss at higher temperatures, Q_{mat} plays a much more dominant roll in the overall quality factor. Therefore, the tradeoff between the high absorption at low values of r_o and high radiation at higher r_o region creates an optimum value of the outer cavity dimensions.

The external cavity efficiency is also plotted in Fig. 6.18. Lower external efficiency is

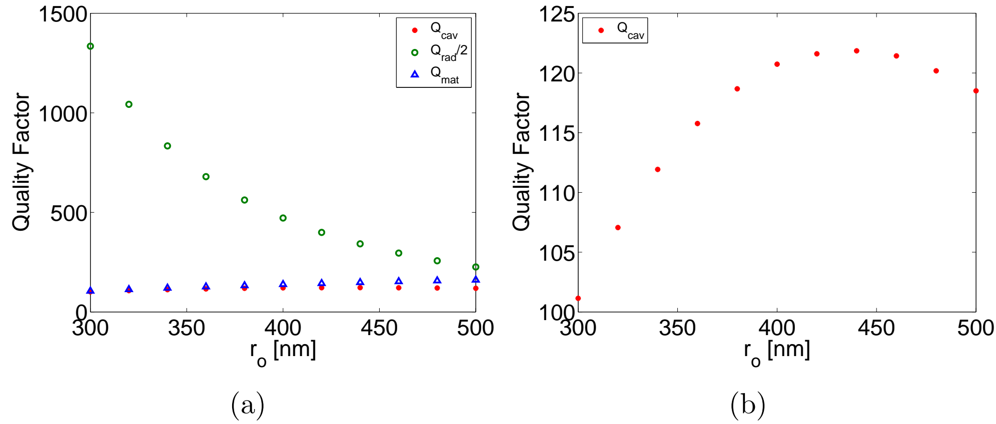

Figure 6.17: Quality factor as a function of outer radius of the coaxial cavity at RT. Overall quality factor (stars) as well as $Q_{rad}/2$ (circles) and Q_{mat} (triangles)(b)External cavity efficiency as a function of cavity outer radius.

due to higher loss at RT and could be adjusted by changing r_o at the expense of lower overall quality factor.

6.5.1 Full-Wave 3D Analysis

The full wave 3D analysis was also performed using finite-element method (FEM) in COMSOL. In order to obtain and analyze the various cavity modes, full-wave 3D analysis was performed for the optimized cavity structure at RT with the following dimensions obtained from waveguide and TRT analysis discussed so far,

- $r_{\mathrm{o}} = 400\ nm$
- $r_{\mathrm{i}} = 130\ nm$
- semiconductor region height $= 660\ nm$
- $\mathrm{SiO_2}$ height $= 30\ nm$

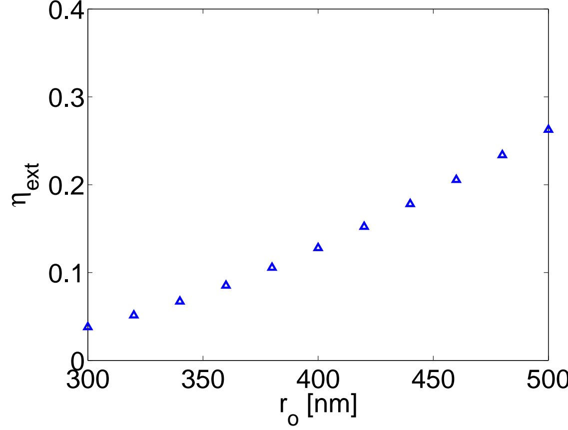

Figure 6.18: External cavity efficiency as a function of cavity outer radius at RT

The electric field of the fundamental resonant cavity mode is shown in Fig. 6.19. The magnetic field component parallel to the semiconductor-metal boundary, H_z, is zero for this mode, which is expected for a plasmonic mode. Given the finite magnitude of the longitudinal electric field, E_z, this mode is, strictly speaking, a TM mode. However, inside the cavity the longitudinal electric field is several orders of magnitude smaller than the transverse components. Therefore, this mode exhibits a quasi-TEM behaviour, where most of the energy is stored in the transverse field components. The strong E_x and E_y components inside the cavity are sketched by Fig. 6.19d and 6.19e, respectively. The E_z magnitude becomes appreciable only close to the output aperture of the cavity as shown in Fig. 6.19c. Once the mode is obtained, various cavity merits are calculated through data post processing according to the definitions introduced in the previous sections. For the specific cavity mentioned above, the wavelength of the fundamental resonant mode is at $3.5\mu m$ and the cavity has a quality factor of 118. The confinement factor and effective mode volume are calculated according to Eq. 6.25 and 6.15. For this structure, V_{eff} and Γ are equal to $0.14(\lambda/2n)^3$ and 84% respectively. The required modal gain is around 500 cm^{-1} and the Purcell factor has a value of 5.1×10^2.

In order to compare the cavity performance at room and low temperatures as well as the dependance of the various parameters on the cavity dimensions and loss, several structures have been simulated in full-wave 3D mode and the corresponding parameters are summarized in Table. 6.1. It can be seen that some parameters like the quality factor depend on both physical geometry and the permittivity values whereas other merits such as the confinement factor mostly depends on the modal behaviour and shows lower sensitivity to temperature or geometry. The quality factor can be enhanced at low temperatures by decreasing the outer diameter of the cavity. However, at RT, there exists an optimum value for r_o corresponding to the maximum Q. This is in agreement with the TRT simulation data. The threshold gain is lower considerably at low temperature clearly demonstrates the feasibility of the realization of this design at cryogenic temperature. Additional experimental data is required to determine the actual temperature range for this and similar design. Assuming a typical value of 0.005 for the spontaneous emission factor in semiconductor lasers, the higher ends of the Purcell factors reported in Table. 6.1 yield a spontaneous emission enhancement factor close to one and exhibits potential for thresholdless operation. It is also worth to note that the optimum cavity parameters obtained from the systematic 2D analysis are well lined up with the 3D simulations.

Other modes of the mid-IR micro-cavity are shown in Fig. 6.20. Aside from the fundamental mode at $\lambda = 3.5\mu m$, the resonant wavelength of the nearest modes are at $\lambda = 4.85\mu m$ and $\lambda = 2.83\mu m$ both with second order degeneracy. These modes fall outside of the gain bandwidth of the active region and will not compete with the fundamental mode. Thus, the device will operate in pure single mode. It is important to note the following points:

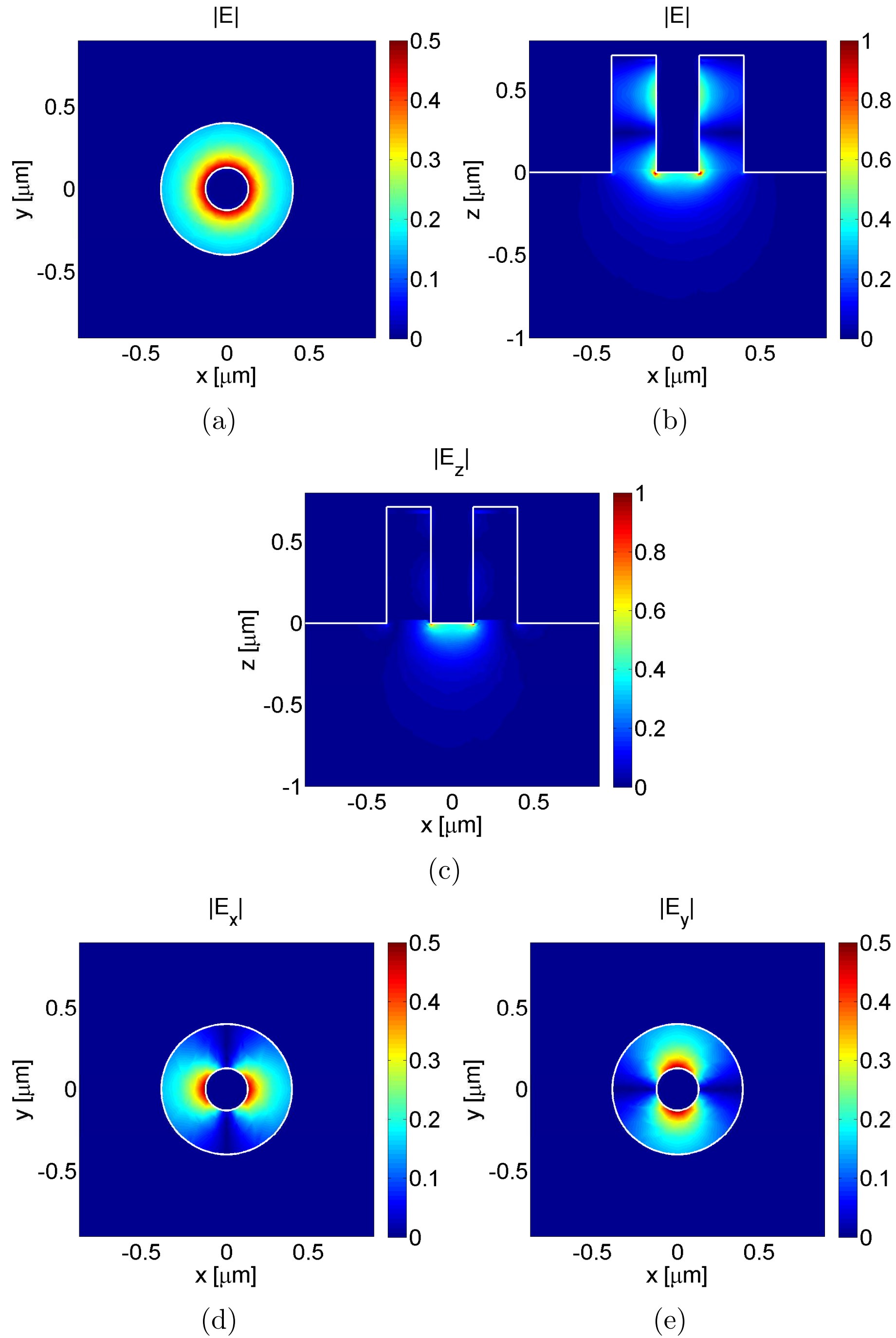

Figure 6.19: The electric field of the fundamental resonant mode of the optimized cavity at RT. (a) Magnitude of the electric field in XY plane at Z=450 nm (b) in XZ plane at Y=0 (c) z component of the electric field in YZ plane and (d) x and (e) y components of the electric field at XY plane at Z=450 nm

Table 6.1

Parameter	**RT**	**RT**	**4K**	**4K**	**4K**
$r_{\mathrm{o}}[nm]$	400	400	400	350	300
$r_{\mathrm{i}}[nm]$	200	130	130	130	130
$\lambda_0[\mu m]$	3.56	3.52	3.52	3.57	3.65
Q	107	118	810	1247	2014
Γ_E	83%	84%	84%	83%	81%
$\frac{V_{\mathrm{eff}}}{(\lambda/2n)^3}$	0.25	0.14	0.14	0.08	0.04
$\Gamma G_{\mathrm{th}}[cm^{-1}]$	562	515	75	48	29
$\mathrm{F_{cav}}$	2.60E+2	5.12E+2	3.51E+3	9.47E+3	3.06E+4

- The cavity modes are separated by a $\Delta f = 23$ [THz]. This frequency spacing at Mid-IR wavelength indicates a sparse modal content which allows for designing a cavity where only the fundamental mode coincides with the gain bandwidth

- As opposed to the other cavity modes, the fundamental mode is not a degenerate mode. Combined with the frequency spacing characteristics of the cavity, this means that the cavity can operate in a single frequency mode.

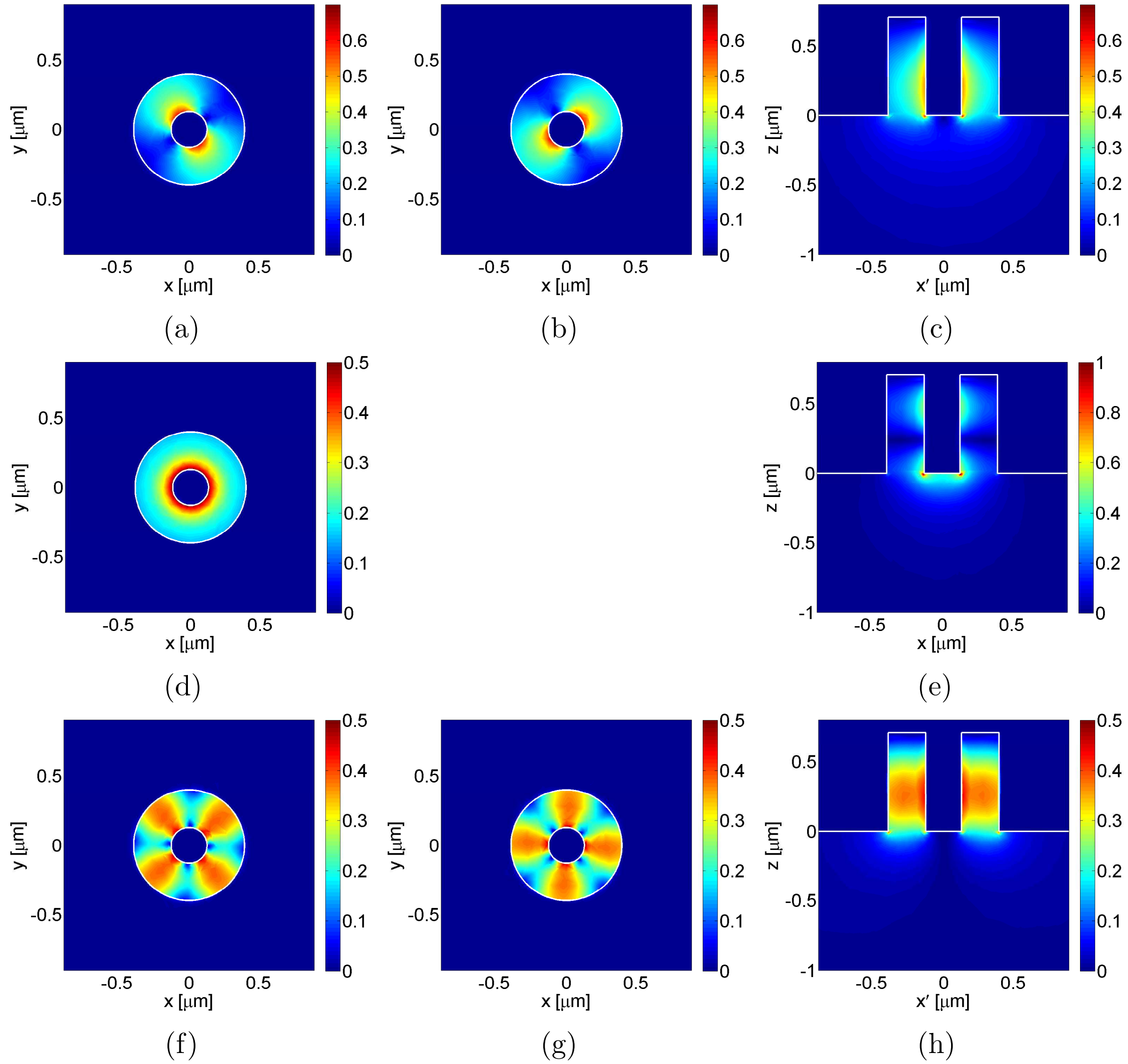

Figure 6.20: Modal content of the optimized mid-IR cavity. (a-c) The degenerate cavity mode at $\lambda = 4.85\mu m$ with Q=75 (d-e)The fundamental mode at $\lambda = 4.85\mu m$ with Q=118 (f-g) Higher order mode at $\lambda = 2.83\mu m$ with Q=210 and second order degeneracy

6.5.2 Optical Pumping and Scattering from Cavity

Given that this cavity is designed for optical pumping, it is important to discuss how efficiently the external excitation can be coupled into the cavity. For calculating the efficiency of the coupling of optical pump power to the cavity active region, the scattering problem was solved for the optimum cavity design. A plane wave incidence is considered at $\lambda = 2.098\mu m$, which corresponds to a HO:yttrium-aluminum-garnet (YAG) laser, assuming an imaginary refractive index of 0.05 for the gain medium [110]. The background excitation is a plane wave electric field polarized in the $\mathbf{x}$ direction. Figure 6.21 shows the scattered field together with the background excitation.

The scattered time average power flow is shown by the yellow arrows in Fig. 6.22. This results shows the circulation of the pump power through the cavity. Calculating the ratio of the absorbed power by the semiconductor region to the incident power on the device aperture,

$$\text{AbsorptionEfficiency} = \frac{\int_v P_{abs}\ dv}{\int_s P_{inc}\ d\mathbf{s}} \tag{6.34}$$

shows that 75% of the power impinged on the aperture is absorbed by the gain medium, indicating the compatibility of this design with optical pumping methods. Therefore, these devices can be efficiently pumped using a external laser at $\lambda = 2.098\mu m$. The input excitation is coupled into the cavity and is absorbed by the gain medium. Atoms will absorb energy from the field due to dipole interactions by going from ground to the excited states leading to population inversion and lasing.

6.5.3 Electrical Pumping

Several modifications to the design are required in order for the coaxial cavity to become compatible with electrical pumping schemes. First and foremost the metallic region of

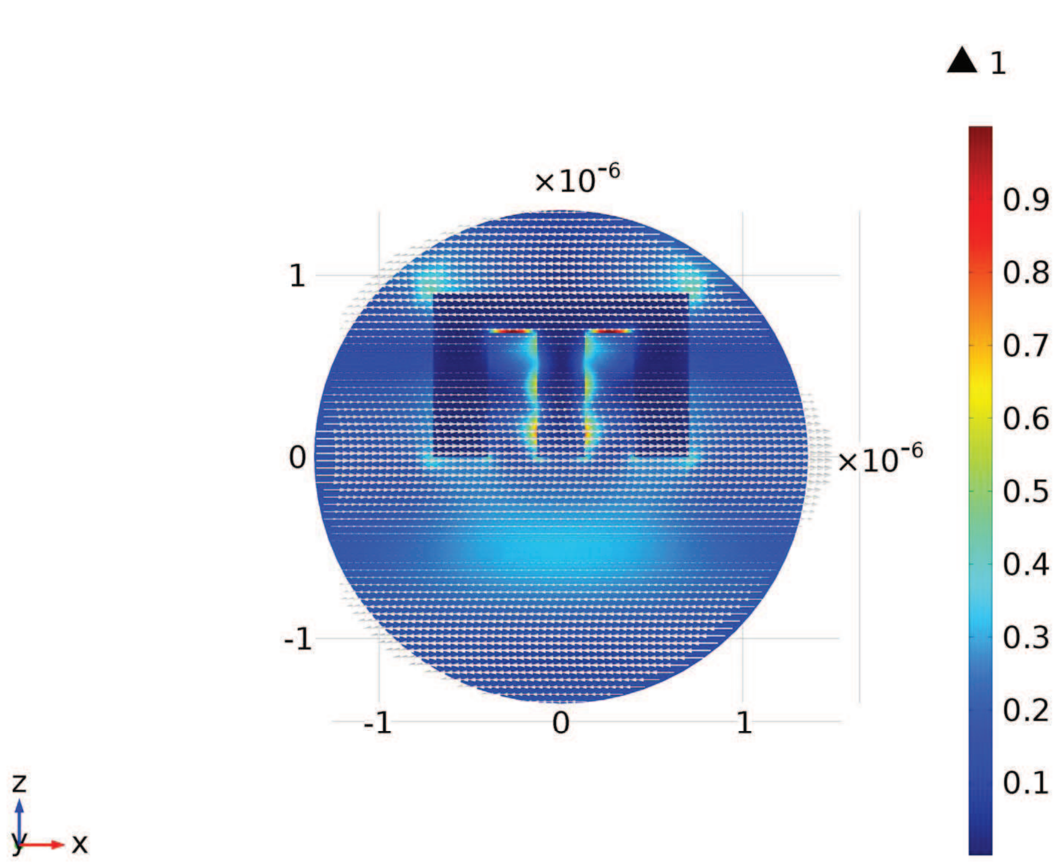

Figure 6.21: The background electric field, a plane wave in **x** direction, shown by white arrows and the normalized magnitude of the scattered field [color plot] from the structure.

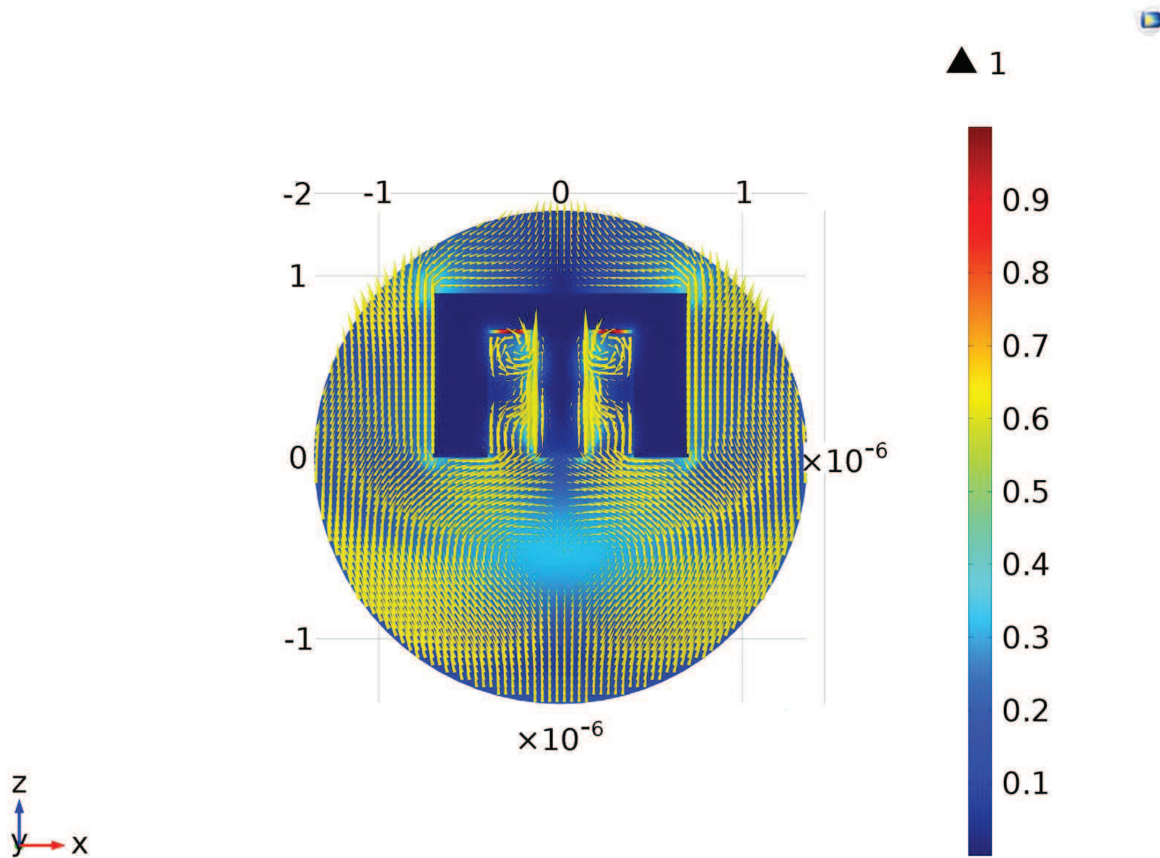

Figure 6.22: The normalized time averaged power flow of the scattered field shown by yellow arrows and the normalized magnitude of the scattered field from the structure [color plot].

the cavity should not be in direct contact with the active region. Thin layers of dielectric materials can be implemented to separate the active region from the metal. The thickness and refractive index of the dielectric have to be carefully tuned to minimize the mode perturbation. Other cavities such as a simple pillar could also be adapted to mid-IR emission gain mediums. In these scenarios the cavity terminations can be controlled by incorporating distributed Bragg reflectors (DFB) in the active region growth for maximum performance.

6.6 Discussions and Conclusions

In this chapter a systematic approach was demonstrated to design a coaxial cavity. The method not only enables the design of an optimum subwavelength plasmonic cavity at Mid-IR wavelength region, but also is amenable to any other spectral region due to its generality. Throughout the process, the role of each component on the final cavity merits was quantitatively studied. This systematic approach can be summarized as follows:

1. The plasmonic waveguide design $\longrightarrow$ the approximate silver nano-wire dimensions r_i
2. The pilar waveguide design $\longrightarrow$ outer diameter of the cavity r_o
3. The coaxial waveguide $\longrightarrow$ adjustment of r_i and r_o when combined is a single waveguide and the effective index of the traveling wave
4. The transverse resonant technique $\longrightarrow$ the component height determination and the tuning of the cavity wavelength
5. 2D and 3D simulation $\longrightarrow$ quality factor optimization.
6. Post processing and calculation of cavity parameters

The design methodology is illustrated by a flow chart in Fig. 6.23. Due to the plasmonic nature of the coaxial structure, high values of confinement and mode volumes much below the diffraction limit were obtained. Given that for a laser cavity minimizing the threshold gain is highly desirable, the 3D simulations have been focused on maximizing the quality factor. It was shown that in the presence of loss, especially at non cryogenic temperatures, the balance between loss and confinement results in an optimum design to achieve the most efficient cavity.

The active region for a coaxial cavity at Mid-IR can utilize the W-shape quantum well (QW) structure at the heart of an ICL. Several of these multi-QW periods can be stacked together and grown on a GaSb substrate as shown in Fig. 6.24b. Such a cavity can have applications in imaging and sensing. Figure 6.24a shows the dependance of the resonant wavelength on the ambient refractive index.

The resonant wavelength can be varied by 25 nm for ambient refractive index change of 0.1. This characteristic can be utilized in biological, chemical, or environmental sensing where the emission wavelength is monitored in presence of the detectent. Another interesting application of this design is in the field of Mid-IR imaging. Since the metal cladding shields the evanescent tail of the cavity mode, many of these micro-structures can be packed in a small region and may be pumped at the same time. As the resonant wavelength can be tuned in these cavities by merely changing the dimensions, such as array can cater to a range of wavelength not unlike a CCD camera. The radial polarization of the fundamental mode will become highly beneficial in such applications.

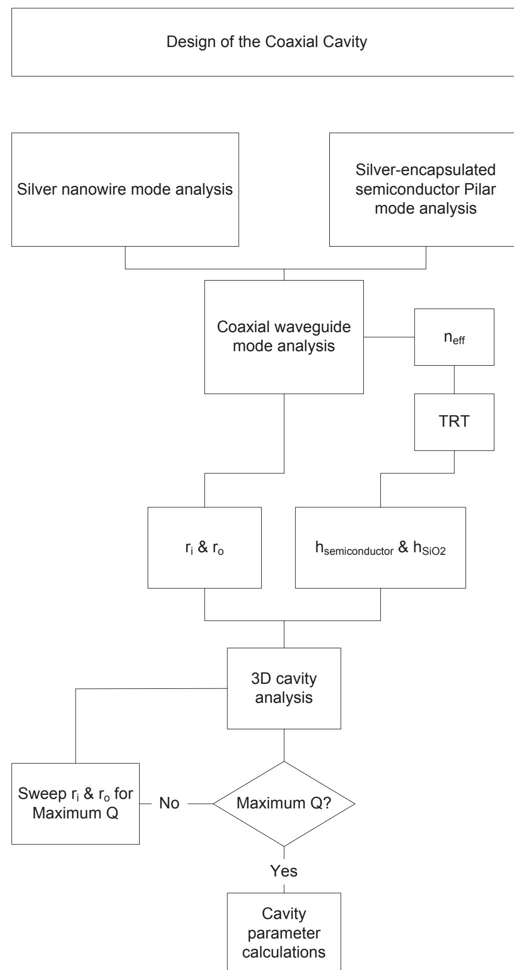

Figure 6.23: Flow chart of the systematic design method of a coaxial cavity

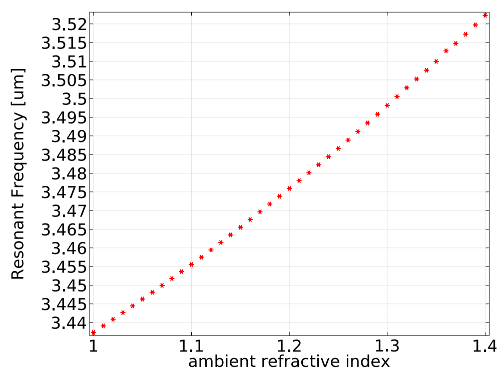

(a)

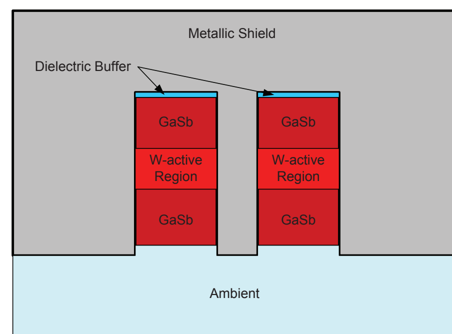

(b)

Figure 6.24: (a) The coaxial cavity resonant wavelength versus ambient refractive index (b) Proposed active region for the coaxial cavity at Mid-IR

Chapter 7

Conclusions and Future Works

This thesis began by reviewing the operational pricniples of ICLs and highlighting the unique properties of this category of cascaded lasers such as internal generation of electron and holes. ICLs were then compared to QCLs from several viewpoints including their material system, temperature sensitivity, record output power, number of cascades, polarization, and threshold power. It was argued that QCLs are best suited for high power operation in the mid-IR and ICLs are ideal for low-power battery operated applications. The list of milestones achieved are as follows:

- **RT CW Operation**
  The fabrication of ICL was explored in detail. Several techniques such as planarization were proposed and implemented to add more flexibility to the fabrication methods for future devices close to optical lithography limits. Moreover, several new generations of ICLs were developed based on novel designs, which ultimately led to RT operation. Throughout these studies, different aspects of the ICL designs were varied in order to assess their effects on the device performance. These variable parameters included the number of cascades (changing from 12 to 6 and 5), doping level

of the active region's p-doped areas, electron injector's length, and electron injector's doping level. It was experimentally demonstrated that the number of cascades affects the internal loss mainly through changing the confinement factor. Therefore, a major reduction in the internal loss was achieved by means of lowering the p-doping level in the GaInSb and GaSb wells in the active region. Furthermore, lowering the threshold current was accomplished primarily through the reduction of the length of electron injector. The lower loss and threshold current densities were the two main milestones towards achieving room temperature operation. Further optimizations such as increasing the n-doping of the electron injector resulted in additional reduction in the threshold current and improving the WPE. Maximum WPE of 6% was achieved form a 1 mm device producing up to 22 mW of usable power.

- **Fabrication and measurement of novel active region designs**

  In order to realize higher gain per cascade, novel active region designs, such as δ-strained QW design, were experimentally characterized. Even though these initial trials was proven far from optimized, their fabrication and measurements provided valuable insight to their design shortcomings. For example, it was experimentally shown that two distinct peaks were detectable in the output emission spectrum. These peaks were associated with separate and competing optical transitions in the active region. This discovery was linked to the high threshold current observed for these devices. Additional iteration of similar design is an important subject for future research which could lead to an active region design that outperform the W-active region.

- **Mid-IR anti-reflection coating design and fabrication for ICLs**

  As the next phase of the project, several material combinations were considered

for ARC application in mid-IR lasers. Each material was individually characterized from optical and fabrication points of view. Single and double layer ARCs were then designed and applied to ICLs. For each experiment, the fabricated laser die was packaged to allow precise control of the substrate temperature during the coating evaporation. Throughout these experimental analyses, YF_3, SiO_2, Al_2O_3, TiO_2, and ZnS were identified as the most promising candidates from a wide range of materials that were available at the time. The ARC design was always tailored to the specific laser wavelength. Coatings for a wide range of reflectivities from 0.15 to 7×10^{-4} were designed and fabricated. By monitoring the laser performance pre- and post ARC, the leakage current in the interband cascade lasers with different carrier concentrations was experimentally studied. Single layer Al_2O_3 and double layer ZnS-YF_3, ZnS-SiO_2, and TiO_2-SiO_2 ARCs were applied to mid-IR ICL devices to achieve reflectance ranging. It was observed that for lower reflectivity coatings the leakage current appreciably rises with increasing carrier concentration, thus, diminishing the slope efficiency improvements and in fact degrading the slope efficiency at very low reflectance. The ratio of leakage to threshold current was increased by 17% for high carrier concentrations at very low AR coating values. The results also allowed for experimental optimization of anti-reflection coatings for increased slope efficiency in Mid-infrared ICLs. The existence of an optimal value for the anti-reflection coatings in order to maximize the power in ICLs was deduced as an important result. Future work should focus on implementing design ideas such as the implementation of high barriers in the active region in order to improve the performance and stability of these lasers. Substantial improvement in the wall-plug efficiency and in the extractable power from ICL lasers are expected by appreciable reduction the carrier leakage.

- **Broadband Antireflection coating design, and fabrication for solar cells**

  As another application of ARCs, wide band coatings for GaSb solar cells were also developed. In order to provide lower reflectivity over a wider spectral range the ARC simulation tool was expanded to support three layer coating simulations. Further material characterizations and fabrication optimizations were implemented which resulted in 20% increase in solar cell efficiency and a record short circuit current. These results were not discussed in this thesis since they were not directly related to mid-IR lasers. Nevertheless, they were shared with the scientific community through the following publication [111].

- **Subwavelength Plasmonic cavity design at mid-IR**

  And last, but not least, the subwavelength micro cavities were considered at mid-IR with the W-active region at the heart of the design. The cavity design methodology was developed in a systematic way that is applicable to similar designs at other wavelengths. The contribution of the fundamental building blocks were inspected through simulations using FEM method in COMSOL multiphysics®. It was shown that due to the plasmonic nature of its mode, a coaxial cavity is able to confine the mode well below the wavelength which opens the possibility of realizing *thresholdless* lasers at these wavelengths. Optimal designs were investigated through 3D simulation and post processing calculations. A quality factor of 118 was calculated for a coaxial cavity with outer diameter 400 nm and height of $\approx$ 700 nm at RT. At low temperature the quality factor was shown to improve to above 2000. The energy confinement factor of about 84% was predicted with an effective volume below $0.25\frac{V_{\text{eff}}}{(\lambda/2n)^3}$ for all the design variations. Future work should focus on the fabrication of such cavities to correlate the simulation design with experimental data.

Bibliography

[1] E. C. Desk, "Electronic warfare and radar systems engineering handbook," 1997.

[2] I. Vurgaftman, W. Bewley, C. Canedy, C. Kim, M. Kim, C. Merritt, J. Abell, J. Lindle, and J. Meyer, "Rebalancing of internally generated carriers for mid-infrared interband cascade lasers with very low power consumption," *Nature Communications*, vol. 2, p. 585, 2011.

[3] G. Ryu, A. N. Chryssis, J. Amirloo, S. Saini, F. J. Towner, and M. Dagenais, "Gain and losses and room-temperature operation in interband cascade lasers," *Photonics Journal, IEEE*, vol. 4, no. 1, pp. 133–142, 2012.

[4] J. Amirloo, F. J. Towner, S. Saini, and M. Dagenais, "Carrier leakage in interband cascade lasers," in *Semiconductor Laser Conference (ISLC), 2012 23rd IEEE International*. IEEE, 2012, pp. 130–132.

[5] A. N. Chryssis, "Design and fabrication of high-performance interband cascade tunable external cavity lasers," Ph.D. dissertation, University of Maryland, College Park, 2010.

[6] S. Babar and J. Weaver, "Optical constants of cu, ag, and au revisited," *Applied Optics*, vol. 54, no. 3, pp. 477–481, 2015.

[7] P. B. Johnson and R.-W. Christy, "Optical constants of the noble metals," *Physical Review B*, vol. 6, no. 12, p. 4370, 1972.

[8] http://www.sspectra.com/sopra.html, "Sopra n&k database."

[9] M. Bass, C. DeCusatis, J. Enoch, V. Lakshminarayanan, G. Li, C. Macdonald, V. Mahajan, and E. Van Stryland, *Handbook of optics, Volume IV: Handbook of Optics, Third Edition Volume IV: Optical Properties of Materials, Nonlinear Optics, Quantum Optics (set)*. McGraw-Hill, Inc., 2009.

[10] B. Tatian, "Fitting refractive-index data with the sellmeier dispersion formula," *Applied optics*, vol. 23, no. 24, pp. 4477–4485, 1984.

[11] M. Debenham, "Refractive indices of zinc sulfide in the 0.405-13-μm wavelength range mary debenham," *Applied Optics*, vol. 23, no. 14/15, 1984.

[12] http://materion.com/, "Materion data base."

[13] I. Malitson, "Interspecimen comparison of the refractive index of fused silica," *JOSA*, vol. 55, no. 10, pp. 1205–1208, 1965.

[14] A. Einstein, "Zur quantentheorie der strahlung," *Physikalische Zeitschrift*, vol. 18, pp. 121–128, 1917.

[15] T. H. Maiman, "Stimulated optical radiation in ruby," 1960.

[16] I. Vurgaftman, W. W. Bewley, C. L. Canedy, C. S. Kim, M. Kim, J. R. Lindle, C. D. Merritt, J. Abell, and J. R. Meyer, "Mid-ir type-II interband cascade lasers," *Selected Topics in Quantum Electronics, IEEE Journal of*, vol. 17, no. 5, pp. 1435–1444, 2011.

[17] I. Vurgaftman, W. W. Bewley, C. L. Canedy, C. S. Kim, M. Kim, C. D. Merritt, J. Abell, and J. R. Meyer, "Interband cascade lasers with low threshold powers and high output powers," *Selected Topics in Quantum Electronics, IEEE Journal of*, vol. 19, no. 4, pp. 1 200 210–1 200 210, 2013.

[18] M. E. Flatte, J. Olesberg, and C. Grein, "Ideal performance of cascade and non-cascade intersubband and interband long-wavelength semiconductor lasers," *Applied physics letters*, vol. 75, no. 14, pp. 2020–2022, 1999.

[19] A. Krier, *Mid-infrared semiconductor optoelectronics.* Springer, 2007, vol. 118.

[20] C. N. Banwell and E. M. McCash, *Fundamentals of molecular spectroscopy.* McGraw-Hill London, 1983.

[21] M. Razeghi, N. Bandyopadhyay, Y. Bai, Q. Lu, and S. Slivken, "Recent advances in mid infrared (3-5μm) quantum cascade lasers," *Optical Materials Express*, vol. 3, no. 11, pp. 1872–1884, 2013.

[22] L. Shterengas, R. Liang, G. Kipshidze, T. Hosoda, S. Suchalkin, and G. Belenky, "Type-i quantum well cascade diode lasers emitting near 3 μm," *Applied Physics Letters*, vol. 103, no. 12, pp. 121 108–121 108, 2013.

[23] G. Belenky, L. Shterengas, G. Kipshidze, and T. Hosoda, "Type-i diode lasers for spectral region above 3 μm," *Selected Topics in Quantum Electronics, IEEE Journal of*, vol. 17, no. 5, pp. 1426–1434, 2011.

[24] R. Weih, A. Bauer, M. Kamp, and S. Höfling, "Interband cascade lasers with algaassb bulk cladding layers," *Optical Materials Express*, vol. 3, no. 10, pp. 1624–1631, 2013.

[25] T. Hosoda, G. Kipshidze, G. Tsvid, L. Shterengas, and G. Belenky, "Type-i gasb-based laser diodes operating in 3.1-to 3.3-μm wavelength range," *Photonics Technology Letters, IEEE*, vol. 22, no. 10, pp. 718–720, 2010.

[26] J. Faist, F. Capasso, D. L. Sivco, C. Sirtori, A. L. Hutchinson, and A. Y. Cho, "Quantum cascade laser," *Science*, vol. 264, no. 5158, pp. 553–556, 1994.

[27] M. Yamanishi, T. Edamura, K. Fujita, N. Akikusa, and H. Kan, "Theory of the intrinsic linewidth of quantum-cascade lasers: Hidden reason for the narrow linewidth and line-broadening by thermal photons," *Quantum Electronics, IEEE Journal of*, vol. 44, no. 1, pp. 12–29, 2008.

[28] R. Q. Yang, "Infrared laser based on intersubband transitions in quantum wells," *Superlattices and Microstructures*, vol. 17, pp. 77–83, 1995.

[29] J. Meyer, I. Vurgaftman, R. Yang, and L. Ram-Mohan, "Type-II and type-I interband cascade lasers," *Electronics Letters*, vol. 32, no. 1, pp. 45–46, 1996.

[30] J. Bradshaw, N. Breznay, J. Bruno, J. Gomes, J. Pham, F. Towner, D. Wortman, R. Tober, C. Monroy, and K. Olver, "Recent progress in the development of type-II interband cascade lasers," *Physica E: Low-dimensional Systems and Nanostructures*, vol. 20, no. 3, pp. 479–485, 2004.

[31] W. Bewley, H. Lee, I. Vurgaftman, R. Menna, C. Felix, R. Martinelli, D. Stokes, D. Garbuzov, J. Meyer, M. Maiorov *et al.*, "Continuous-wave operation of λ= 3.25 μm broadened-waveguide w quantum-well diode lasers up to t= 195 k," *Applied Physics Letters*, vol. 76, no. 3, pp. 256–258, 2000.

[32] R. Q. Yang, C. J. Hill, L. E. Christensen, and C. R. Webster, "Mid-ir type-II interband cascade lasers and their applications," in *Asia-Pacific Optical Communications*. International Society for Optics and Photonics, 2005, pp. 413–422.

[33] R. Q. Yang, C. J. Hill, and B. Yang, "High-temperature and low-threshold midinfrared interband cascade lasers," *Applied Physics Letters*, vol. 87, no. 15, pp. 151 109–151 109, 2005.

[34] C. Canedy, W. Bewley, G. Boishin, C. Kim, I. Vurgaftman, M. Kim, J. Meyer, and L. Whitman, "Molecular beam epitaxy growth and characterization of mid-ir type-II w diode lasers," *Journal of Vacuum Science & Technology B: Microelectronics and Nanometer Structures*, vol. 23, no. 3, pp. 1119–1124, 2005.

[35] C. Canedy, W. Bewley, J. Lindle, C. Kim, M. Kim, I. Vurgaftman, and J. Meyer, "High-power and high-efficiency midwave-infrared interband cascade lasers," *Applied physics letters*, vol. 88, no. 16, pp. 161 103–161 103, 2006.

[36] K. Mansour, Y. Qiu, C. Hill, A. Soibel, and R. Yang, "Mid-infrared interband cascade lasers at thermoelectric cooler temperatures," *Electronics Letters*, vol. 42, no. 18, pp. 1034–1036, 2006.

[37] W. Bewley, J. Nolde, D. Larrabee, C. Canedy, C. Kim, M. Kim, I. Vurgaftman, and J. Meyer, "Interband cascade laser operating cw to 257 k at λ= 3.7 μm," *Applied physics letters*, vol. 89, p. 161106, 2006.

[38] W. Bewley, C. Canedy, M. Kim, C. Kim, J. Nolde, J. Lindle, I. Vurgaftman, and J. Meyer, "Interband cascade laser operating to 269 k at λ= 4.05 μm," *Electronics Letters*, vol. 43, no. 5, pp. 283–284, 2007.

[39] C. Canedy, C. Kim, M. Kim, D. Larrabee, J. Nolde, W. Bewley, I. Vurgaftman, and J. Meyer, "High-power, narrow-ridge, mid-infrared interband cascade lasers," *Journal of Vacuum Science & Technology B: Microelectronics and Nanometer Structures*, vol. 26, no. 3, pp. 1160–1162, 2008.

[40] M. Kim, C. Canedy, W. Bewley, C. Kim, J. Lindle, J. Abell, I. Vurgaftman, and J. Meyer, "Interband cascade laser emitting at λ= 3.75 μm in continuous wave above room temperature," *Applied Physics Letters*, vol. 92, no. 19, pp. 191 110–191 110, 2008.

[41] I. Vurgaftman, C. Canedy, C. Kim, M. Kim, W. Bewley, J. Lindle, J. Abell, and J. Meyer, "Mid-infrared interband cascade lasers operating at ambient temperatures," *New Journal of Physics*, vol. 11, no. 12, p. 125015, 2009.

[42] R. Q. Yang, Z. Tian, R. T. Hinkey, F. Zhao, K. Mansour, C. J. Hill, and Y. Qiu, "Recent progress in interband cascade lasers with separate confinement layers," in *SPIE OPTO: Integrated Optoelectronic Devices*. International Society for Optics and Photonics, 2009, pp. 72 300S–72 300S.

[43] A. Chryssis, G. Ryu, and M. Dagenais, "Measurement of internal quantum efficiency and temperature dependence of gain and loss in interband cascade lasers near room-temperature," in *Semiconductor Laser Conference (ISLC), 2010 22nd IEEE International*. IEEE, 2010, pp. 43–44.

[44] ——, "Thermal impedance of epi-up and epi-down interband cascade lasers," in *IEEE Photonics Society, 2010 23rd Annual Meeting of the*. IEEE, 2010, pp. 421–422.

[45] C. Canedy, J. Abell, W. Bewley, E. Aifer, C. Kim, J. Nolde, M. Kim, J. Tischler, J. Lindle, E. Jackson *et al.*, "Molecular beam epitaxial growth effects on type-II

antimonide lasers and photodiodes," *Journal of Vacuum Science & Technology B: Microelectronics and Nanometer Structures*, vol. 28, p. C3G8, 2010.

[46] M. O. Fischer, M. Von Edlinger, L. Nähle, J. Koeth, A. Bauer, M. Dallner, S. Höfling, L. Worschech, A. W. Forchel, S. Belahsene *et al.*, "Dfb lasers for sensing applications in the 3.0-3.5 um wavelength range," in *SPIE OPTO*. International Society for Optics and Photonics, 2011, pp. 79 450E–79 450E.

[47] S. Höfling, R. Weih, A. Bauer, M. Kamp, and A. Forchel, "Room temperature continuous wave interband cascade lasers for gas sensing," in *Society of Photo-Optical Instrumentation Engineers (SPIE) Conference Series*, vol. 8432, 2012, p. 15.

[48] G. Ryu, J. Amirloo, S. Saini, F. Towner, and M. Dagenais, "62 mw output power, room-temperature operation, cw interband cascade laser," in *CLEO: Science and Innovations*. Optical Society of America, 2012.

[49] W. W. Bewley, C. L. Canedy, C. S. Kim, M. Kim, C. D. Merritt, J. Abell, I. Vurgaftman, and J. R. Meyer, "High-power room-temperature continuous-wave mid-infrared interband cascade lasers," *Optics Express*, vol. 20, no. 19, pp. 20 894–20 901, 2012.

[50] I. Vurgaftman, J. R. Meyer, C. L. Canedy, W. W. Bewley, J. R. Lindle, C.-s. Kim, M. Kim *et al.*, "High-temperature interband cascade lasers," 2012.

[51] W. Bewley, C. Kim, C. Canedy, C. Merritt, I. Vurgaftman, J. Abell, J. Meyer, and M. Kim, "High-power, high-brightness continuous-wave interband cascade lasers with tapered ridges," *Applied Physics Letters*, vol. 103, no. 11, pp. 111 111–111 111, 2013.

[52] R. Weih, M. Kamp, and S. Höfling, "Interband cascade lasers with room temperature threshold current densities below 100 a/cm2," *Applied Physics Letters*, vol. 102, p. 231123, 2013.

[53] S. L. Chuang, *Physics of photonic devices.* John Wiley & Sons, 2012, vol. 80.

[54] J. Faist, "Wallplug efficiency of quantum cascade lasers: Critical parameters and fundamental limits," *Applied physics letters*, vol. 90, no. 25, pp. 253 512–253 512, 2007.

[55] I. Vurgaftman, J. Meyer, and L. Ram-Mohan, "Band parameters for III-V compound semiconductors and their alloys," *Journal of applied physics*, vol. 89, no. 11, pp. 5815–5875, 2001.

[56] R. Bartolo, S. Saini, T. Ren, Y. Zhu, M. Dagenais, H. Shen, J. Pamulapati, W. Zhou, O. King, and F. Johnson, "Polarization-independent waveguide modulators using 1.57-μm/spl δ/-strained ingaas-ingaasp quantum wells," *Photonics Technology Letters, IEEE*, vol. 11, no. 5, pp. 554–556, 1999.

[57] http://optics.synopsys.com/rsoft/, "Rsoft."

[58] L. Coldren and S. Corzine, *Diode lasers and photonic integrated circuits.* John Wiley & Sons: New York, 1995.

[59] G. Ryu, "III-V optoelectronic devices: Room temperature cw operation of interband cascade laser & high efficiency p-side down ingan/gan solar cell," Ph.D. dissertation, University of Maryland, College Park, 2011.

[60] R. Maulini, "Broadly tunable mid-infrared quantum cascade lasers for spectroscopic applications," Ph.D. dissertation, Institut de Physique,University of Neuchatel, Switzerland, 2006.

[61] T. Saitoh, T. Mukai, and O. Mikami, "Theoretical analysis and fabrication of antireflection coatings on laser-diode facets," *Lightwave Technology, Journal of*, vol. 3, no. 2, pp. 288–293, 1985.

[62] I. Wu *et al.*, *Real-time in situ ellipsometry for the controlled deposition of anti-reflection coatings on semiconductor laser facets*, 1993.

[63] Y. Hu, *Multilayer Dielectric Coatings for Optoelectronic Devices.* University of Maryland, College Park, 2000.

[64] H. Macleod, "Monitoring of optical coatings," *Applied optics*, vol. 20, no. 1, pp. 82–89, 1981.

[65] G. Ghosh, *Handbook of Optical Constants of Solids: Handbook of Thermo-Optic Coefficients of Optical Materials with Applications.* Academic Press, 1998.

[66] F. A. Jenkins and H. E. White, "Fundamentals of optics," *New York: McGraw-Hill, 1957, 3rd ed.*, vol. 1, 1957.

[67] A. Paint, "Tests for chemical, physical, and optical properties; appearance, volume 06.01 of annual book of astm standards," *ASTM International*, 2009.

[68] J. Amirloo, S. Saini, and M. Dagenais, "Effect of carrier leakage on optimal ar coatings in mid-infrared interband cascade lasers," *Photonics Journal, IEEE*, vol. 7, no. 2, p. 1501511, 2015.

[69] D. Botez, J. C. Shin, S. Kumar, L. J. Mawst, I. Vurgaftman, and J. R. Meyer, "Electron leakage and its suppression via deep-well structures in 4.5-to 5.0-μm-emitting quantum cascade lasers," *Optical Engineering*, vol. 49, no. 11, pp. 111 108–111 108, 2010.

[70] R. Maulini, A. Lyakh, A. Tsekoun, R. Go, C. Pflügl, L. Diehl, F. Capasso, and C. K. N. Patel, "High power thermoelectrically cooled and uncooled quantum cascade lasers with optimized reflectivity facet coatings," *Applied Physics Letters*, vol. 95, no. 15, p. 151112, 2009.

[71] D. Botez, J. C. Shin, J. Kirch, C.-C. Chang, L. Mawst, and T. Earles, "Multidimensional conduction-band engineering for maximizing the continuous-wave (cw) wallplug efficiencies of mid-infrared quantum cascade lasers," *Selected Topics in Quantum Electronics, IEEE Journal of*, vol. 19, no. 4, pp. 1 200 312–1 200 312, 2013.

[72] J. Kirch, J. Shin, C.-C. Chang, L. Mawst, D. Botez, and T. Earles, "Tapered active-region quantum cascade lasers (λ= 4.8 μm) for virtual suppression of carrier-leakage currents," *Electronics letters*, vol. 48, no. 4, pp. 234–235, 2012.

[73] C. Ning, "Semiconductor nanolasers," *physica status solidi (b)*, vol. 247, no. 4, pp. 774–788, 2010.

[74] C. Walther, G. Scalari, M. I. Amanti, M. Beck, and J. Faist, "Microcavity laser oscillating in a circuit-based resonator," *Science*, vol. 327, no. 5972, pp. 1495–1497, 2010.

[75] K. Iga, "Surface-emitting laser-its birth and generation of new optoelectronics field," *Selected Topics in Quantum Electronics, IEEE Journal of*, vol. 6, no. 6, pp. 1201–1215, 2000.

[76] O. Painter, R. Lee, A. Scherer, A. Yariv, J. O'brien, P. Dapkus, and I. Kim, "Two-dimensional photonic band-gap defect mode laser," *Science*, vol. 284, no. 5421, pp. 1819–1821, 1999.

[77] A. Levi, S. McCall, S. Pearton, and R. Logan, "Room temperature operation of submicrometre radius disk laser," *Electronics Letters*, vol. 29, no. 18, pp. 1666–1667, 1993.

[78] E. Purcell, "Spontaneous emission probabilities at radio frequencies," *Physical Review*, vol. 69, p. 681, 1946.

[79] A. M. T. Kobayashi, T. Segawa and T. Sueta, *Technical Digest of the 43rd Fall Meeting of Japanese Society of Applied Physics*, vol. 69, pp. paper 29a–B–6, Sept., 1982 (in Japanese).

[80] H. Yokoyama, "Physics and device applications of optical microcavities," *Science*, vol. 256, no. 5053, pp. 66–70, 1992.

[81] M. P. Nezhad, K. Tetz, and Y. Fainman, "Gain assisted propagation of surface plasmon polaritons on planar metallic waveguides," *Opt. Express*, vol. 12, no. 17, pp. 4072–4079, 2004.

[82] S. A. Maier, "Gain-assisted propagation of electromagnetic energy in subwavelength surface plasmon polariton gap waveguides," *Optics communications*, vol. 258, no. 2, pp. 295–299, 2006.

[83] A. Maslov and C. Ning, "Size reduction of a semiconductor nanowire laser by using metal coating," in *Integrated Optoelectronic Devices 2007*. International Society for Optics and Photonics, 2007, pp. 64 680I–64 680I.

[84] M. T. Hill, "Nanophotonics: Lasers go beyond diffraction limit," *Nature Nanotechnology*, vol. 4, no. 11, pp. 706–707, 2009.

[85] M. T. Hill, Y.-S. Oei, B. Smalbrugge, Y. Zhu, T. De Vries, P. J. Van Veldhoven, F. W. Van Otten, T. J. Eijkemans *et al.*, "Lasing in metallic-coated nanocavities," *Nature Photonics*, vol. 1, no. 10, pp. 589–594, 2007.

[86] K. Ding and C. Ning, "Metallic subwavelength-cavity semiconductor nanolasers," *Light: Science & Applications*, vol. 1, no. 7, p. e20, 2012.

[87] M. T. Hill, M. Marell, E. S. Leong, B. Smalbrugge, Y. Zhu, M. Sun, P. J. van Veldhoven, E. J. Geluk, F. Karouta, Y.-S. Oei *et al.*, "Lasing in metal-insulator-metal sub-wavelength plasmonic waveguides," *Opt. Express*, vol. 17, no. 13, pp. 11 107–11 112, 2009.

[88] M. Khajavikhan, A. Simic, M. Katz, J. Lee, B. Slutsky, A. Mizrahi, V. Lomakin, and Y. Fainman, "Thresholdless nanoscale coaxial lasers," *Nature*, vol. 482, no. 7384, pp. 204–207, 2012.

[89] D. J. Bergman and M. I. Stockman, "Surface plasmon amplification by stimulated emission of radiation: quantum generation of coherent surface plasmons in nanosystems," *Physical Review Letters*, vol. 90, no. 2, p. 027402, 2003.

[90] M. Noginov, G. Zhu, A. Belgrave, R. Bakker, V. Shalaev, E. Narimanov, S. Stout, E. Herz, T. Suteewong, and U. Wiesner, "Demonstration of a spaser-based nanolaser," *Nature*, vol. 460, no. 7259, pp. 1110–1112, 2009.

[91] M. T. Hill, "Status and prospects for metallic and plasmonic nano-lasers [invited]," *JOSA B*, vol. 27, no. 11, pp. B36–B44, 2010.

[92] K. Ding, L. Yin, M. T. Hill, Z. Liu, P. J. van Veldhoven, and C. Ning, "An electrical injection metallic cavity nanolaser with azimuthal polarization," *Applied Physics Letters*, vol. 102, no. 4, pp. 041 110–041 110, 2013.

[93] K. Yu, A. Lakhani, and M. C. Wu, "Subwavelength metal-optic semiconductor nanopatch lasers," *Optics Express*, vol. 18, no. 9, pp. 8790–8799, 2010.

[94] F. Peng, B. Yao, S. Yan, W. Zhao, and M. Lei, "Trapping of low-refractive-index particles with azimuthally polarized beam," *JOSA B*, vol. 26, no. 12, pp. 2242–2247, 2009.

[95] Q. Zhan, "Cylindrical vector beams: from mathematical concepts to applications," *Adv. Opt. Photon*, vol. 1, no. 1, pp. 1–57, 2009.

[96] M. P. Nezhad, A. Simic, O. Bondarenko, B. Slutsky, A. Mizrahi, L. Feng, V. Lomakin, and Y. Fainman, "Room-temperature subwavelength metallo-dielectric lasers," *Nature Photonics*, vol. 4, no. 6, pp. 395–399, 2010.

[97] M. T. Hill and M. J. Marell, "Surface-emitting metal nanocavity lasers," *Advances in Optical Technologies*, vol. 2011, 2011.

[98] B.-T. Lee, T. Hayes, P. Thomas, R. Pawelek, and P. Sciortino, "Sio_2 mask erosion and sidewall composition during ch_4h_2 reactive ion etching of ingaasp/inp," *Applied physics letters*, vol. 63, no. 23, pp. 3170–3172, 1993.

[99] S. A. Maier, *Plasmonics: fundamentals and applications.* Springer Science & Business Media, 2007.

[100] N. Ashcroft and N. Mermin, *Solid State Physics.* Holt, Rinehart and Winston, 1976.

[101] B. E. Saleh, M. C. Teich, and B. E. Saleh, *Fundamentals of photonics.* Wiley New York, 1991, vol. 22.

[102] J. T. Robinson, C. Manolatou, L. Chen, and M. Lipson, "Ultrasmall mode volumes in dielectric optical microcavities," *Physical review letters*, vol. 95, no. 14, p. 143901, 2005.

[103] K. Ding, Z. Liu, L. Yin, M. Hill, M. Marell, P. Van Veldhoven, R. Nöetzel, and C. Ning, "Room-temperature continuous wave lasing in deep-subwavelength metallic cavities under electrical injection," *Physical Review B*, vol. 85, no. 4, p. 041301, 2012.

[104] M. T. Hill and M. C. Gather, "Advances in small lasers," *Nature Photonics*, vol. 8, no. 12, pp. 908–918, 2014.

[105] J. D. Jackson, *Classical Electrodynamics, 3rd Edition.* John Wiley & Sons: New York, 1998.

[106] S.-W. Chang and S. L. Chuang, "Fundamental formulation for plasmonic nanolasers," *Quantum Electronics, IEEE Journal of*, vol. 45, no. 8, pp. 1014–1023, 2009.

[107] B. Zhang, T. Okimoto, T. Tanemura, and Y. Nakano, "Proposal and numerical study on capsule-shaped nanometallic semiconductor lasers," *Japanese Journal of Applied Physics*, vol. 53, no. 11, p. 112703, 2014.

[108] D. M. Pozar, *Microwave engineering.* John Wiley & Sons, 2009.

[109] C. A. Balanis, *Advanced engineering electromagnetics.* Wiley Online Library, 2012, vol. 111.

[110] C. Felix, W. Bewley, I. Vurgaftman, L. Olafsen, D. Stokes, J. Meyer, and M. Yang, "High-efficiency midinfrared w laser with optical pumping injection cavity," *Applied physics letters*, vol. 75, no. 19, pp. 2876–2878, 1999.

[111] T. Li, J. Amirloo, J. Murray, K. Sablon, J. Little, P. Uppal, J. Munday, and M. Dagenais, "A comparison of bulk and quantum dot gaas solar cells," in *IEEE Photonics Conference 2012*.

Appendices

Appendix A

Material Dispersion and Refractive Indices in Mid-IR

Single Layer Coatings Materials

- Zirconium dioxide (ZrO_2)

  ZrO_2 refractive index in the visible range is plotted in Fig. A.1 together with the ellipsometry data. Cauchy equation was used to fit and estimate the refractive index in the 3-4 μm region, and results in an index around 1.89 in the infrared region.

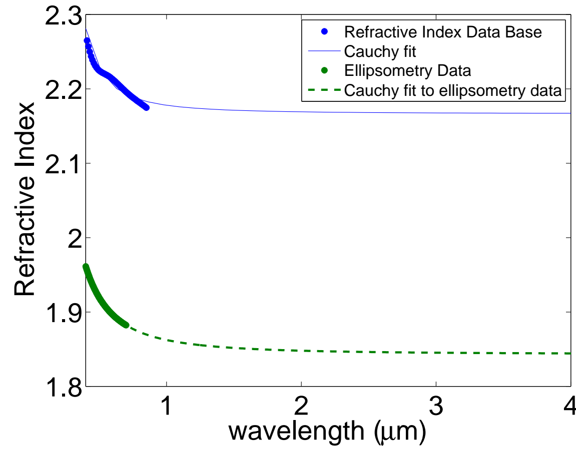

Figure A.1: ZrO_2 dispersion curve from SOPRA N&K Database [8], its Cauchy fit and experimental ellipsometry data

- Tantalum pentoxide (Ta_2O_5)

  Figure A.2 shows the refractive index spectrum of Ta_2O_5 in the visible range as well as the ellipsometry data. Fitted curve using Cauchy approximation is also included. The fitted values predict an index of 1.76 within 3μm-4μm range.

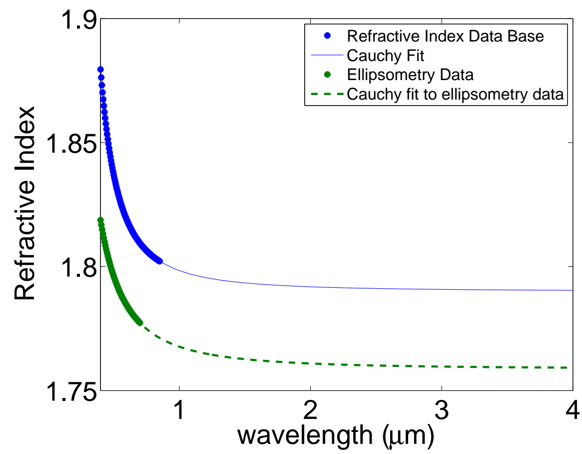

Figure A.2: Ta_2O_5 dispersion curve from SOPRA N&K Database [8], its Cauchy fit and experimental ellipsometry data

- Aluminium oxide (Al_2O_3)

  Al_2O_3 has absorption bands in the far-infrared and ultraviolet region is evident from the Sellmeier equation [9]:

$$
\begin{aligned}
n^2 - 1 &= 1.4313493 \frac{\lambda^2}{\lambda^2 - 0.0726631^2} \\
&+ 0.65054713 \frac{\lambda^2}{\lambda^2 - 0.1193242^2} \\
&+ 5.3414021 \frac{\lambda^2}{\lambda^2 - 18.028251^2}
\end{aligned}
\tag{A.1}
$$

  The ellipsometry data was fitted with a Sellmeier equation similar to Eq. A.1 and it is plotted in Fig. A.3.

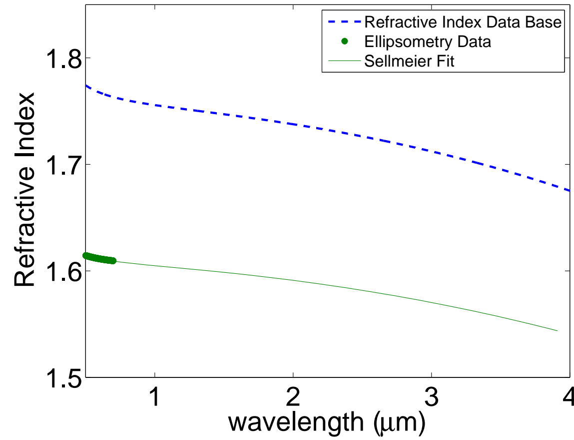

Figure A.3: Al_2O_3 Sellmeier dispersion curve [9], experimental ellipsometry data and its Sellmeier fit

High Index Materials

- Zinc sulfide (ZnS)

  ZnS is one of the most widely used material in infrared region. The refractive index

data [11] can be fitted with a Sellmeier dispersion equation [10] indicating absorption bands in the ultraviolet and far infrared range.

$$
\begin{aligned}
n^2 - 1 &= 3.60981117\frac{\lambda^2}{\lambda^2 - 0.169807804^2} \\
&+ 0.490409060e\frac{\lambda^2}{\lambda^2 - 0.302036761^2} \\
&+ 0.273290892\frac{\lambda^2}{\lambda^2 - 33.8906653^2}
\end{aligned} \quad (A.2)
$$

The spectrum of the refractive index is plotted in Fig. A.4. The ellipsometry data and a Sellmeier fit with parameters similar to Eq. A.2 are also shown in this figure.

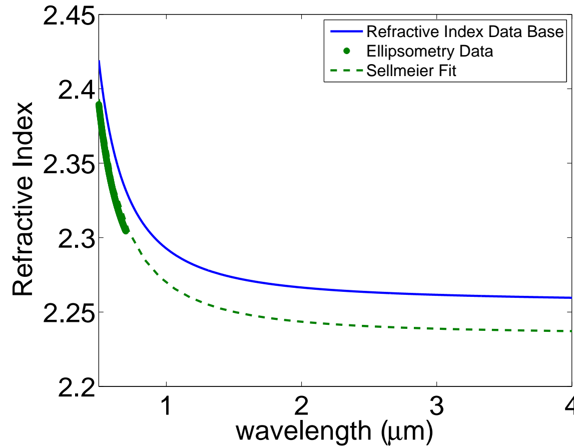

Figure A.4: ZnS Sellmeier dispersion curve [10,11], experimental ellipsometry data and its Sellmeier fit

Low Index Materials

- Yttrium fluoride (YF_3)

  YF_3 is one of the low index materials that was used in multi-layer coatings. The

known refractive index [12] and the ellipsometry data were fitted with a similar Sellmeier equation for consistency, and are plotted in Fig. A.5 .

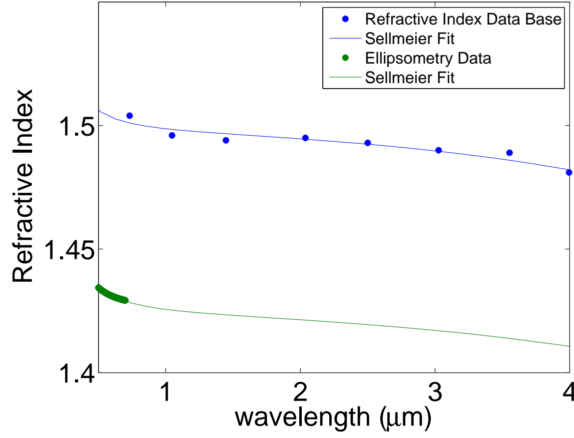

Figure A.5: YF_3 Sellmeier dispersion curve [12] and its Sellmeier fit, experimental ellipsometry data and its Sellmeier fit.

- Silicon dioxide (SiO_2)

  The Sellmeier equation for SiO_2 [9, 13] indicates three absorption bands at 0.06 μm, 0.11 μm, and 9.89μm.

$$\begin{aligned} n^2 - 1 &= 0.6961663\frac{\lambda^2}{\lambda^2 - 0.0684043^2} \\ &+ 0.4079426\frac{\lambda^2}{\lambda^2 - 0.1162414^2} \\ &+ 0.8974794\frac{\lambda^2}{\lambda^2 - 9.896161^2} \end{aligned} \tag{A.3}$$

  The data collected from the ellipsometry was fitted with a similar Sellmeier equation, which gives a refractive index between 1.36 to 1.38 in 3 μm-4 μm region.

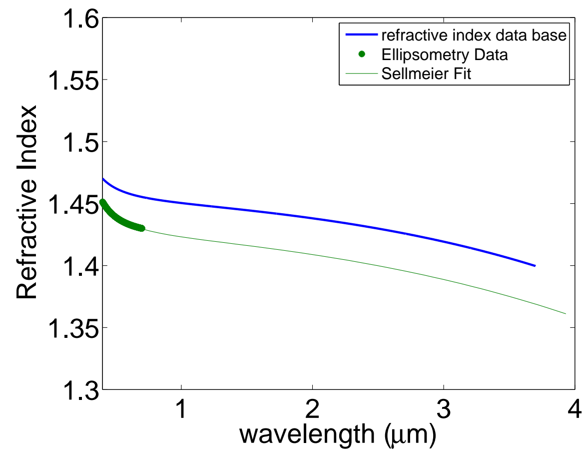

Figure A.6: SiO_2 Sellmeier dispersion curve [9, 13], experimental ellipsometry data and its Sellmeier fit

Appendix B

Double Layer AR Coating Designs

This appendix summarizes the parameters associated with the measured devices in Table 5.2. Under each item, the ARC material and film thickness as well as the target and measured reflectivity are listed. In each section, the contours of constant reflectivity versus film thickness and the reflectivity curve versus wavelength are plotted.

- YF_3-ZnS design for reflectivity of 1% at λ=3.4μm

  YF_3= 176 nm

  ZnS= 164 nm

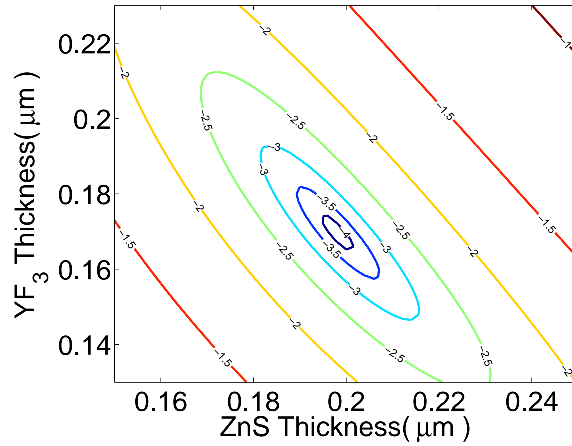

Figure B.1: Contours of constant reflectivity versus film thickness for a double layer YF_3-ZnS ARC for an ICL-3 at λ=3.4μm

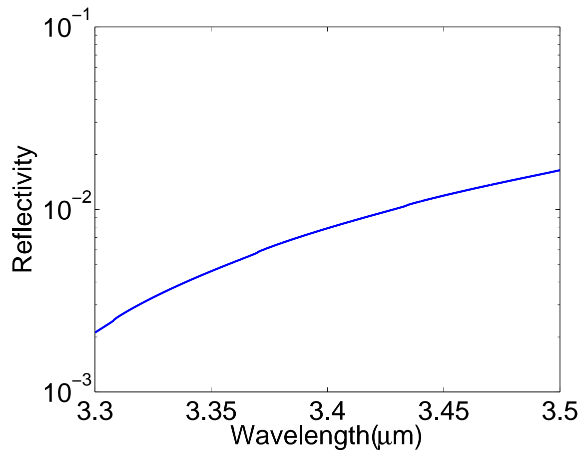

Figure B.2: Reflectivity curve versus wavelength for a double layer YF_3-ZnS ARC with thickness of 177 nm and 164 nm, respectively.

- ZnS-YF_3design for reflectivity of 1% at λ=3.4μm

  ZnS=244 nm

  YF_3=344 nm

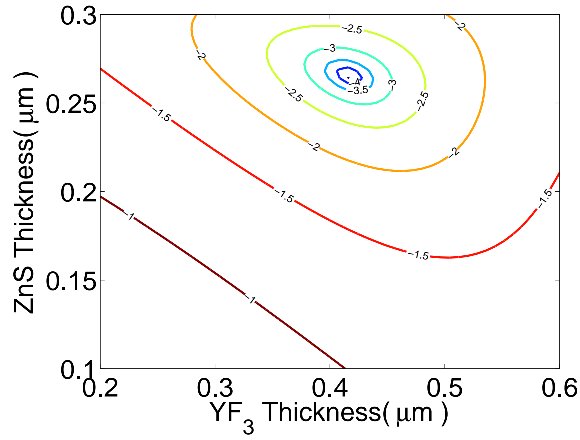

Figure B.3: Contours of constant reflectivity versus film thickness for a double layer ZnS-YF_3 ARC for an ICL-3 at λ=3.4μm

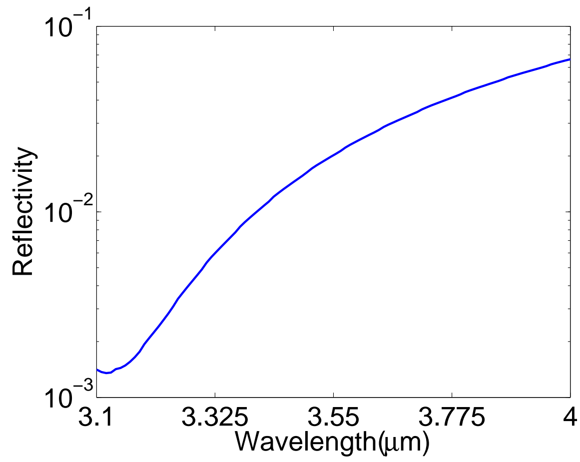

Figure B.4: Reflectivity curve versus wavelength for a double layer ZnS-YF_3 ARC with thickness of 244 nm and 344 nm, respectively.

- TiO_2-SiO_2 design for reflectivity of 1% at λ=3.5μm

  TiO_2= 330 nm

  SiO_2= 200 nm

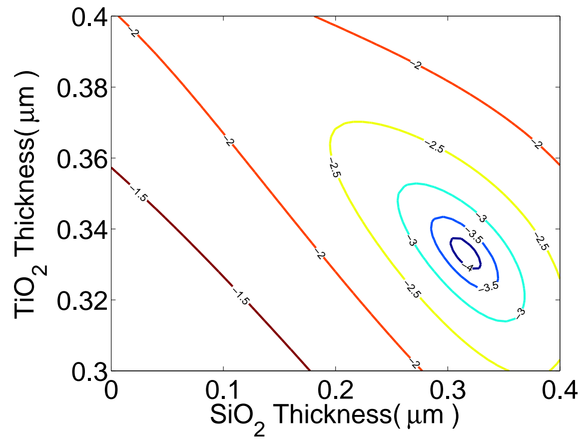

Figure B.5: Contours of constant reflectivity versus film thickness for a double layer TiO_2-SiO_2 ARC for an ICL-1 at λ=3.5μm

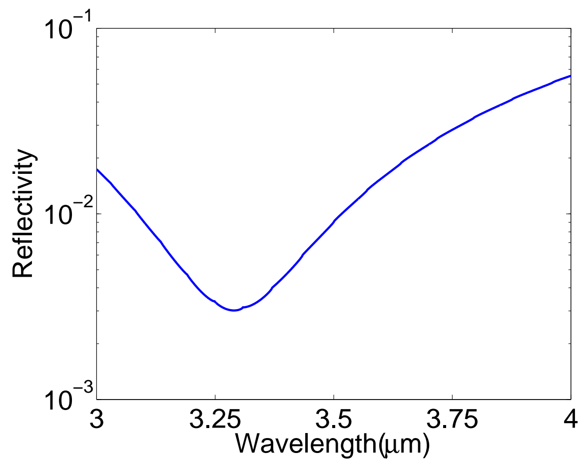

Figure B.6: Reflectivity curve versus wavelength for a double layer TiO_2-SiO_2 ARC with thickness of 330 nm and 200 nm, respectively.

- ZnS-SiO_2 design for reflectivity of 1% at λ=3.8μm

  ZnS=292 nm

  SiO_2=408 nm

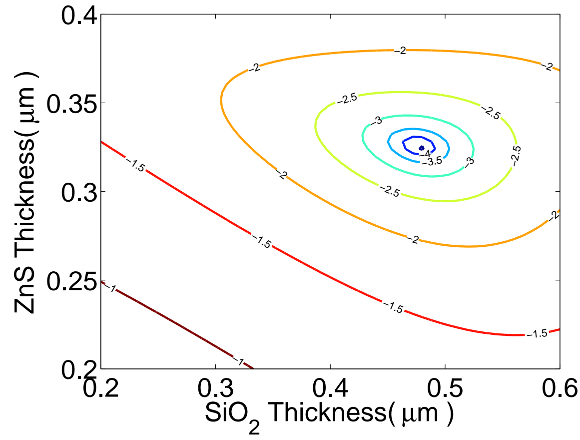

Figure B.7: Contours of constant reflectivity versus film thickness for a double layer ZnS-SiO_2 ARC for an ICL-2 at λ=3.8μm

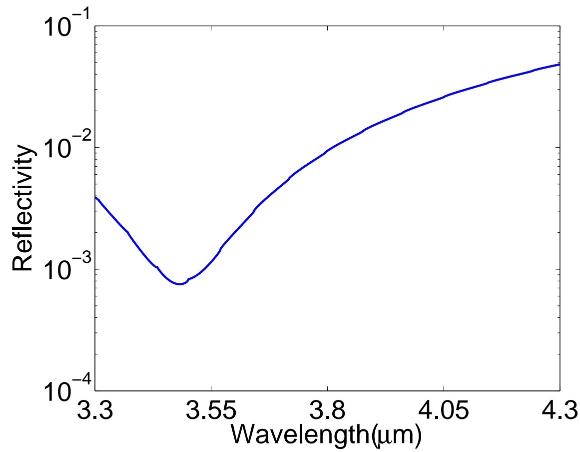

Figure B.8: Reflectivity curve versus wavelength for a double layer ZnS-SiO_2 ARC with thickness of 292 nm and 408 nm, respectively.

- ZnS-SiO_2 design for reflectivity of 1E-5% at λ=3.5μm

  ZnS=287 nm

  SiO_2=447 nm

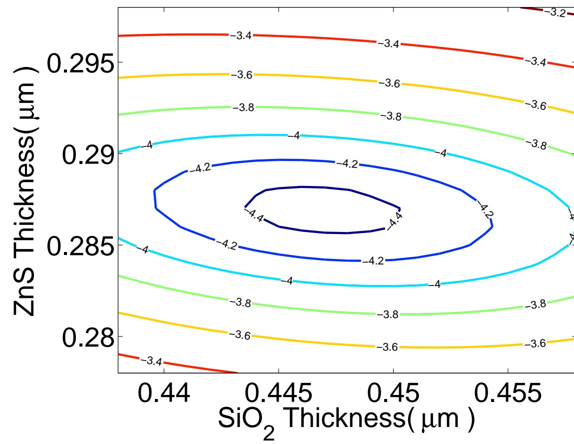

Figure B.9: Contours of constant reflectivity versus film thickness for a double layer ZnS-SiO_2 ARC for an ICL-2 at λ=3.2μm

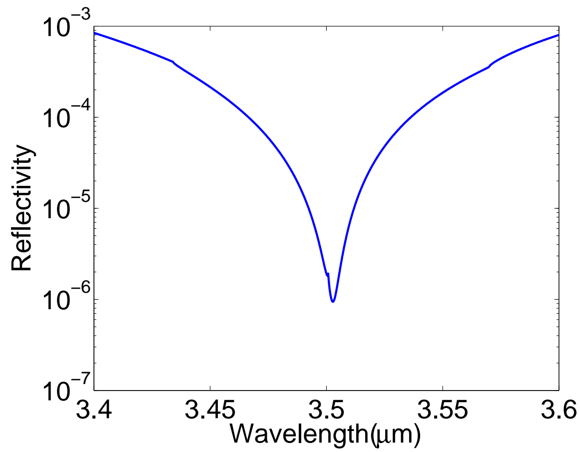

Figure B.10: Reflectivity curve versus wavelength for a double layer ZnS-SiO_2 ARC with thickness of 287 nm and 447 nm, respectively.